

Extraterrestrial and Terrestrial Outdoor Applications of Mössbauer Spectroscopy

Dissertation
zur Erlangung des Grades
des Doktors der Naturwissenschaften
(Dr. rer. nat.)
am Fachbereich Physik
der Johannes Gutenberg - Universität
in Mainz

Paulo Antônio de Souza Júnior
geboren in Campo Grande
Brasilien

Referent: Prof. Dr. Dr. h.c. Philipp Gütlich
Koreferent: Prof. Dr. Hermann Adrian

Mainz 2004

”Die Erfahrung nutzt erst der Wissenschaft sodann schodet sie,
weil die Erfahrung Gesetz und Ausnahme gewahr werden läßt.
Der Durchschnitt von beiden gibt keineswegs das Wahre.”

”The experience benefits science at first, then acts damaging
towards it, because the experience lets one become aware of law
and exception. The average of both is by no means the truth.”

[Goethe: Wilhelm Meisters Wanderjahre]

To my parents Rose and Paulo

Contents

1	Introduction	1
2	^{57}Fe Mössbauer spectroscopy	5
2.1	Mössbauer effect	5
2.2	Mössbauer experiment	9
2.2.1	Doppler effect	9
2.2.2	The standard Mössbauer spectrometer	10
2.2.3	The Mössbauer source	13
2.3	Important effects and transitions	14
2.3.1	Cosine smearing effect	14
2.3.2	Goldanskii-Karyagin effect	14
2.3.3	Super-paramagnetism	15
2.3.4	Morin transition	16
2.3.5	Verwey transition	16
3	Miniaturized Mössbauer spectrometer	19
3.1	MIMOS II sensor head	20
3.2	Mössbauer sources, shielding, and collimator	24
3.3	Drive system	25
3.4	Detector system and electronics	26
3.5	Temperature measurement	27
3.6	Operation modes and software	27
3.6.1	Data structure of MIMOS II	29
3.7	MIMOS II calibration	29
3.7.1	Energy calibration	31
3.7.2	Velocity calibration	32
3.7.3	Internal calibration sample	33
3.7.4	FIDO trials	35
3.7.5	Health checks	37

4	Analysis of the Mössbauer spectrum	39
4.1	Introduction	39
4.2	Classical curve fitting	40
4.3	Curve fitting using genetic algorithm	44
4.4	Fitting control using fuzzy logic	47
4.5	Mössbauer-mineral data bank	49
4.6	Mössbauer phase identification	51
4.6.1	Neural identifiers	54
4.6.2	The implemented neural network	56
4.6.3	Neural identification of minerals	59
4.6.4	Neural identification of crystalline structures	60
4.7	Summary	61
5	Selected terrestrial outdoor applications	65
5.1	Introduction	65
5.2	Air pollution investigation	65
5.3	Historical artifacts analysis	69
5.3.1	Iron purity and corrosion	70
5.3.2	Were iron artifacts burned in sacrifices?	81
5.3.3	Identification of fragments	84
5.3.4	Pigment characterization	88
6	Extraterrestrial applications	97
6.1	Introduction	97
6.2	Meteorites	99
6.2.1	Metallic meteorites	100
6.2.2	Chondrite meteorites	101
6.2.3	Martian meteorites	103
6.3	Martian mineralogy	105
6.3.1	Published Mössbauer parameters on Mars analogue minerals	107
6.4	Mössbauer experiments on Mars	108
6.4.1	MIMOS II calibrations taken on Mars	109
6.4.2	In situ experiments on a Martian rock and soils	112
6.4.3	Strategy of Mössbauer data analysis	113
6.4.4	Selected Mössbauer results from Mars	115
7	Summary, conclusions and outlook	125
7.1	Summary of results	125
7.2	Conclusions and outlook	127

A Possible Mars analogue Fe-minerals	141
A.1 Oxide, hydroxide and oxide-hydroxide	143
A.2 Carbonates and Rich-Mn minerals	143
A.3 Sulphate, sulphide and sulphite	144
A.4 Phosphates	145
A.5 Silicates	146
A.5.1 Nesosilicates	147
A.5.2 Sorosilicates	148
A.5.3 Cyclosilicate	148
A.5.4 Inosilicates	149
A.5.5 Phyllosilicates	150
A.5.6 Tectosilicates	152
A.6 Other minerals	152

Chapter 1

Introduction

Many efforts have started in the early nineties at the Technical University of Darmstadt by Professor Dr. Egbert Kankeleit and his co-workers to miniaturize a laboratory Mössbauer spectrometer such that it can be used for outdoor and extraterrestrial applications. These efforts continued since 1998 at the Institute of Inorganic and Analytical Chemistry of the University of Mainz with Dr. Göstar Klingelhöfer and co-workers. The miniaturized Mössbauer spectrometer called MIMOS II has been recently proven to be a mobile tool for the in situ characterization of samples and solving problems of mineralogy, archaeology and so on.

One part of this thesis is devoted to the non-destructive analysis of the surface of archaeological artifacts. Also, as an outdoor application, a field experiment on air pollution characterization done in Brazil is presented. The other part will deal with the presently on going experiments on Mars performed by the rover *Spirit* of the Mars Exploration Rover mission from NASA. The MIMOS II are being used for the characterization of iron-bearing minerals in this extraterrestrial mission to Mars. The genesis of the planetary surface can be assessed knowing its mineral composition; and to try to get answers of some appealing questions: - Was Mars once a wet planet? - Could it sustain life?

Life on Earth can thrive in many environments, everywhere with available liquid water, energy and nutrient sources. Mars could once hold such environment. Yet, the evolution of both planets have diverged: Earth has remained warm and wet, while Mars has become cold and dry. However, still these are open questions as how wet and warm was Mars, and whether did life develop in our neighbor planet. These questions have been growing in interest since the controversial evidence for fossil microbial life in the Martian

meteorite ALH84001. Magnetite crystals in Martian meteorite ALH84001 are the focus of controversy about the possibility of past (and present) life on Mars. McKay et al. [Mck 96] suggested that some magnetite crystals associated with carbonate globules in the meteorite are biogenic because they share many characteristics with magnetosomes from terrestrial magnetotactic bacteria.¹ These characteristics include size consistent with single magnetic domains, absence of crystalline defects, chemical purity, and coexistence with metastable phases in apparent disequilibrium. On the other hand, Golden et al. [Gol 04] demonstrated that an abiotic inorganic history can produce magnetite crystals like those in ALH84001 which does not support an exclusively biogenic origin. This evidence still controversial. Wherever life conditions hold, organisms will spring up and spread over. Live forms will always be struggling for ways to survive, to adapt and to flourish around.

Mars missions are focused to grow our understanding of the origin and evolution of life in the solar system, determining what conditions were on early Mars, and whether the *red planet* supported life.² Our best present knowledge on Mars suggests that possible past life (fossils) would lie in formerly water-rich regions of ancient terrain or sediment deposits of earlier terrain. But yet, the fundamental substance known to form life is still to be geologically proven that once existed on Mars. Since clay-rich aqueous sediments on Earth frequently hold high concentrations of biogenic organic matter, clay materials such as smectites are very important as candidates to hold evidence for Martian life.³

The challenge of knowing better the analyzed materials, and from these materials the history of the studied samples from archaeological artifacts to the planet Mars is the central point of this thesis. For such extraterrestrial and outdoor terrestrial applications an easy to use spectrometer is needed. There are also severe constraints on non-destructive and remote analysis to be observed. Efforts to meet these constraints will be presented here.

Considering the short time available for deciding the rover activities for the next Martian day, a data analysis suite for quick spectral fitting and mineral identification is needed. This data analysis package was developed using genetic algorithms, fuzzy logic, and artificial neural networks.

¹e.g., *aquaspirillum magnetotacticum*; R. B. Frankel, R. P. Blakemore, S. T. A. Squivel, and J. Danon, Magnetotactic bacteria at the geomagnetic equator, *Science* 212(1981)1269.

²Details are given in chap. 6.

³Check app. A for a list of iron-bearing clay minerals.

The many years of efforts to develop the light-weighted and robust MIMOS II spectrometer opened the possibility of many interesting non-destructive and outdoor terrestrial applications. Some of these applications are explored in this thesis. Also the data analysis package can be useful for non-specialists in Mössbauer spectroscopy.

Chapter 2 describes basic concepts of ^{57}Fe Mössbauer spectroscopy, as well as some effects that can be investigated by this technique.

The portable and miniaturized Mössbauer spectrometer (MIMOS II), developed by the group in Mainz lead by Dr. Göstar Klingelhöfer, is presented in detail in chapter 3. The calibration procedures, functionality, and operational features are also presented.

The analysis of a Mössbauer spectrum is described in detail in chapter 4. In this chapter the proposed analysis using genetic algorithms, fuzzy set theory, and artificial neural networks is discussed and some examples are demonstrated. The motivation of this development is to make a data analysis package available for fast fitting of the Mössbauer spectrum, and precise identification of minerals from Mössbauer parameters.

In chapter 5 some outdoor terrestrial applications of MIMOS II is proposed. The chapter starts presenting the use of MIMOS II for in situ air pollution investigation in Vitória, ES, Brazil. The instrument was adapted for the characterization of airborne particles in an industrial urban area. This chapter contains surface analysis of painted figures on ancient pottery, of fragments of Chinese wall paintings, and of a "miniature" from the fifteenth century; and the characterization of a Celtic helmet knob to determine whether it was burned in sacrifices. The authenticity of fragments of a Roman mask is verified with the Mössbauer spectrum obtained with MIMOS II. The characterization of corrosion products in archaeological artifacts is also reported. For this characterization it was necessary to supplement data from X-ray diffraction and SQUID (Superconducting Quantum Interference Device).

Chapter 6 is devoted to extraterrestrial applications, starting with the results on Mössbauer characterization of some meteorites. Detailed discussion of data obtained by MIMOS II onboard of the rover *Spirit* at the Mars surface and comparison of Mössbauer experiments of a Martian rock and meteorites are also presented.

Summary, conclusions and outlook are presented in chapter 7, which is followed by some of the used bibliography and an appendix on candidate Martian minerals.

Chapter 2

^{57}Fe Mössbauer spectroscopy

When the radiation interacts with matter many effects are produced. Wherein Compton and fluorescence effects are particularly important and are used in many experimental techniques. The effect studied and used in this thesis is the fluorescence. "Fluorescence is the property of emitting radiation as a result of absorption of radiation from other source. The emitted radiation persists only as long as exposure is subject to radiation which may be either electrified particles or waves. The fluorescent radiation generally has a longer wave length than that of the absorbed radiation. If the fluorescent radiation includes waves of the same wavelength as that of the absorbed radiation it is termed resonance radiation."¹ A nuclear resonant fluorescence phenomena studied here is the Mössbauer effect, the non-resonant part is the X-ray fluorescence.

The recoil free nuclear resonance absorption was discovered by Rudolf Mössbauer in 1957 [Mös 58a, Mös 58b, Mös 62, Mös 00]. Some of the principles, experimental setup, and special magnetic transitions are discussed in this chapter. The data analysis commonly used and proposed is discussed in detail in chapter 4. Further details are described in some textbooks [Wer 64, Güt 78, Mit 92].

2.1 Mössbauer effect

If a nucleus in an excited state with mean lifetime τ_N ($141\text{ ns }^{57}\text{Fe}$) emits γ -radiation, the energy distribution follows the Breit-Wigner law (Lorentzian):

¹CRC Handbook of Chemistry and Physics, Editor-in-chief David R. Lide, 79th Edition 1998-1999, Chemical Rubber Company Press, Boca Raton, USA.

$$I(E) = I_0 \cdot \frac{(\Gamma/2)^2}{(E - E_0)^2 + (\Gamma/2)^2} \quad (2.1)$$

where E_0 is the transition energy and $\Gamma = \hbar/\tau_N$ is the resonance width ($E_0 = 14.4\text{keV}$, $\Gamma = 4.7\text{neV}$ for ^{57}Fe). The momentum of the γ -quantum is $\hbar k$. A free atom emitting a γ -quantum will recoil with the energy $E_r = p_\gamma^2/2M = \frac{(E_\gamma)^2}{2Mc^2}$ ($E_r = 2\text{meV}$ for ^{57}Fe). The recoil energy is much larger than the natural line width Γ . If the emitting nucleus is in a solid, the whole matrix takes up the recoil. As this mass is about 10^{20} times larger as compared with the single nucleus, the recoil energy becomes negligible. This enables the resonant nuclear emission and absorption, i.e., the Mössbauer effect. Nevertheless, the emission (or absorption) may also involve energy transfer to lattice vibrations (phonons) in the crystal and the probability that the emission takes place without inducing any phonons is named, as in X-ray diffraction, Debye-Waller factor f_A . As shown in Eq. 2.2, this factor depends on the temperature T , the Debye temperature Θ_D of the crystal, and on the energy of the γ -quantum [Gon 86]:

$$f_A(T) = \exp\left\{\frac{-3\hbar^2 k^2}{4Mk_B\Theta_D} \left[1 + 4\left(\frac{T}{\Theta_D}\right)^2 \int_0^{\Theta_D/T} \frac{y}{\exp(y) - 1} dy\right]\right\} \quad (2.2)$$

The probability of recoil free emission or absorption is 0.76 for ^{57}Fe in $\alpha\text{-Fe}$ at room temperature. Due to the high resolution involved in this process, the hyperfine interactions can be resolved by a Doppler gamma energy modulation

$$E(\nu) = E_0 \cdot \left(1 + \frac{\nu}{c}\right) \quad (2.3)$$

by moving the source relative to the absorber, or vice versa. Usually, the source is moved and the necessary velocities for ^{57}Fe lie in the range of ± 10 mm/s. The energy resolution of this movement allows the observation of the change of the energy levels resulting from electric or magnetic fields acting at the nucleus. These are the electric monopole interaction, the electric quadrupole interaction, and the magnetic dipole interaction. These (hyperfine) interactions can be translated into the following three parameters that can be measured in the Mössbauer spectrum, after curve fitting:

1. The isomer shift (δ):

The electrical monopole interaction is the interaction of the nuclear charge Ze with the electron density. This leads to a change of the

energy states in the source (s) and the absorber (a) as compared to a point charge [Wer 64]:

$$E_{s,a} = E_0 + \frac{2}{5}\pi Z e^2 |\Psi_{s,a}(0)|^2 [R_e^2 - R_g^2] \quad (2.4)$$

Here Ψ is the electron wave function $e|\Psi_s(0)|^2$ is the electron density at the nucleus and R is the nuclear radius of the state (index g for ground state, e for the excited one). The energy difference between the absorber and the source ($\delta = E_a - E_s$) results in the the isomer shift. Thus,

$$\delta = \frac{2}{5}\pi Z e^2 [|\Psi_a(0)|^2 - |\Psi_s(0)|^2] [R_e^2 - R_g^2] \quad (2.5)$$

2. The quadrupole splitting (Δ):

An electrical quadrupole moment of the nucleus, eQ , interacts with the electric field gradient tensor (**EFG**) acting at the nucleus, leading to a splitting of the energy levels. The asymmetry parameter η is obtained by diagonalizing the **EFG** tensor:

$$V_{ij} = \frac{\partial^2}{\partial r_i \partial r_j} V \quad (2.6)$$

where V is the electrical potential with $|V_{zz}| \geq |V_{yy}| \geq |V_{xx}|$ and $V_{xx} + V_{yy} + V_{zz} = 0$, and the asymmetry parameter η is given by:

$$\eta = \frac{V_{xx} - V_{yy}}{V_{zz}}. \quad (2.7)$$

The energy shift for a state with spin I and magnetic quantum number m_I is:

$$E_q(m_I) = \frac{eQV_{zz}}{4I(2I-1)} \left[3m_I^2 - I(I+1) \right] \sqrt{1 + \frac{1}{3}\eta^2} \quad (2.8)$$

For ^{57}Fe with $I_g = 1/2$ and $I_e = 3/2$ only the excited state splits and the quadrupole splitting Δ is:

$$\Delta = E_q(m_I = 3/2) - E_q(m_I = 1/2) = \frac{1}{2}eQV_{zz} \sqrt{1 + \frac{1}{3}\eta^2} \quad (2.9)$$

3. The internal magnetic field (B_{hf}):

The magnetic moment μ of the nucleus interacts with a magnetic field B acting at the nucleus (nuclear Zeeman effect). This interaction leads

to the splitting of the degenerated states. The state with spin I splits into $2I + 1$ magnetic sub-states with eigenvalues:

$$E_m = -\frac{\mu B m_I}{I} = -g_N \mu_N B m_I \quad (2.10)$$

where the magnetic quantum number m_I can hold the values $m_I = I, I - 1, \dots, -(I - 1), -I$. The magnetic moment μ is given by the Bohr magneton μ_N and the Landé factor g_N by:

$$\mu = g_N \mu_N I. \quad (2.11)$$

From the selection rule ($\Delta m = 0, \pm 1$) only six transitions are possible (sextets in the Mössbauer spectra of magnetic materials).

If there is an action of the magnetic dipole and the electric quadrupole, the eigenvalues cannot be determined as easily as for each interaction alone [Fri 89]. As usually the magnetic interaction is much stronger, first the eigenvalues are determined for this magnetic interaction and the electric one is treated as a perturbation. For the energy states in a first order perturbation calculation one can obtain [Bla 85]:

$$E_m = -g_N \mu_N B m_I + (-1)^{|m_I|+\frac{1}{2}} \cdot \frac{1}{4} \cdot e Q V_{zz} \cdot \frac{1}{2} (3 \cos^2 \theta - 1 + \eta \sin^2 \theta \cos 2\phi) \quad (2.12)$$

where θ and ϕ are angles between the direction of the magnetic field and the predominant axis of the electric field gradient component V_{zz} . For ^{57}Fe we have:

$$\Delta = \frac{1}{8} \cdot e Q V_{zz} (3 \cos^2 \theta - 1 + \eta \sin^2 \theta \cos 2\phi) \quad (2.13)$$

The line positions for the general case can be given by equation 2.14:

$$\begin{aligned} L_1 &= \delta - g_1 \mu_N B + \Delta \\ L_2 &= \delta - g_2 \mu_N B - \Delta \\ L_3 &= \delta - g_3 \mu_N B - \Delta \\ L_4 &= \delta + g_3 \mu_N B - \Delta \\ L_5 &= \delta + g_2 \mu_N B - \Delta \\ L_6 &= \delta + g_1 \mu_N B + \Delta \end{aligned} \quad (2.14)$$

The g -factors g_x result from the Landé factors of the ground state g_g and the excited state g_e are given in equation 2.15:

$$g_1 = \frac{1}{2} \cdot (3|g_e| + g_g)$$

Table 2.1: Line intensities for the magnetic dipole interaction (cf. fig. 2.1).

line	transition	Δm_I	intensity
L_1	$-3/2 \rightarrow -1/2$	+1	$I_1 = 3/8(1 + \cos^2 \theta)$
L_2	$-1/2 \rightarrow -1/2$	0	$I_2 = 1/2(1 - \cos^2 \theta)$
L_3	$+1/2 \rightarrow -1/2$	-1	$I_3 = 1/8(1 + \cos^2 \theta)$
L_4	$-1/2 \rightarrow +1/2$	+1	$I_4 = 1/8(1 + \cos^2 \theta)$
L_5	$+1/2 \rightarrow +1/2$	0	$I_5 = 1/2(1 - \cos^2 \theta)$
L_6	$+3/2 \rightarrow +1/2$	-1	$I_6 = 3/8(1 + \cos^2 \theta)$

$$g_2 = \frac{1}{2} \cdot (|g_e| + g_g) \quad (2.15)$$

$$g_3 = \frac{1}{2} \cdot (|g_e| - g_g)$$

The relative line intensities I_x for a sextet depends on the angle $\theta = \widehat{\vec{k}, \vec{I}}$ between the propagation direction \vec{k} of the γ -radiation and the direction of the spin (magnetization) \vec{I} .

If the directions of magnetization are randomly (isotropic) distributed ($\bar{\theta} = 54.7^\circ$), the ratios are $I_1 : I_2 : I_3 = 3 : 2 : 1$. For $\theta = 90^\circ$ the intensity ratio is $I_1 : I_2 : I_3 = 3 : 4 : 1$, whereas for $\theta = 0^\circ$ the intensities are $I_1 : I_2 : I_3 = 3 : 0 : 1$, that is, the lines L_2 and L_5 disappear. The relative intensities for the magnetic dipole interaction are given in table 2.1.

All these hyperfine parameters, except the isomer shift, are also found for *Perturbed Angular Correlation* (PAC) [Sch 92] and they are comparable with those observed by Mössbauer spectroscopy.

2.2 Mössbauer experiment

2.2.1 Doppler effect

The main components of a Mössbauer spectrometer are the γ -ray source containing the Mössbauer active nuclide, the absorber (or scatterer), a transducer, a detector for low-energy γ -radiation, and electronics for storing the measured data. The source and the absorber are moved relative to each other. The transmitted (or scattered) γ -quanta are registered as a function of the relative velocity, being possible to follow the absorption line or the emission line by Doppler effect. A γ -quantum emitted from the source moving at a velocity v receives a Doppler energy E_D modulation given by

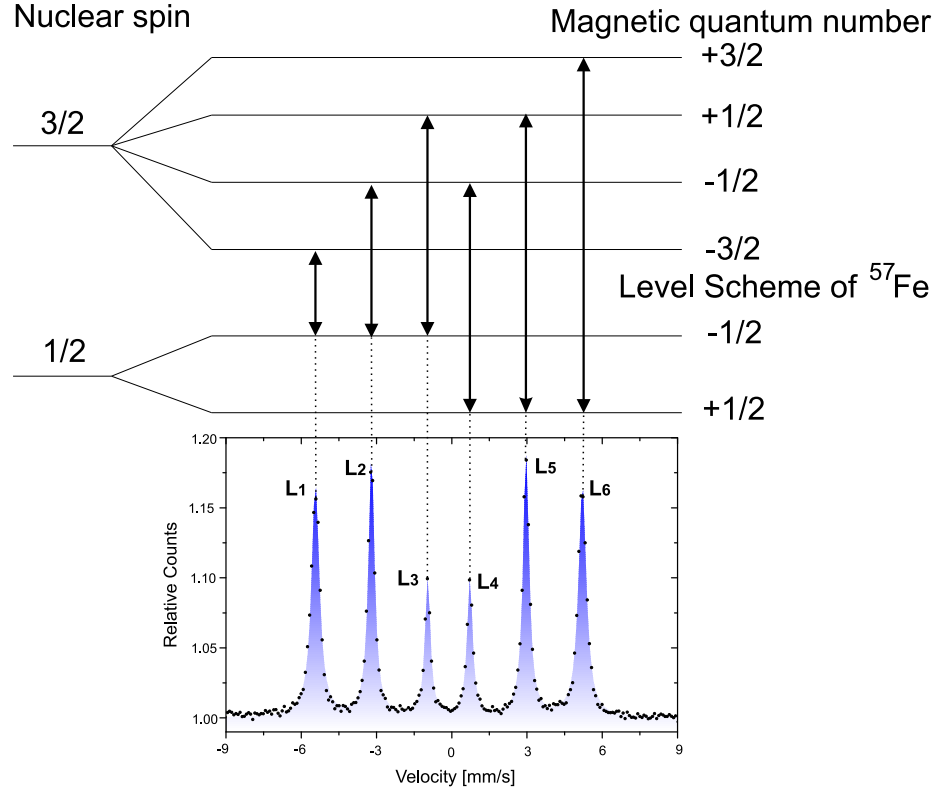


Figure 2.1: The magnetic hyperfine interaction in α -Fe (cf. table 2.1).

$$E_\gamma = E_0 + E_D = E_0 \left(1 + \frac{v}{c}\right) \quad (2.16)$$

where E_0 is the energy of the γ -quantum emitted from the same source at rest and c is the velocity of light. This relation is valid for a moving source, the velocity being positive for the source moving towards the absorber. Resulting from the very narrow line width Γ of the resonance line, it is generally sufficient to produce a small Doppler energy change E_D of the order of the line width Γ by Doppler shifting the source in order to sweep over the resonance (fig. 2.2). The Doppler velocities needed in case of ^{57}Fe spectroscopy are in the range of 10 mm/s.

2.2.2 The standard Mössbauer spectrometer

The standard Mössbauer spectrometer generates the spectrum by the velocity-sweep method. The drive system moves the source (or absorber) repeatedly over a range of velocities, while simultaneously counts the γ -quanta behind

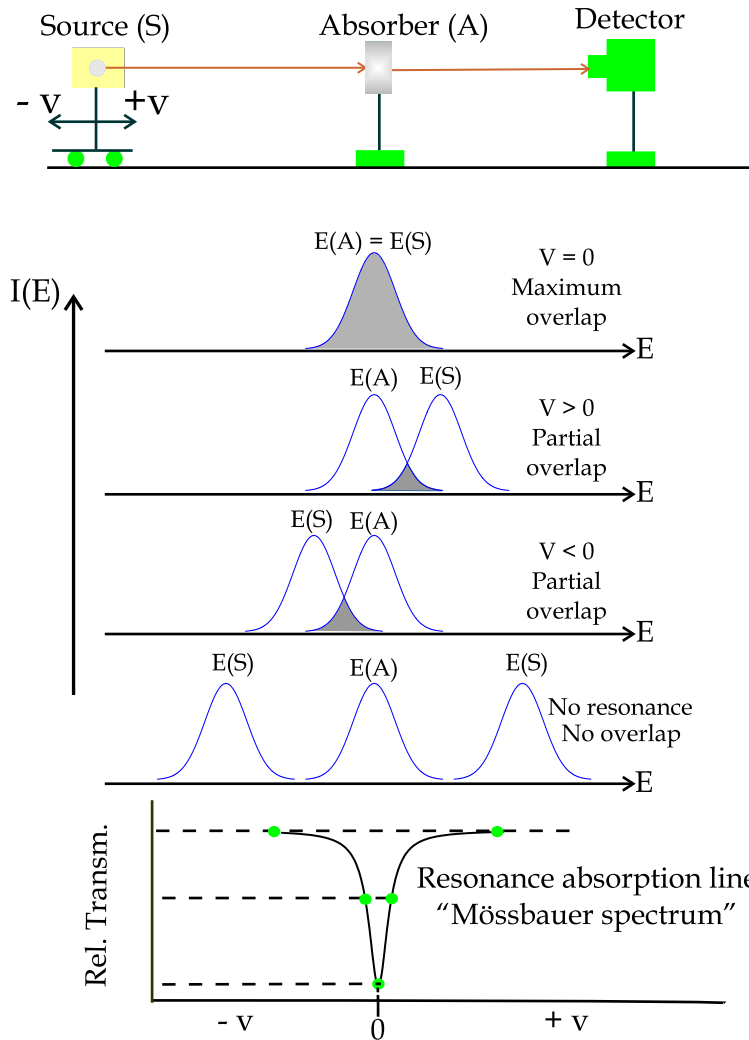


Figure 2.2: Schematic illustration of the experimental arrangement for the recoil free nuclear absorption, and the relative transmission of recoil free γ -quanta as a function of Doppler velocity.

the absorber into synchronized channels. The modern Mössbauer spectrometers have a velocity transducer, the wave form generator and synchronizer, the multichannel analyzer, γ -ray detection system, a cryostat or oven for temperature dependent measurements, a velocity calibration device, the source, the absorber, and a computer (fig. 2.3).

The source (or the absorber) is mounted on the vibrating axis of an electromagnetic transducer (loudspeaker system) which is moved according to a voltage waveform applied to the driving coil of the system. Usually, the source is moved with a constant acceleration, given a certain velocity as

the drive moves. Other options like the use of piezoelectric drive were also proposed [Alf 62].

The pulses detected after the absorption through the absorber are stored in a memory (typically 512 or 1024 channels). Synchronization of the channel number in the memory and the instantaneous velocity of the source is achieved by advancing the memory address one by one. This is done through an external clock which subdivides the period of the waveform applied to the drive system into the number of available channels. The whole velocity range of interest is scanned typically 10 to 60 Hz.

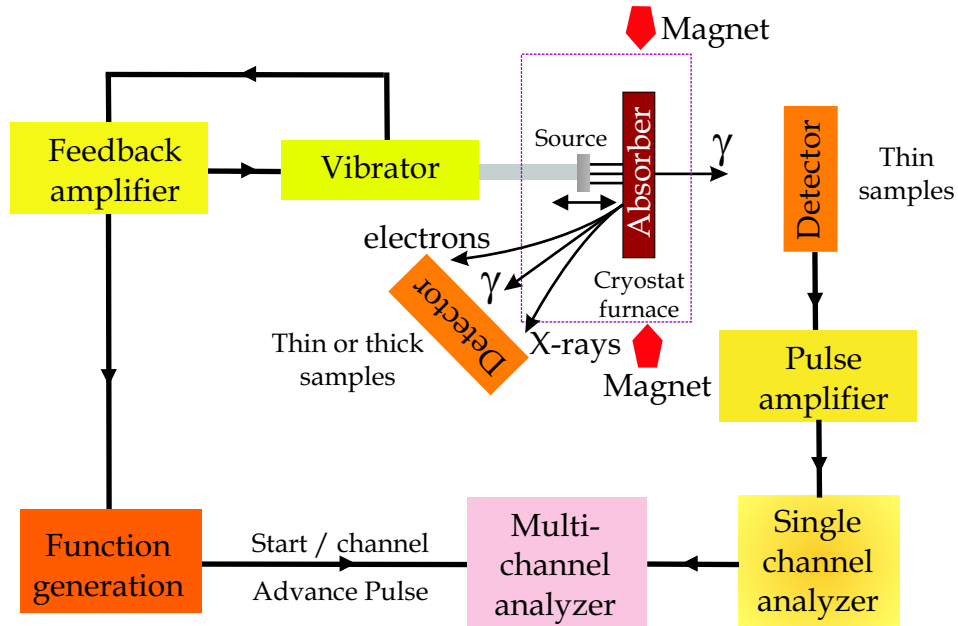


Figure 2.3: Block diagram illustrating the principle of a Mössbauer spectrometer. Transmission geometry is obtained from thin samples. The backscattering geometry, convenient for thin or thick samples, can be detected either with emission electrons, X-rays or γ -rays.

In the standard experimental geometry for Mössbauer measurements, the sample is irradiated and the absorption is measured with a detector behind the sample. This is called the *transmission geometry* (TMS). The effect of the internal conversion is also very important in Mössbauer spectroscopy. As a result of internal conversion, conversion electrons, Auger electrons, and conversion X-rays are also emitted and can be used for the Mössbauer measurements. In the *Conversion X-ray Mössbauer Spectroscopy* (CXMS), conversion X-rays or re-emitted γ -radiation are used to measure the Mössbauer effect in the samples under study. This method is convenient for in situ measurements on thick samples, and was used in the development of a miniaturized Mössbauer spectrometer (MIMOS II) [Kli 95]. The use of more than

one of these Mössbauer setups may provide information on different layers of the material studied.

Some additional experimental accessories can be attached to a standard Mössbauer spectrometer. They are lasers, pressure cells, oven or cryostat, superconducting or permanent magnets, different detector types such as for the deep selective conversion electron Mössbauer spectroscopy. The use of one or simultaneously some of these apparatus yield changes in the Mössbauer pattern. This may allow better understanding of the sample structure and composition.

2.2.3 The Mössbauer source

The source of a Mössbauer experiment is a radioactive isotope of appropriate half-life and adequate nuclear transition energy and excited state lifetime. In the radioactive disintegration, the isotope populates a nuclear excited state which decays to the ground state emitting low-energy gamma radiation. Figure 2.4 shows the decay scheme of ^{57}Co which populates the 14.4 keV Mössbauer level of ^{57}Fe with a lifetime of $\tau_N = 141\text{ns}$. The Mössbauer source should have the emission line as narrow and intense as possible, unsplit and unbroadened; its recoil free fraction should be as high as possible; the material should be chemically inert during the lifetime of the source. Also the Mössbauer source matrix should not give rise to interfering X-rays and Compton scattering, and the photoelectric processes should be insignificant. Other Mössbauer active nuclei were also reported (e.g., [Güt 78]).

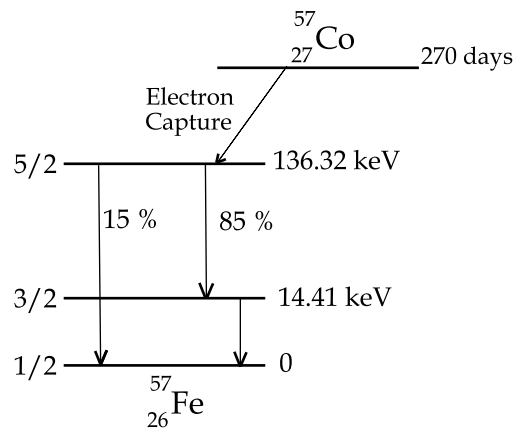


Figure 2.4: Decay scheme of ^{57}Co .

2.3 Important effects and transitions

There are some effects and transitions that can be followed by Mössbauer spectroscopy. These effects result from experimental setups, sample temperature, incorporated water, lattice defects, impurities, crystallinity degree, other elemental substitution, anisotropy, and grain size distribution. Temperature and external magnetic field can also induce changes in the Mössbauer spectrum revealing some interesting characteristics of minerals. Some of these effects, important to Mars temperature range, are described in this section.

2.3.1 Cosine smearing effect

The backscattering Mössbauer experiment parameters can influence the shape of the obtained spectrum. Cosine smearing results from γ -quantum ejected from the source in an angle ϕ relative to the drive axis. The Doppler energy added to the γ -quantum by drive velocities decreases to

$$E_D = E_0 \frac{v_0}{c} \cos\phi; \quad (2.17)$$

and

$$\cos\phi = \frac{v}{v_0}. \quad (2.18)$$

where v_0 is the actual drive velocity and v is the Doppler velocity that leads to the resonance. At high velocities the effect on a Mössbauer spectrum is a widening of peaks while their center shifts outward. Collimators are useful to extenuate the effect. For coaxial symmetry [Ara 70] calculations show that when the ratio of the radius of the collimator and the distance between source and collimator is smaller than or equal to 0.1 cosine smearing can be neglected. This is the case for transmission Mössbauer setups. Should this constraint not be fulfilled, mathematical corrections can be used. In the backscattering setup of MIMOS II the detectors lie in a separate plane and additionally do not comply to coaxial symmetry. Held [Hel 97] solved this problem implementing a correction in a fitting routine.

2.3.2 Goldanskii-Karyagin effect

An anisotropy in the recoil free fraction (f_A) can be observed in a polycrystalline sample if the absorption spectrum shows resolved hyperfine structure

[Kar 63, Gol 63]. This anisotropy leads to relative intensities of the various absorption lines distinct from those expected from a randomly oriented polycrystalline sample. In a cubic crystal the recoil free fraction is isotropic; but crystals with different crystalline symmetry would show anisotropy in f_A .

2.3.3 Super-paramagnetism

Magnetic particles can lose its magnetic order by decreasing the particle size, increasing the temperature, and by isomorphic substitution. The small particle size effects causing super-paramagnetism have been found in iron oxide-hydroxides, α -*Fe*, oxides, olivine in lunar samples, magnetite in Orgueil meteorite, and clay minerals (e.g., Fe-smectites). The super-paramagnetism is common in many natural systems such as soil, corrosion products, and archeological artifacts.²

According to Cornell and Schwertmann [Cor 03], super-paramagnetism arises as a results of magnetic anisotropy, i.e., the existence of preferred crystallographic directions along which the electron spins are most readily aligned and the substance most easily magnetized. If sufficient energy is supplied, magnetism can be reversed along these axes. The time required for spin reversal, the relaxation time (τ_N) depends on the height of the energy barrier between the forward and reverse spin states and the temperature, according to

$$\tau_N = \exp\left(\frac{K_{eff} \cdot V}{kT}\right). \quad (2.19)$$

The weight of the energy barrier between the forward and reverse states is the product of the particle volume (V) and the anisotropy constant (K_{eff} , which is, to some extent, a function of particle size). Super-paramagnetic relaxation occurs when the thermal energy of the particle exceeds the activation energy barrier between the spin states and so allows rapid, spontaneous fluctuations between these states. The effect of these spin reversals is that the observed magnetic field is reduced or even absent.

Because the appearance of the super-paramagnetic effect depends on the anisotropy constant and on the particle size, it is often displayed at room temperature by iron oxides < 10 nm in size, for example, hot-springs materials (e.g., [Wdo 67] and references therein). By lowering the temperature the super-paramagnetic relaxation can be counteracted and, thereby increasing τ_N .

²See chap. 5.3 for some examples.

Super-paramagnetism was found in many systems such as in the corrosion products of archeological artifacts (sec. 5.3.1) and in the wall paintings from China (sec. 5.3.4).

2.3.4 Morin transition

The Morin transition (MT) in hematite ($\alpha\text{-Fe}_2\text{O}_3$) is a well-known phenomenon resulting from a magnetic phase transition from an antiferromagnetic (AF) to a weakly ferromagnetic (WF) state. At high temperatures the spins are lying in the basal plane (1 1 1) in hematite, forming a slight canting with each other, resulting from a Dzyaloshinsky anti-symmetric coupling [Dzy 58], whereas at low temperatures the spins order antiferromagnetically in the rhombohedral (1 1 1) plane. For pure hematite, this 90° first-order spin transition normally takes place in the range $T_M = (263 - 267)\text{K}$ [Van 01]. MT was explained as a result of a competition between strong magnetic-dipolar and single-ion anisotropy and as function of the sign of high-order anisotropy constants by Vandenberghe et al. [Van 01].

The quadrupole shift $2\epsilon_Q$ depends on the canting angle θ of the spins with respect to the Electric Field Gradient principal axis [1 1 1], as given by

$$2\epsilon_Q = \frac{\Delta}{2(3\cos^2\theta - 1)} \quad (2.20)$$

and, therefore, yielding values with opposite sign for the AF ($\theta = 0^\circ$) and WF ($\theta = 90^\circ$) states. MT in non-ideal hematite results in a shift of T_M together with the presence of a temperature interval, in which AF and WF states coexist. Usually, the Mössbauer spectra exhibit two distinct phases for which the WF phase increases at the expense of the AF phase. Al-substituted hematite in which a lower T_M generally corresponds to a broader temperature region of coexistence of both phases. For hematite particles smaller than 20nm no MT was observed and WF phase persists down to 4.2 K. Similarly, substitution of Al for Fe at concentrations above 8 at.% suppresses the MT transition [Gra 82].

2.3.5 Verwey transition

Coulomb interaction that overcomes the kinetic energy of carriers below a certain temperature (Wigner crystallization) produces, in magnetite, an alternating $\text{Fe}^{2+} - \text{Fe}^{3+}$ ordering within the B-sites of the spinel structure. Below the Verwey temperature [Ver 41], $T_V = 119\text{K}$, the Mössbauer spectrum reveals distinct hyperfine patterns for Fe^{2+} and Fe^{3+} in B-site [Mør 83]. Above 119K the octahedral pattern of the mixed state exhibits line-broadening.

This is due to decreasing hopping relaxation time which approaches the Larmor frequencies of the ^{57}Fe ground states [Kün 69]. The Verwey transition temperature is found to decrease with the decreasing of the particle size.

For the Mössbauer experiment in the Mars surface, the Verwey transition (VT) will not be detected once the Mars temperature lies between 290 K down to 130 K during a typical sol.³ Nevertheless, further use of MIMOS II to other space bodies such as comets, Moons, meteors, for example, if such body contains magnetite, VT should be considered.

³A day on Mars is called sol. A martian solar day has a mean period of 24 hours 39 min 35.244 s and is referred to as a sol to distinguish this from a roughly 3% shorter solar day on Earth. A martian sidereal day, as measured with respect to the fixed stars, is 24 hours 37 min 22.663 s, as compared with 23 hours 56 min 04.0905 s for Earth. See <http://www.giss.nasa.gov/tools/mars24/> for more information.

Chapter 3

Miniaturized Mössbauer spectrometer

Because of mission constraint for minimum mass, volume, and power consumption, the MIMOS II is extremely miniaturized compared to standard laboratory Mössbauer spectrometers [Kli 03]. All MIMOS II components were selected to resist high acceleration forces and shocks, temperature variations over the Martian diurnal cycle, and cosmic irradiation. Because of restrictions in data transfer rates, most instrument functions and data processing capabilities, including acquisition and separate storage of spectra as a function of temperature, are performed by an internal dedicated microprocessor (CPU) and memory. The dedicated CPU is also required because most Mössbauer measurements will be done at night when the rover CPU is turned off to save power. High detection efficiency is extremely important in order to minimize experiment time. Experiment time is also minimized by using as strong a $^{57}\text{Co}/\text{Rh}$ source as possible. Because the half life of ^{57}Co (271 days) is not much longer than the seven month duration of the journey to Mars, this implies a design and schedule that allows the source to be manufactured, delivered, and mounted in MIMOS II as close to launch as possible. Instrument internal calibration is accomplished by a second, less intense radioactive source mounted on the end of the velocity transducer opposite to the main source, and in transmission measurement geometry with a well known reference sample. For "Mars Exploration Rover" mission (MER), the spectrometer can also be calibrated with the magnetite "compositional calibration target" (CCT) which is mounted on the rover body [Squ 03]. Physically, MIMOS II has two components that are joined by an interconnect cable: the sensor head and electronics printed-circuit board.

3.1 MIMOS II sensor head

Reduced in size and weight, in comparison to normal laboratory setups, the MIMOS II sensor head just weighs approximately 400 g, with a volume of $(50 \times 50 \times 90) \text{ mm}^3$ (fig. 3.1). The drive weighs 56 g (in 15.5 cm^3), and holds two γ -ray sources: the stronger (25 to 300 mCi) for experiments and the weaker (0.1 to 1 mCi) for calibrations. The activity of the source can be chosen accordingly to the time available to record a good spectrum, the need for space as well as the required radiation shielding. The collimator (in sample direction) also shields the primary radiation off the detectors. Tantalum plates of 0.5 mm are placed at the backside of the detectors to avoid direct radiation from the sources. The boxes stretching out behind the detectors contain amplifiers and discriminators.

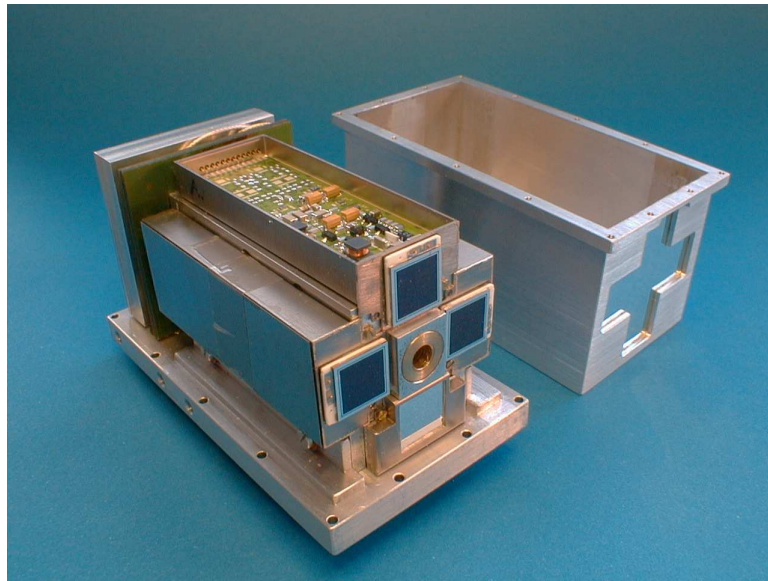


Figure 3.1: The sensor head of the miniaturized Mössbauer spectrometer: MIMOS II. The four PIN-diode detectors are front-faced shown. The sensor head dimensions are $(9 \times 5 \times 5) \text{ cm}^3$.

Around the drive, the detector units (four in this setup) are mounted. The detectors (fig. 3.1) are made of Si-PIN-photodiodes in chip form (area = 100 mm^2 , thickness $\sim 500 \mu\text{m}$). Incident light is reflected by Al metallic window at the sample facing side of each chip.

The control unit is located in a separate electronics board. This board is responsible for the power supply, generation of the drives' velocity reference signal, read of the detector pulses to record the Mössbauer spectrum, perform

data storage, and communication with the host computer. Therefore, there is a microprocessor, RAM and ROM data storage units, an A/D converter, the host interface and power converters. The computer is only needed to start and stop of the running measurement as well as to read and analyze the data.

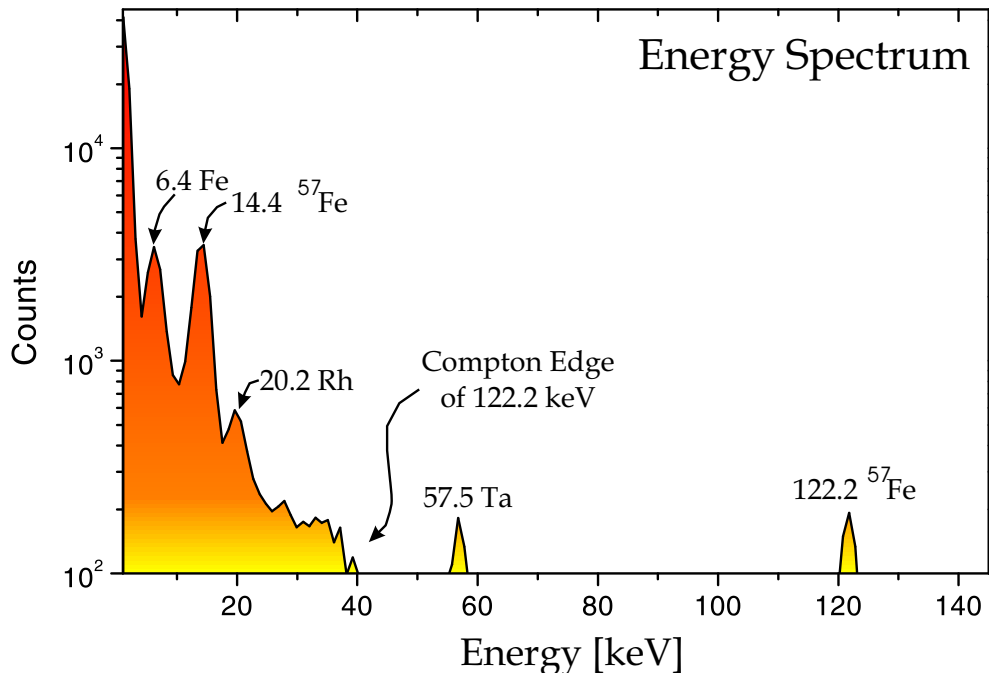


Figure 3.2: Energy spectrum of the $^{57}\text{Co}/\text{Rh}$ source recorded at 173 K with a MIMOS II detector. Threshold values for MIMOS II front detectors are settled for 6.4 keV and 14.4 keV from this energy spectrum.

MIMOS II can be used for the depth selective analysis of a certain category of samples where the surface layers of interest have a thickness of several tens of Angstroms up to a couple of hundred Angstroms. The depth selectivity, which is certainly limited in respect to conversion electron Mössbauer spectroscopy (CEMS), is achieved by detecting in backscattering geometry both 6.4 keV X-rays and the 14.4 keV Mössbauer radiation simultaneously, as well as the transmission spectrum in cases of thin samples. For pure iron and stainless steel, the cross-section for both radiations are comparable. Therefore, the selection should only work if the sample contains other chemical species like Al, Si or Ti. These other elements have different cross-sections for the 6.4 and 14.4 keV radiation. Figure 3.2 depicts the energy spectrum of the $^{57}\text{Co}/\text{Rh}$ source recorded at 173 K using MIMOS II. Simultaneous backscattering and transmission Mössbauer spectra recorded at room tem-

perature of an α -Fe ($25 \mu\text{m}$), aluminum ($100 \mu\text{m}$), and stainless steel SS-310 ($25 \mu\text{m}$) sandwich is shown in figure 3.3. The 6.4 keV and 14.4 keV spectra were obtained in backscattering geometry and the other 14.4 keV in transmission geometry. This experiment demonstrated that most of the 6.4 keV backscattered radiation cannot reach the stainless steel foil but the 14.4 keV radiation does.

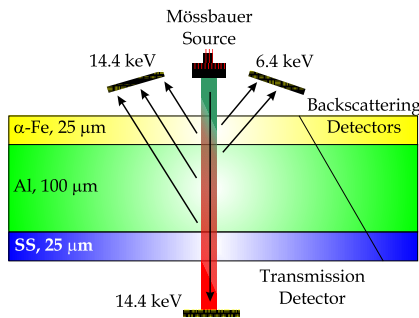


Figure 3.3: Demonstration of the depth selective surface analysis. Experimental setup: 14.4 keV in standard transmission geometry and both 6.4 keV and 14.4 keV in backscattering arrangement.

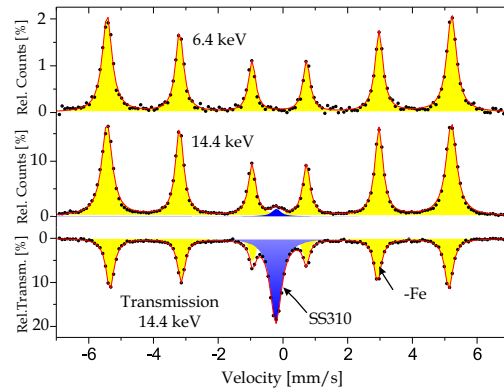


Figure 3.4: Simultaneously recorded backscattering and transmission room temperature Mössbauer spectra of a Fe /Al/SS ($25/100/25 \mu\text{m}$) sandwich. The 6.4 keV and 14.4 keV spectra were obtained in backscattering geometry and 14.4 keV in transmission geometry.

The detector of MIMOS II used for calibration was moved from inside the sensor head. It was placed behind the sample to record a 14.4 keV Mössbauer transmission spectrum. Simultaneously backscattering spectra were obtained. The 6.4 keV radiation emitted resulted from fluorescence of the inner shell electrons of the iron atoms in the sample. The γ -radiation emitted by Mössbauer effect by the nucleus increases the cross-section of the fluorescence. Therefore, it is possible that there is a coincident effect of the Mössbauer effect (14.4 keV) and the fluorescence ("6.4 keV Mössbauer spectrum"). Indeed, all "6.4 keV Mössbauer effect signal" should be faced up, since the non-resonant (6.4 keV fluorescence) lines are always emitted from the sample to the detectors. Unfortunately, the 6.4 keV spectrum at transmission geometry could not be distinguished from noise because of the high activity of the Mössbauer source. Typical 6.4 keV and 14.4 keV differences in the Mössbauer spectra obtained on Mars is proposed as further work to the scope of this thesis (chap. 7).

Another depth-selective Mössbauer analysis was done only with backscattered and transmitted 14.4 keV radiation. A glass bead sample, prepared

from magnetite (geochemical standard named $JSS812_3$) by the Chemical Laboratory from Companhia Vale do Rio Doce (CVRD) in Vitória, Brazil, was analyzed simultaneously in both geometries by MIMOS II. The obtained Mössbauer spectra show two doublets assigned to Fe^{3+} and Fe^{2+} (fig. 3.5). In transmission geometry the area of Fe^{3+} is equal to 89%, while in backscattering it is equal to 93%. The Fe^{2+} is, therefore, concentrated at the center of the glass bead sample, should no counting saturation of the Fe^{3+} occur. Fe^{2+} phase was not reported in glass bead samples [Mat 89] and this fact was associated to imprecisions in chemical analysis of iron ores by X-ray fluorescence, as reported by CVRD (e.g., [Sil 04]).

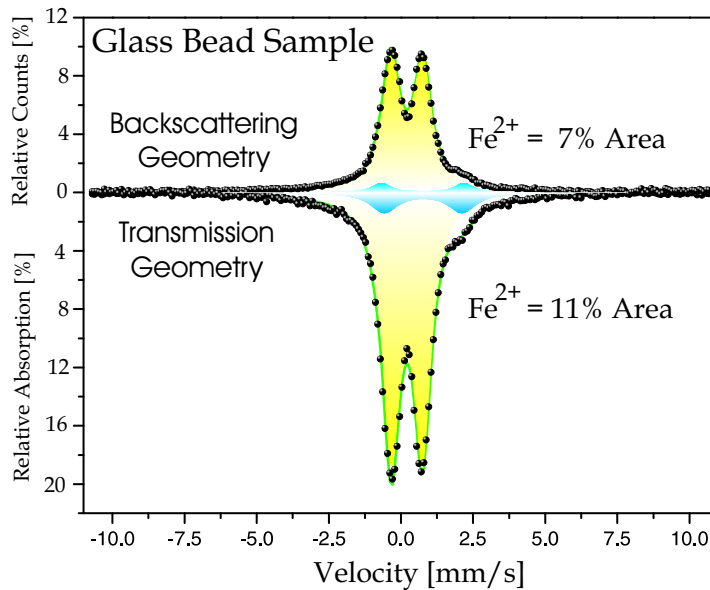


Figure 3.5: MIMOS II analysis in a glass bead sample.

On MER, the sensor head is located at the end of the Instrument Deployment Device (IDD) and the electronics board is located in an electronics box inside the rover body. On Mars Express Beagle-2, the sensor head was mounted on a robotic arm integrated to the Position Adjustable Workstation (PAW) instrument assembly. The sensor head also contains a contact plate and a temperature sensor. The contact plate is used together with the IDD to apply a small pre-load when it places the sensor head, holding it firmly against the target. Figure 3.6 shows a microscope image recorded from a MIMOS II nose print in the martian soil. The electronics board contains power supplies and conditioners, the dedicated CPU (a 8051 type microprocessor), different kinds of memory, firmware, and associated circuitry for instrument control and data processing. Figure 3.7 presents an image of the navigation

camera where the Mössbauer contact ring can be seen.¹

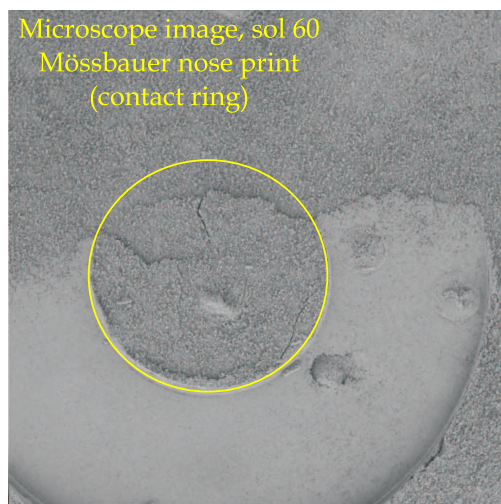


Figure 3.6: Mössbauer nose print image recorded by the microscope onboard *Spirit* on sol 60. The circle in yellow illustrates the analyzed region of the soil.



Figure 3.7: The region called "Last Chance" can be seen in the background at upper left in this navcam image. In the foreground, *Opportunity* examines its tool turret. The "wrist" of its robotic arm is behind the turret. The rock abrasion tool is pointed to the left; MIMOS II is pointing upward in the image. The alpha particle X-ray spectrometer is pointing to the right.

3.2 Mössbauer sources, shielding, and collimator

The highest possible source activity is desirable, with the constraint that the source line width should not increase significantly over the expected 7 months of the interplanetary flight, and the 9 to 12 months duration of the mission. Calculations and tests indicate an optimum specific activity for ^{57}Co at 1 Ci/cm^2 [Gum 88, Evl 93]. Sources of 330 mCi with an extremely narrow source line width (< 0.13 mm/s at room temperature), were produced by Cyclotron Co. Ltd. (Russia) in custom made space-qualified Ti-holders and tested successfully. They were mounted in flight instruments approximately 90 days prior to launch. No additional line broadening will result at lower

¹This picture is available in Mastro program that can be downloaded at <http://marsrovers.nasa.gov>.

temperatures on Mars with the rhodium matrix. An effective shielding of the detector system from direct and cascade radiation from the $^{57}\text{Co}/\text{Rh}$ source is very important. A graded shield consisting of concentric tubes of brass, tantalum, and lead was used. The thickness and the shape of different parts of the shielding were optimized so that nearly no direct 122.2 keV radiation (emitted by the ^{57}Co) is in a direct line with the detectors. The shielding also acts as the collimator which fixes the diameter of the target that is illuminated by the incident radiation. This diameter is as large as possible to minimize experiment time within the constraint of acceptable cosine smearing [Kli 92]. The larger the irradiated area, the higher are the counts, and therefore better measurement statistics for a given source activity can be achieved. Nevertheless, the cosine smearing effect [Rie 69] can occur changing the backscatter Mössbauer spectral line shapes recorded with higher velocity.² The measure used for acceptable cosine smearing was the ability to reliably resolve the strongly overlapping spectra of hematite and maghemite in a 1:1 mixture of those oxides. A series of experiments with this mixture and the pure oxides were conducted at constant source intensity and variable collimator radius [Sch 01]. The spectra were analyzed using the fitting routine developed by Held [Hel 97].

3.3 Drive system

The simplest way to meet volume and weight constraints was to scale down the drive systems built for laboratory instruments during many years [Kan 64]. A drive system which was constructed has about $\frac{1}{10}$ the size of a standard laboratory system. It has a diameter of 22 mm, a length of 40 mm, and ~ 50 g mass [Teu 94]. The MIMOS II design is based on a rigid tube connection between drive and the velocity pick-up coils in the double-loudspeaker arrangement with good electrical and magnetic shielding between the two coils to avoid crosstalk. The intense main $^{57}\text{Co}/\text{Rh}$ source is mounted on one end of the tube, and the weaker source for the reference absorber is mounted on the other end. The short tube guarantees a fast transfer of information with the velocity of sound in the aluminum and thus a minimum phase lag and a high feedback gain margin. Fortunately, and despite the increase of unwanted crosstalk resulting from the smaller distance between the coils, the relative contribution of crosstalk is still less than 0.01% in the frequency domain of the triangular waveform and is, therefore, negligible (e.g., [Kli 03]). The system is equipped with SmCo permanent magnets and was optimized

²See fig. 5.3 for an example.

to give a homogeneous and high magnetic field in the coil gaps [Teu 94].

The drive operates at a nominal frequency of ~ 24 Hz. This low frequency allows a broad bandwidth for the closed loop system, and good performance with a triangular reference signal, but requires rather soft Kapton springs. As a consequence, rotation of the drive from horizontal to vertical position in Earth gravity leads to a shift of about 0.4 mm from the equilibrium position of the tube. However, the resulting non-linearity between velocity and pick-up voltage remains $< 0.1\%$ at room temperature. Although this shift could be compensated by a DC current, no correction is needed for a mission to Mars where the gravity forces are smaller by a factor of ~ 3 . In order for the drive to operate under expected Martian surface temperatures (153 - 293 K), it was necessary to degrade the linearity to $\sim 3\%$. The design provides limiters to avoid destruction of the Kapton springs during the large accelerations associated with launch and landing. Vibration and shock tests of the drive system with levels up to, and slightly exceeding the specifications for both MER-NASA and Mars Express-ESA missions were successfully performed [Kli 03].

3.4 Detector system and electronics

The main disadvantage of the backscatter measurement geometry employed by MIMOS II is the secondary radiation caused by primary 122.2 keV radiation from the decay of ^{57}Co . To reduce the background at the energies of the 14.4 keV ray and the 6.4 keV X-ray lines, a detector with good energy resolution is required. Four Si-PIN-diodes with a (10×10) mm^2 active area were selected as detectors [Wei 92, Hel 93] instead of gas-counters as considered by other authors [Pri 90, Agr 92], for extraterrestrial purposes. A detector thickness of about $400 - 500 \mu\text{m}$ was a good choice. The energy resolution is $\sim 1.0 - 1.5$ keV at room temperature, and it improves at lower temperatures. The efficiencies at 6.4 and 14.4 keV are nearly 100% and about 70%, respectively [Hel 93]. The 100 V DC bias voltage for the detector diodes is generated by high frequency cascade circuitry with a power consumption of less than 5 mW. Noise contributions are minimized by incorporating a preamplifier-amplifier-SCA system for each individual detector. In addition to the four detectors used to detect backscattered radiation from the sample, there is a fifth detector to measure the transmission spectrum of the reference absorber. Sample and reference spectra are recorded simultaneously, and the known temperature dependence of the Mössbauer parameters of the reference absorber can be used to give a measurement of the average temperature

inside the sensor head, providing a redundancy to measurements made with the internal temperature sensor.

3.5 Temperature measurement

MIMOS II has three temperature sensors (Analogue Devices AD590): one on the electronics board in the rover/lander warm electronics box and two on the sensor head. One temperature sensor in the sensor head is mounted near the internal reference absorber, and the measured temperature is associated with the reference absorber and the internal volume of the sensor head. The other thermometer is mounted outside the sensor head at the contact ring assembly. It gives the approximate temperature for the sample on the Martian surface. This temperature is used to route the Mössbauer data to the different temperature intervals (maximum of 13, with the selectable temperature range) assigned in specific memory areas. An example of a laboratory overnight experiment on Mars is shown in figure 3.8 for 12 temperature intervals using the CCT as the target. In case of contact-ring temperature sensor failure, the internal temperature sensor would be used (software selectable). Laboratory Mössbauer lines for the CCT, which is fixed on the rover/lander, are sharper than those lines from the Mössbauer spectra recorded on Mars on the same CCT magnetite. The reason is that in the laboratory the temperature does not vary as much as 10 °C. This range is fixed to accumulate the Mössbauer spectrum. This situation is more clear for the internal calibration sample. During measurements, a temperature log is acquired for all three sensors. Temperature measurements are done in a given frequency, software selectable, from minimum of ~ 10 seconds to maximum ~ 40 minutes. The higher the integration time, the smaller this time frequency. MIMOS II can accumulate up to 256 temperature records corresponding to a total integration time of ~ 21 hours.

3.6 Operation modes and software

MIMOS II can be operated in six different modes depending on the nature of the measurement requirements:

Mössbauer temperature-dependent mode: Mössbauer sample and reference spectra are collected and stored as a function of up to 13 temperature intervals. The temperature ranges are variable and can be changed during mission operations;

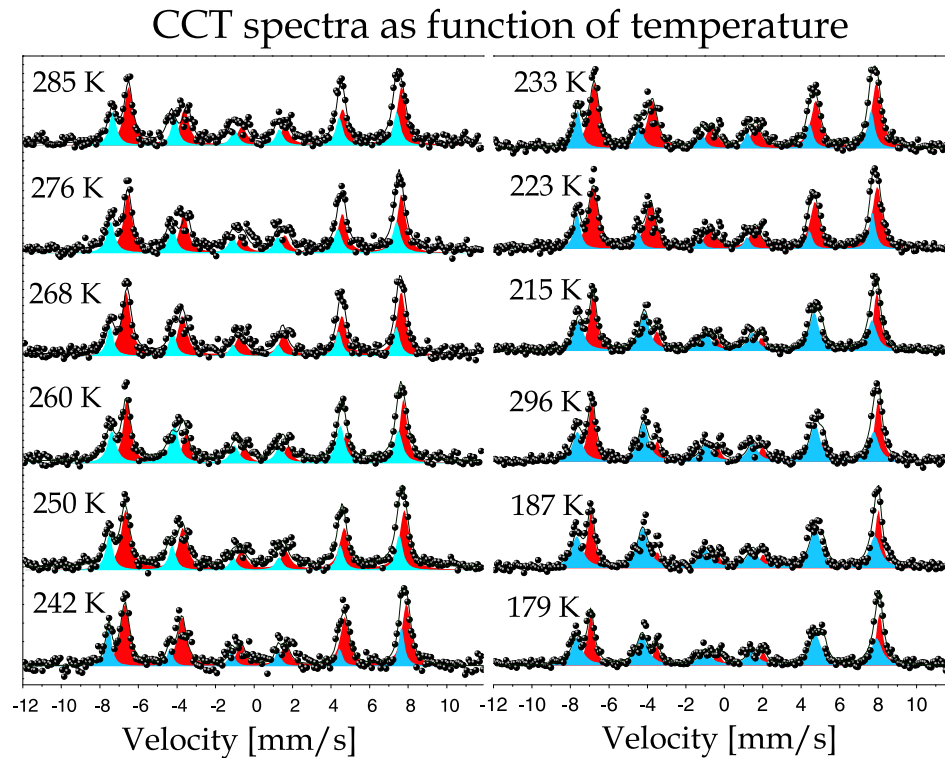


Figure 3.8: Mössbauer spectra of the compositional calibration target (CCT) as function of typical Martian temperature. The CCT is a magnetite disk installed in the MER rover’s deck. Widening of these lines were found on Martian measurements, as expected, resulting from the accumulation of the data given in a 10 °C range (see fig. 3.9).

Mössbauer temperature independent mode: Mössbauer and reference spectra are collected irrespective of the sample or reference temperature;

Energy mode: PHA spectra are collected to determine detector performance and to make changes in energy-window settings;³

Engineering mode: The drive differential signal is collected to determine the velocity drive performance;⁴

Standard mode: This mode is used for normal operations. It consists of the engineering, energy, and Mössbauer temperature dependent modes commanded sequentially; and

Idle mode: In this mode, no operations are performed.

³Details are given in sec. 3.7.1.

⁴See sec. 3.7.5 and fig. 3.14.

3.6.1 Data structure of MIMOS II

The MIMOS II consists of 512 velocity channels (3 bytes/channel). One temperature interval consists of five Mössbauer spectra (one for each detector or the sum of 14.4 and 6.4 keV obtained by pairs of front detectors; and only 14.4 keV from the reference detector). There are 13 temperature intervals with selectable width. Therefore, MIMOS II can accumulate up to 65 Mössbauer spectra during one experiment session. All Mössbauer and energy spectra as well as engineering and the temperature data taken during this session are stored in a volatile SRAM memory (128 kB) on the MIMOS II electronics board. Firmware parameters and the instrument logbook are stored in the non-volatile memory ferroelectric RAM (FRAM) on the electronics board. There are three individual FRAMs on the MIMOS II electronics board with three identical copies of these parameters to ensure parameter integrity during interplanetary data transmission. The copies are verified and compared to each other from time to time to verify they are identical. If one copy deviates from the other two, it will be replaced by a copy of the two other still identical parameter sets. All operational parameters can be adjusted during mission operations. To minimize risk of data loss because of power failure or other reasons, the Mössbauer data are copied to a non-volatile EEPROM memory every 9 minutes (software selectable). As the size of the EEPROM is smaller than the SRAM, the EEPROM can accumulate only up to ten Mössbauer spectra as a subset of the data from the SRAM. These spectra are obtained from the SRAM according to a pre-defined summation strategy.

3.7 MIMOS II calibration

As discussed, the MIMOS II sensor head (figures 3.1 and 3.11) carries the Mössbauer drive with the analogous part of the drive unit, the $^{57}\text{Co}/\text{Rh}$ Mössbauer source, the radiation collimator and shielding, the four PIN-diode detector channels including pulse amplifiers, and one reference detector channel to monitor the velocity of the drive using a weak $^{57}\text{Co}/\text{Rh}$ source and should also have a well known Mössbauer reference absorber in transmission geometry. In space rovers (NASA:MER Mission) and landers (European Space Agency - ESA:Beagle 2 mission) a calibration target to check the front detectors and related systems was provided. This calibration target is a thin slab of magnetite-rock placed where it was directly measured by the instrument soon after landing (*Opportunity*), as well as later in the mission if necessary (*Spirit*). A composition calibration target measurement made by MIMOS II onboard *Opportunity* rover on Mars is shown in figure 3.9.

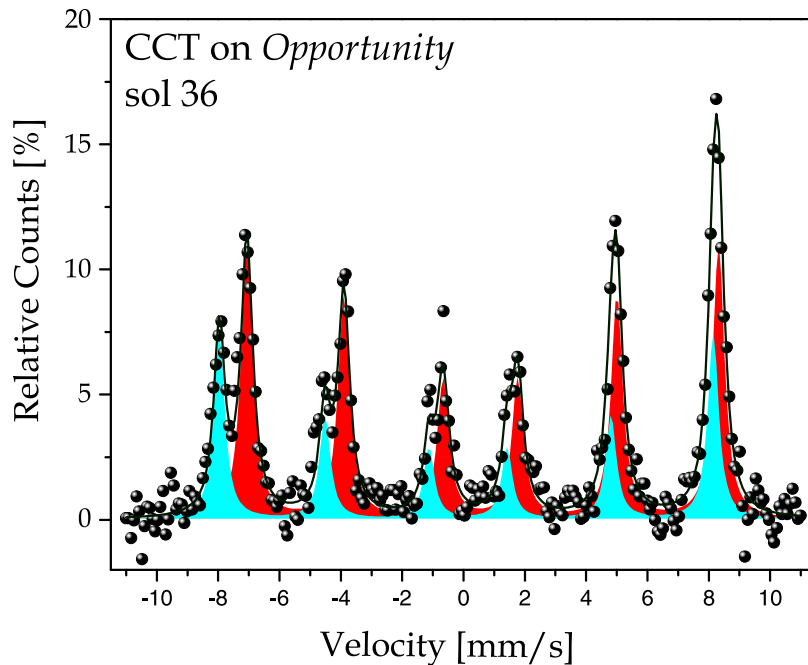


Figure 3.9: The Mössbauer spectrum recorded during 1h and 5min on the compositional calibration target by the *Opportunity* MIMOS II sensor head on sol 36. Temperature during this measurement oscillated from 258 K to 261 K. The measurement started on 11:46 A.M. (1146 local solar time, LST-B).

Mössbauer spectroscopy reveals temperature dependent characteristics of the sample, if any takes place. As discussed in section 2.3, some effects like super-paramagnetism and Morin transition can be followed by temperature dependent Mössbauer measurements. On Mars surface, from sunshine to sunset, temperature changes as much as 120 °C (figures 3.10 and 6.7). The temperature variation for one spectral accumulation interval will not be larger than about ± 10 °C. When larger temperature variations occur, spectra for different ranges are stored separately, resulting in the total data volume (depending on the number of temperature intervals required), and a decrease of statistical quality for the individual subspectra. Nevertheless, a summation of particular subsequent ranges can be performed and analyzed, increasing the statistical quality, when plausible. Therefore, information can be obtained on temperature dependent transitions (such as super-paramagnetism and MT) against statistical quality of the recorded spectra. Most silicates show no change at Mars temperatures. Mars hematite, if all the conditions discussed in section 2.3.4 hold, may undergo MT. Fine-grained (nanoparticles) super-paramagnetic relaxation may also be seen. This fact was considered for Martian data analysis (see sec. 6.4 for detailed discussion).

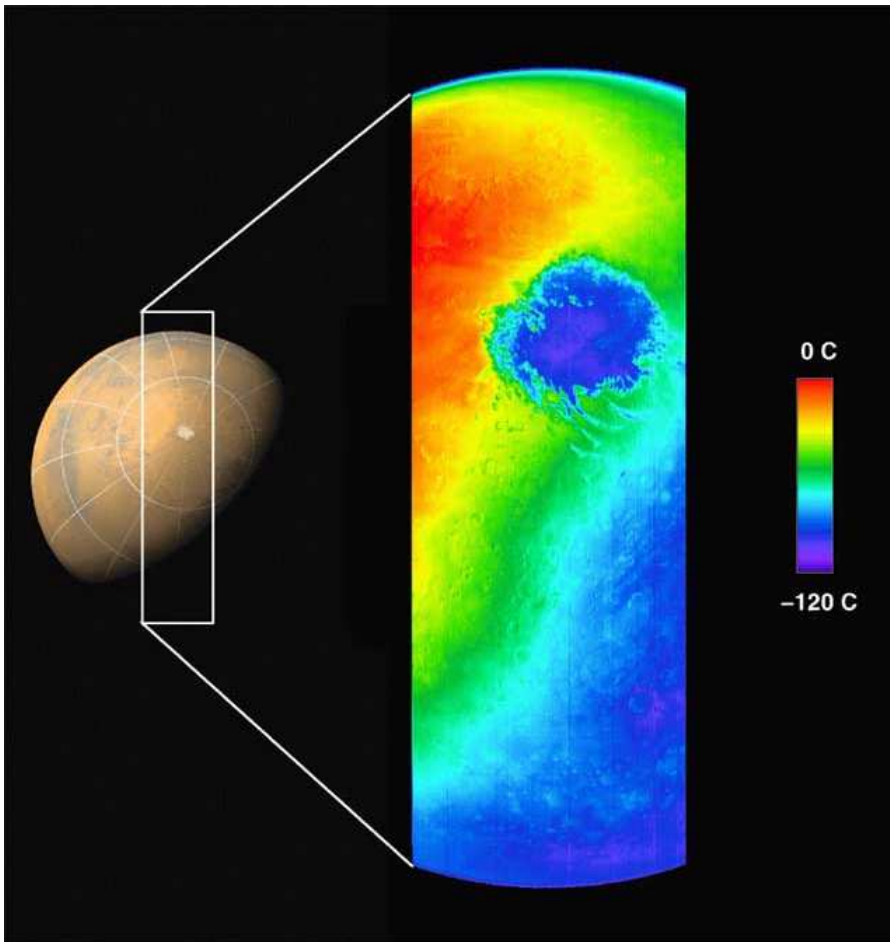


Figure 3.10: Mars temperature recorded by the Thermal Emission Spectrometer of the orbiter Mars Global Surveyor (*Courtesy: JPL-NASA*).

Therefore, both external (CCT) and internal calibration samples (e.g., enriched $\alpha\text{-Fe}$, Fe_2O_3 , and $\alpha\text{-Fe}_2\text{O}_3$), and temperature records were measured to check MIMOS II engineering working.

3.7.1 Energy calibration

Careful energy calibration for each detector was done to achieve optimal detection rate. Each sensor head was temperature cycled (153 K - 293 K; the typical Martian temperature range). During cycling, energy spectra were measured (fig. 3.2). As a result of analysis of these spectra, optimal firmware parameters were calculated for each detector and each temperature window.

During operation, instrument firmware adjusted those parameters depending on temperature, ensuring optimal performance as temperature changes.

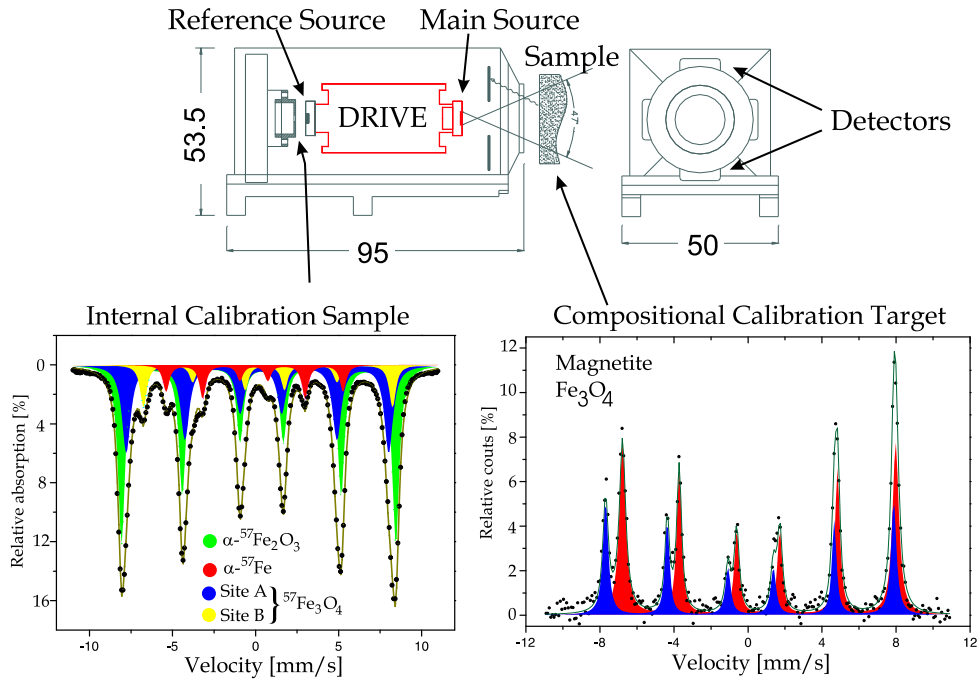


Figure 3.11: Drawing of MIMOS II with positions of both reference and main $^{57}\text{Co}/\text{Rh}$ sources showed in detail. A possible reference sample (internal calibration sample) and a spectrum from the compositional calibration target (CCT, magnetite) for the Mössbauer spectrometer on board of the Mars Exploration Rovers (MER) are also depicted.

3.7.2 Velocity calibration

The interpretation of acquired Mössbauer spectra is impossible without knowing precisely the drive velocity. Mössbauer drive velocity calibration for MIMOS II is rather straightforward and done in three different ways, ensuring redundancy. For example, prior to an interplanetary flight each individual drive system was calibrated by measuring in backscattering mode an α -Fe foil standard. A maximum drive velocity was preset by firmware. Fitting the acquired Mössbauer spectrum using the well known parameters of the α -Fe foil then yielded the real velocity. During the mission, the magnetite CCT will be measured in several runs to verify the functionality of MIMOS II. The well known Mössbauer parameters of magnetite can be used for velocity calibration again. This kind of measurements have been done already in the

laboratory with the flight units as a function of temperature, to be used as reference for the measurements on Mars (fig. 3.8). The primary method for velocity calibration is the internal reference target and detector arranged in transmission geometry (fig. 3.11). The reference target is a mixture of Fe^0 (metallic iron, 30% enriched ^{57}Fe); Fe_3O_4 (magnetite), and $\alpha-Fe_2O_3$ (hematite) 95% enriched ^{57}Fe .⁵ Its Mössbauer spectrum is measured automatically during each backscattering measurement. Each component of the reference target has well-known Mössbauer parameters, so that fitting of reference spectra enables velocity calibration for each individual measurement done in backscatter geometry, ensuring that the actual drive velocity is always well-defined, regardless of prevailing environmental conditions.

Once on outdoor terrestrial applications it is always possible to make a calibration by using a known sample directly on MIMOS II main detectors. Therefore, for outdoor applications, the reference detector was removed from the MIMOS II interior and used for transmission measurements. This is an additional possibility on air pollution and on other thin sample studies (e.g., deep-selective analysis shown in fig. 3.4).

3.7.3 Internal calibration sample

For all given sample measurements, MIMOS II also records a transmission spectrum as reference spectrum. This reference measurement taken on Mars on a well-known sample, placed inside the instrument, has a very specific dependence of the hyperfine parameters on the range of Mars' surface temperature. This reference sample should also present magnetic phases to check the operational status of the drive unit at high velocity ranges. The functionality of the spectrometer can also be measured in terms of line widths and the capacity to distinguish close spectral features for different sites, also at different temperatures. A sample that offers these specifications would be a mixture of hematite ($\alpha-Fe_2O_3$) and magnetite (Fe_3O_4). Moreover, these oxides have well-known properties and are chemically stable under Mars temperatures. In particular, well crystalline and pure hematite has the Morin transition at such temperatures (sec. 2.3.4).

The internal calibration sample is an enriched iron oxide film together with an enriched 25 μm $\alpha-Fe$ foil. The iron oxide (95 % ^{57}Fe enriched) was ground using agate mortar to obtain a fine powder. The powder (20 mg) was

⁵See sec. 3.7.3 for details.

taken in a glass container and about 40 mL ethyl alcohol was added to the powder. Aluminium oxide discs (6 mm diameter) were placed at the bottom of the glass container, with alcohol and the powder material. The solution was heated at 50 °C for 30 minutes (seven such heating cycles were used). Heating cycles are useful to increase the rate of evaporation of alcohol, and also to stir the solution, in order to have better deposition of particle on aluminium discs. When the oxide particles settle down at the bottom of container, they also get deposited on aluminium oxide discs and form an almost uniform layer of powder on aluminium discs. Once the alcohol is evaporated, the discs with the deposited powder material are taken out of the glass container and coated with SCC3 conformal coating for particle fixation. The enriched ^{57}Fe oxide disks were dried at room temperature for 4 days. Transmission Mössbauer spectra were recorded from room temperature down to 130K (lowest expected Mars temperature at the landing sites) in constant acceleration mode, using a $^{57}\text{Co}/\text{Rh}$ source. The Mössbauer spectra were analyzed assuming overlapping of different components (see table 3.1 and fig. 3.11). Additionally, $\alpha\text{-Fe}$ or stainless steel can be used together with the ^{57}Fe oxide, increasing the lines to be checked during the mission (see fig. 6.9). This spectrum was used for measurement validation of all Mössbauer experiments on Mars surface.

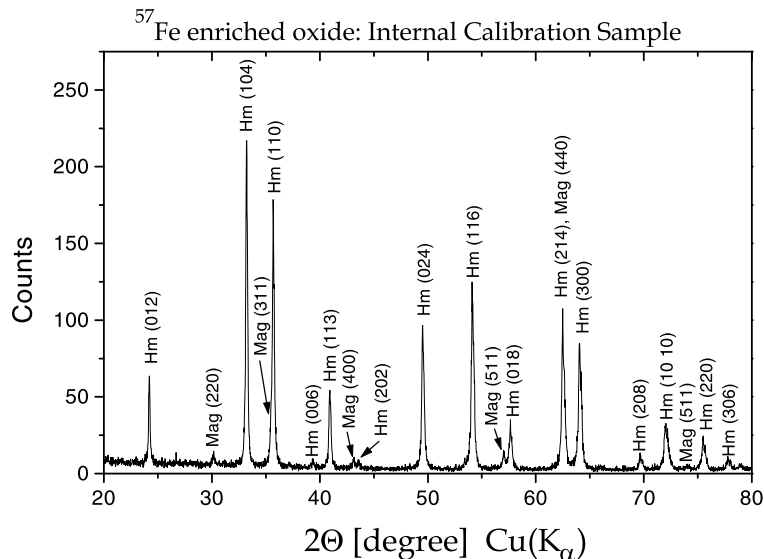


Figure 3.12: Powder X-ray diffraction pattern of the internal calibration sample recorded in a Siemens D500 diffractometer using a $\text{CuK}\alpha$ radiation source.

In addition to the internal calibration sample, a compositional calibration

Table 3.1: Least-squares fitted Mössbauer parameters from the internal calibration sample. Note the Morin transition between 298K and 235K.

Temperature [Kelvin]	δ [†] [mm/s]	Δ [mm/s]	Γ_{exp} [mm/s]	B_{hf} [T]	Area [%]	Phase	
Enriched Fe-oxide Material	298	0.40	-0.19	0.55	51.2	53.8 \pm 0.4	α -Fe ₂ O ₃
		0.32	-0.20	0.67	48.8	33.2 \pm 0.4	Site A
		0.78	0.15	0.54	46.4	13.0 \pm 0.1	Site B magnetite
	235	0.42	0.30	0.44	53.0	61.2 \pm 1.3	α -Fe ₂ O ₃
		0.33	-0.07	0.55	49.9	27.5 \pm 1.6	Site A
		0.88	0.19	0.43	48.1	11.3 \pm 0.7	Site B magnetite
	223	0.42	0.32	0.43	53.1	65.6 \pm 1.4	α -Fe ₂ O ₃
		0.31	-0.05	0.49	49.9	21.6 \pm 1.7	Site A
		0.87	0.17	0.48	48.4	12.8 \pm 0.9	Site B magnetite
	208	0.43	0.33	0.43	53.2	64.7 \pm 0.9	α -Fe ₂ O ₃
		0.30	-0.02	0.46	50.0	19.8 \pm 0.9	Site A
		0.86	0.24	0.56	48.5	15.6 \pm 0.6	Site B magnetite
	190	0.44	0.34	0.43	53.3	64.5 \pm 1.1	α -Fe ₂ O ₃
		0.31	-0.10	0.47	50.1	20.0 \pm 1.3	Site A
		0.86	0.19	0.57	48.7	15.5 \pm 0.8	Site B magnetite
	165	0.44	0.34	0.44	53.3	66.8 \pm 1.1	α -Fe ₂ O ₃
		0.33	-0.03	0.47	50.1	18.1 \pm 1.2	Site A
		0.87	0.22	0.56	48.7	15.1 \pm 0.8	Site B magnetite
	130	0.47	0.34	0.43	53.7	65.3 \pm 1.4	α -Fe ₂ O ₃
		0.35	0.02	0.48	50.5	20.3 \pm 1.8	Site A
		0.89	0.21	0.59	49.3	14.4 \pm 1.1	Site B magnetite

Note: [†] related to α -Fe; δ , Δ and Γ errors = 0.02 mm/s; B_{hf} errors = 0.1 Tesla.

target (a magnetite-rock disk) was installed in the rover/lander deck. This target, as discussed, is designed to be used as a reference sample to the front detectors and main source. Measuring this sample the expected quality of the MIMOS II records can be checked, as well as efficiency of the front sample face detectors (figs. 3.8, 3.9, and 3.11).

3.7.4 FIDO trials

Field Integration Design Operations (FIDO) is a prototype Mars rover devoted to "blind" science operation tests. It is designed to evaluate the most efficient ways of traversing across diverse terrains while conducting

reconnaissance-level field. This allows site characterization, finding, approaching, and placing analytical instruments and a drilling system onto rock targets; that characterize in detail the sample material that is representative of the sites traversed. This rover was designed to simulate the Athena Payload for the 2003 Mars Exploration Rovers mission [Arv 02]. During May 2001 and August 2002, FIDO tests were deployed at the Jet Propulsion Laboratory facilities and in American deserts (California desert - Mojave - and in an Arizona desert). Those testing sites were blind to test participating scientists and engineers. Nine samples, selected by NASA, were sent to Mainz for the characterization in the laboratory and also to other payload groups. The objective of these field tests is to simulate real-time surface operations on the mission systems (both software and hardware) and checking upload sequences to the rover.

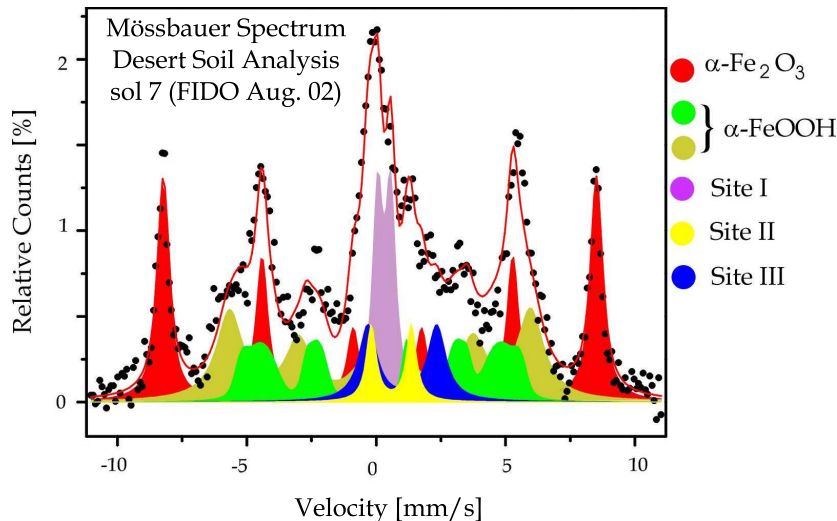


Figure 3.13: Mössbauer spectrum recorded during sol 7 of FIDO trial test from the Arizona desert soil. Hematite, goethite and iron-bearing silicates were detected.

A typical long-integration Mössbauer measurement on Mars for MER mission takes approximately 12 hours. This measuring time could be determined according to Mars-analog samples measured during FIDO test and in laboratory studies, considering the intensity of the γ -rays source. For this purpose, samples containing the most expected iron-bearing minerals with comparable iron-concentration of Martian soil and rocks (table 6.5) were used.⁶ For FIDO tests only room temperature Mössbauer spectra were recorded.

⁶Cf. app. A.

Table 3.2: Mössbauer parameters for the desert soil (Arizona State) measured for the 7th FIDO simulated Mars day (sol 7). The preliminary iron-phase identification is given.

δ^\dagger	Δ	B_{hf}	Area	Preliminary Phase Identification
[<i>mm/s</i>]	[<i>mm/s</i>]	[<i>T</i>]	[%]	Confidence: 1.Sure; 2.Tentative; 3.Uncertain
0.40	-0.25	51.9	30.9	hematite ¹ (well crystallized, large grain sizes)
0.37	-0.22	36.1	27.5	goethite ¹ (well crystallized, large grain sizes)
0.42	0.50		11.6	phyllosilicate ² , lepidocrocite ³
0.70	1.55		4.5	Fe-smectite ² , garnet (melanite) ³ , ilmenite ³
1.12	2.66		8.1	phyllosilicate ² , clinopyx (augite) ² , ilmenite ³
$\langle \delta \rangle$	$\langle \Delta \rangle$	$\langle B_{hf} \rangle$	Area	
[<i>mm/s</i>]	[<i>mm/s</i>]	[<i>T</i>]	[%]	
0.41	-0.24	distrib.	17.4	goethite ¹ (poorly crystallized, Al-substitution)

Note: \dagger related to $\alpha\text{-Fe}$; Bkg = 1702090 counts; Fe-conc. (APXS) = 6.4%wt.

Ratios: $\frac{Fe^{2+}}{Fe_T} = 12.6\%$; $\frac{(Oxides+Oxide-hydroxides)}{Silicates} = \frac{30.9+44.9}{24.2} = 3.13\%$

3.7.5 Health checks

Prior to launch, during the interplanetary flight and shortly after landing a set of measurements were undertaken to check if MIMOS II electronics and mechanics survived the vibrations and accelerations that all payload systems are submitted to during the Delta-II rocket launch. During the interplanetary flight, a noisy Mössbauer spectrum was obtained for both instruments (fig. 3.14). Several hypotheses were formulated to describe the cause of the problem. They were from vibrations caused by the cooling fluid pumping system in the spacecraft to some mechanical blocking of the drive's movement. The problem was minimized using a higher frequency for the drive, decreasing its movement amplitude. After the complex the atmospheric entry, the decent and the landing activities, the instrument has to be checked to verify if the aggressive landing damaged it. The health check was the first planned Mössbauer measurement done on Mars. The first health check was performed with ~ 60 Hz of drive's frequency (fig. 3.15). Once it worked fine, the instrument was set up to work again with the nominal frequency (~ 24 Hz). The experimental protocol for the first health check included several velocity scales at the same drive's frequency and recording time.

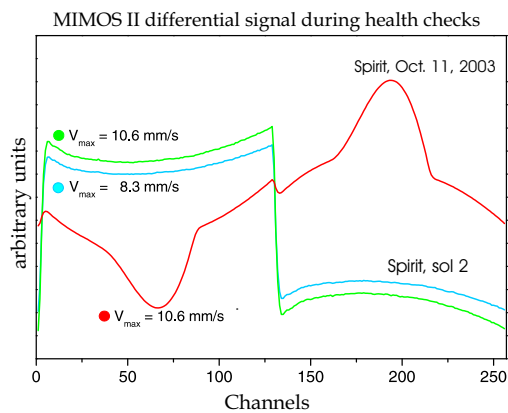


Figure 3.14: Differential signal of the MIMOS II drive recorded during health check exercises performed onboard *Spirit* on Oct. 11, 2003 during flight to Mars, and after landing (sol 2).

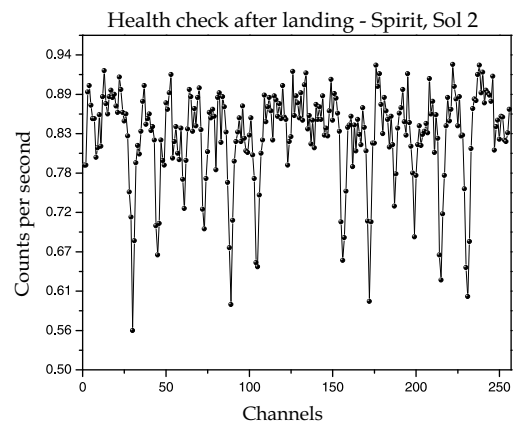


Figure 3.15: Health check of the MIMOS II installed onboard *Spirit* recorded during 900 seconds of sol 2 confirming the instrument and the related systems survived the landing.

Chapter 4

Analysis of the Mössbauer spectrum

This chapter is devoted to present some techniques proposed to overcome usual difficulties in the conventional Mössbauer spectral analysis. The proposed solution uses the so-called intelligent systems of genetic algorithms, fuzzy logic, and artificial neural networks. These techniques are presented to some extent in this chapter. Details on the implementation of each technique is also discussed.

4.1 Introduction

The spectral analysis (e.g., of a Mössbauer spectrum) can be time-consuming and may be subject of a specialist. In the usual analysis procedure the ASCII spectrum file (raw data) is tested against a fitting hypothesis. This hypothesis holds a given set of sub-spectral lines (for ^{57}Fe Mössbauer spectroscopy; singlets, doublets and sextets). Each sub-spectrum can be represented by a given set of parameters (e.g., peak position, full width at half maximum (FWHM), peak area) that can be iteratively improved by a least-squares fitting routine. Depending on the obtained results, a new hypothesis has to be considered. In this case, the initial fitting hypothesis (e.g., number and position of combined basic lines) has to be rebuilt; and the whole process is repeated. The obtained refined parameters should be compared with standard published parameters or with a standard sample. In mineralogy, frequently other technical data are used to support a given hypothesis. It should also be considered that, in a particular case, the published information could be a result of misinterpretation. This may be a problem for the mineral identification.

Literature, data base or standard samples should be and are generally used for comparison and identification purposes. In some cases, there are mineral phases with the same Mössbauer parameters at a given temperature (e.g., for room temperature Mössbauer measurement: akaganéite $\beta\text{-FeOOH}$ and lepidocrocite $\gamma\text{-FeOOH}$). In this situation, new measurements (e.g., different sample temperature) are required. This experimental setup produces differences in the Mössbauer spectrum of the studied sample making possible its correct identification. In some cases, data from other analytical techniques are required.

Since the fitting and the identification processes are time and effort consuming, and considering the large number of iron-bearing minerals already studied by Mössbauer spectroscopy, a complete suite for data analysis was implemented using genetic algorithms, fuzzy logic, and artificial neural networks. The sequence of this chapter describes general aspects of these automatic systems. The detailed implementation, application and results are discussed through the rest of the text. The use of artificial intelligence make possible the use of Mössbauer spectroscopy by non-specialists or in problems where the data analysis has to be done quickly; like in industry and in daily real-time surface operations of a mission to Mars. In the first case, the industry needs a fast analysis for their production process control. A mission like Mars Exploration Rover has a daily interaction with their payloads and need quick data analysis. The planning of a next sol activity is done in a few hours and the decision about the activity rover agenda considers the analysis of the data obtained in the "yestersol". The entire analysis has to be done as fast as possible.

In this chapter it is discusses the optimization process, both the least-squares and testing fitting hypotheses using some well-known expert systems. The implementation of data analysis systems based on these techniques was helpful for the proposed outdoor terrestrial and extraterrestrial applications.

4.2 Classical curve fitting

A Mössbauer spectrum is the plotting of the relative transmission (or scattered counts) as a function of Doppler velocity. The Mössbauer spectrum shows maximum resonance and therefore minimum relative transmission (or maximum counting for backscattering) at relative velocities where emission

and absorption lines overlap ideally. At high positive or negative velocities this overlap is negligible, the resonance effect practically nonexistent, i.e., the relative transmission (or absorption) yields the baseline.

Once the Mössbauer spectrum is obtained, computer routines are applied to extract the Mössbauer parameters of isomer shift (δ , in mm/s), quadrupole splitting (Δ , in mm/s), hyperfine magnetic field (B_{hf} , in kOe or Tesla) or their distribution values.

The ordinary analysis of a Mössbauer spectrum starts with the choice of a spectral model and initial values of the spectral parameters. An experienced analyst does this by an "eye fit" and use of a fitting program to improve the initial parameters. The main characteristics of the classical approach of a Mössbauer fitting procedure is the excessive human dedication required and the dependence on the specialist experience.

Investigation on precision and interlaboratory reproducibility of measurements of the Mössbauer effect in minerals [Dya 84] indicated that the possible causes for inaccuracy in Mössbauer data are both the experimental conditions and the inappropriate analysis. From the experimental point of view the imprecision comes from the counting statistics which can be minimized by through testing of the spectrometer, the long term drift of the equipment's drive, sample concentration, texture effects and electronic relaxation which can cause differences in peak amplitudes, preferred orientation in the samples during the preparation, and by calibration of the equipment. From the analytical point of view, imprecision comes from the overlap of one or more peaks of different subspectrum and errors in the guesses model for fitting, specially how many peaks can be fit and if there are differences in line widths and line intensities. Experimental Mössbauer standards are still an open discussion in Mössbauer spectroscopy and some alternatives have been proposed [Kuz 03].

In general, the steps of a conventional analysis are the following:

1. Create a model (number of line shapes);
2. Supply initial values of the Mössbauer parameters (an input file with the chosen line positions);
3. Run a fitting program to obtain better fitted Mössbauer parameters;
4. Evaluate the accuracy of the result (by the χ^2 value, by the analyst's experience, or other criteria);

5. If the evaluation in step 4 shows a nearly acceptable accuracy, then substitute the initial values by changing the model in step 1; otherwise, consider the results of step 3 as final.

This (usual) method consists of many repetitive interactions between the specialist and the fitting routines. There are, depending of the Mössbauer spectrum and the fitting hypothesis, two typical ways of doing the least-squares fitting: the site and the distribution analysis.

- Site analysis

In the case of well crystallized samples with grain sizes in micrometer scale or above, sharp Mössbauer spectrum lines can be obtained. The fitting become a simple combination of well defined lines shapes (e.g., Lorentzians).

The values of the parameters characterizing a Mössbauer spectrum are typically determined by adjusting these parameters by least-squares method, in which a curve is fitted to the measured points by the minimization of the function

$$\chi^2 = \frac{1}{n - n_p} \sum_{i=1}^n \frac{1}{\sigma_i^2} [N(v_i) - F(v_i)]^2, \quad (4.1)$$

where n is the number of measured points, n_p is the number of the parameters the values of which are to be determined, $N(v_i)$ is the measured spectral value at velocity point v_i and $F(v_i)$ is the sum of the values of Lorentzian functions at that point. The variance σ_i^2 is usually estimated by the measured value $N(v_i)$. Each Lorentzian function is of the form

$$L(v_i, \Gamma) = \frac{\Gamma}{2\pi} \frac{1}{v_i^2 + (\Gamma/2)^2}, \quad (4.2)$$

where Γ is the full width at half maximum (FWHM).

The value $F(v_i)$ of the function F at point v_i is computed as a linear combination of Lorentzian functions:

$$F(v_i) = \sum_{k=1}^{n_s} I_k L(v_i - \delta_k, \Gamma_k) + B, \quad i = 1, 2, \dots, n. \quad (4.3)$$

Here n_s is the number of spectral lines, I_k represents the intensity of the line k , δ_k is the rotation of the line k representing the middle point

of the line (i.e., the peak position), and Γ_k is the width of the line k . The symbol B stands for the value of background absorption. Several investigations on the analysis of Mössbauer spectra have been reported in detail the literature [Des 99].

- Distribution analysis

Some complex materials have spectra consisting of a superposition of large sets of unresolved elemental contributions. This may be a result of chemical variety, such as in phyllosilicates where, despite high crystallinity, the octahedral sites can accommodate a large arrangement of different cations.¹ Other reason can be the structural variety as in super-paramagnetic particles and quasicrystals that also leads to large sets of unresolved and superimposed elemental contributions.

In all cases, the Mössbauer spectra can be understood in terms of (quasi)continuous distributions of different sets of hyperfine parameters, which may include fluctuations in the local environments. Therefore, the distributions of hyperfine parameters hardly give distributions of local distortion or local chemical information. A typical example of a fitted Mössbauer spectrum from a "rainbow hematite" analyzed with a distribution of the hyperfine magnetic fields is given in figure 4.1 and the obtained distribution profile is shown in figure 4.2.²

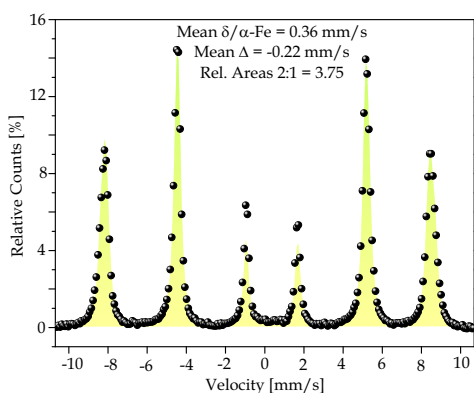


Figure 4.1: Mössbauer spectrum recorded at room temperature of a iridescent hematite. This sample is also known as rainbow hematite.

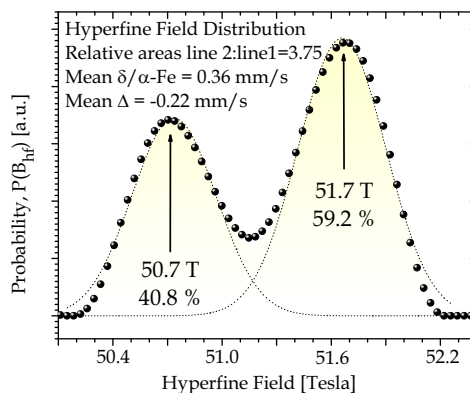


Figure 4.2: The distribution profile obtained for the hyperfine magnetic field.

¹See table A.15 for a list of these minerals.

²This hematite is also known as "iridescent" hematite. It was collected at the Espigão do Pico mine (CVRD), MG, Brazil.

4.3 Curve fitting using genetic algorithm

A genetic algorithm [Gol 89] is an iterative algorithm based on the idea of letting several solutions (individuals) compete with each other for the opportunity of being selected to create new solutions (reproduction). Each solution is represented as a string of binary digits (chromosome). New representations are created by pairwise exchanging bits in the binary representations of two parent solutions. Some of the bits in the new solutions may be switched randomly from zero to one or conversely (mutation). The algorithm starts with a randomly determined set of individuals (initial population) and iteratively generates new populations through the application of genetic operators (selection, cross-in-over, mutation and elitism or clone).

The quality of each parameter combination, i.e., the fitness of each solution, is defined as the weighted optimizing function (e.g., χ^2). The weighting is calculated as the ratio of the individual fitness and the sum of all fitness values of the individuals in the population. It is used as probability for an individual to be selected to the reproduction. Thus, individuals with larger fitness will be chosen with greater probability to the reproduction process. The iteration is usually stopped when the average fitness of the population starts to be saturated (fig. 4.3). This results from the fact that the genetic operators tend to favor those chromosome structures (list of fitting parameters), which corresponds to large fitness values. The convergence of the algorithm is usually improved by exploiting the so called "elitism" or "clone", in which the best individual in the old population replaces the worst in the new one.

The main advantage of the curve fitting using genetic algorithm is the possible way of treating different fitting hypotheses (number of Lorentzian lines) and the possibility of the relative complex Mössbauer spectrum to be fitted by a non-specialist.

The computer implementation of the genetic algorithm takes as its input two files: a file containing the measured absorption or backscattered values (raw data) and a file with the selected spectral model (possible number of singlets, doublets and sextets that better fit the Mössbauer spectrum). The maximum velocity is also given, considering the drive signal being linear.

Each parameter value to be determined is coded as an integer between the values 0 and $2^b - 1$, where b is the number of bits used in representing this integer value as a string of binary digits. The coding is achieved through defining minimal and maximal values for each parameter and dividing this interval to $2^b - 1$ sub-intervals. Hence the accuracy of the representation depends both on the number of bits used and on the selection of those max-

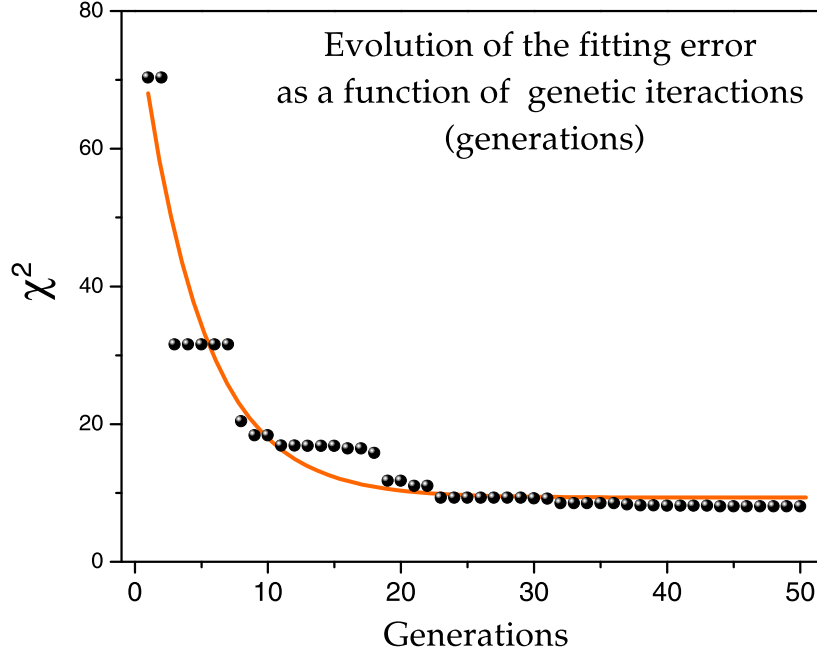


Figure 4.3: The evolution of χ^2 as a function of the fitting iterations (generations).

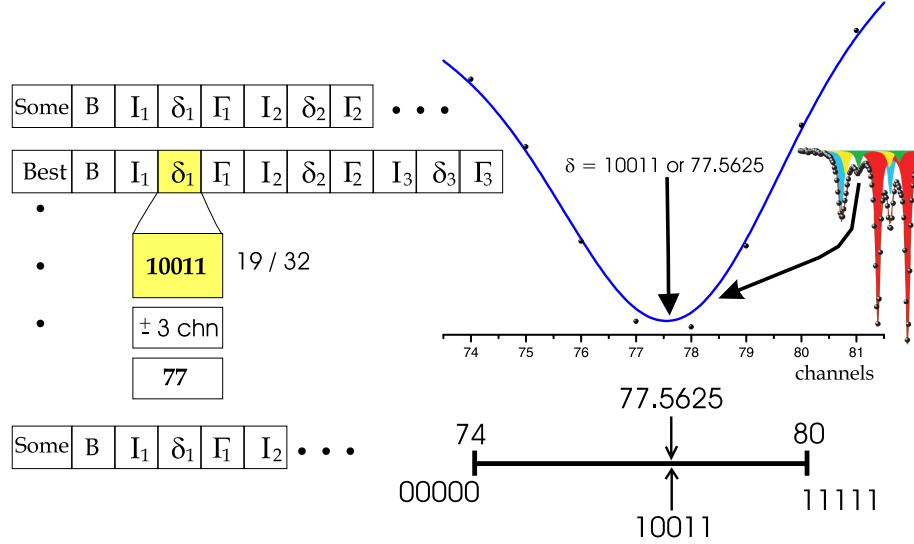
imal and minimal values. A chromosome of an individual is formed through concatenation of the binary strings representing the fitting parameter values.

For example, if the spectral model consists of one singlet and one doublet, then the string representing the chromosome is the concatenation of the binary representations of the coded values of the parameters B , I_1 , δ_1 , Γ_1 , I_2 , δ_2 , Γ_2 , I_3 , δ_3 and Γ_3 (as given in eq. 4.3), where the index 1 refers to the single Lorentzian line of the singlet and the indices 2 and 3 refer to the two Lorentzian lines of the doublets. In figure 4.4 the indices 1, 2, and 3 refer to the first three Lorentzian lines of one of the sextets of the internal calibration sample of MIMOS II measured on Mars (fig. 6.9).

The fitness of each individual resonance line is calculated as the inverse of the calculated χ^2 value (eq. 4.1). In this sense, the values of the Lorentzian functions at each velocity point along with the coefficients (intensities) in the linear combination are calculated (eq. 4.3). This requires decoding of the chromosome, i.e., extracting the parameter values from the binary string.

The implementation of the genetic algorithm takes the following steps:

1. (*Input*) In addition to the file containing the measured absorption or backscattered values (i.e., the Mössbauer spectrum), a spectral model should be used as a starting fitting routine. The spectral model consists



Resolution: $6/32 = 0.1875$ channels; Central channel: 77
 Peak position (in binary): 10011 and (in channels): 77.5625

Figure 4.4: The decoding of the peak position of a Lorentzian line fitted with genetic algorithm is presented. The genetic algorithm works with, for example, five binary digits. The peak position can assume any value between 74 (represented by 00000) and 80 (represented by 11111). Therefore, the six channels are divided into 32 or 2^5 segments. The peak position is between channels 77 and 78 (77.5625). The result of 10011 is equivalent to 77.5625 channels. The parameters B, I, δ and Γ are used in eq. 4.3.

of the calibrated maximal velocity and the positions of the absorption peaks, given as a separate list for each spectral component (i.e., one peak position for each singlet, two for each doublet and six for each sextet).

2. (*Background*) The background level and its standard deviation are evaluated on the basis of a given number of initial and final points in the spectrum.
3. (*Parameter intervals*) The parameter intervals are determined on the basis of the given peak positions, of the computed background level and of the given maximum spectral velocity.
4. (*Initial population*) A set of solutions (e.g., 100) is created by a random generation of binary strings. The length of each string is equal to $(1+3n_s)b$, where n_s is the total number of the Lorentzian lines indicated by the given model and b is the number of bits used in the coding of each parameter value. Typically $b = 8$ or $b = 16$.

5. (*Fitness calculation*) The fitness of each solution is calculated as the inverse value of χ^2 computed on the basis of the measured spectrum and the linear combination of Lorentzian functions corresponding to the parameter values extracted from the binary string. The sum and average of all fitness values are computed (eq. 4.1).
6. (*Stopping*) The stopping conditions are tested (e.g., whether a given number of generations has been created or a good solution quality has been achieved without any improvement in the average fitness during the last generations). If the conditions hold, then the iteration stops and the program jumps to step 9.
7. (*Reproduction, cross-in-over and mutation*) Each individual is provided with a selection probability proportional to its share of the total fitness. Individuals are pairwise selected for reproduction by a "roulette wheel" with sector sizes proportional to the selection probabilities. A new population is formed with the help of the operations of cross-in-over and mutation. These operations are performed with probabilities indicated by the parameters cross-in-over and mutation probability, respectively.
8. (*Elitism or clone*) The worst solution in the new population is replaced by the best solution of the previous population.
9. (*Local improvement*) The fitness of the best solution in the population can be improved with the help of a simple "hill-climbing" algorithm [Gol 89].
10. (*Final output*) The program computes the final "physical" parameter values (like δ , Δ and B_{hf}) on the basis of the extracted parameter values corresponding to the best solution. The result is written into an output file.

4.4 Fitting control using fuzzy logic

Fuzzy set theory has been used in applications where the solution is highly dependent on human experience; because of either imprecise information available or the empirical nature of the problem [Mar 94].

A fuzzy system incorporates fuzzy heuristics and knowledge that defines the terms being used in the former level. Indeed, it is possible to encode linguistic rules and heuristics directly reducing the solution time since the used expert's

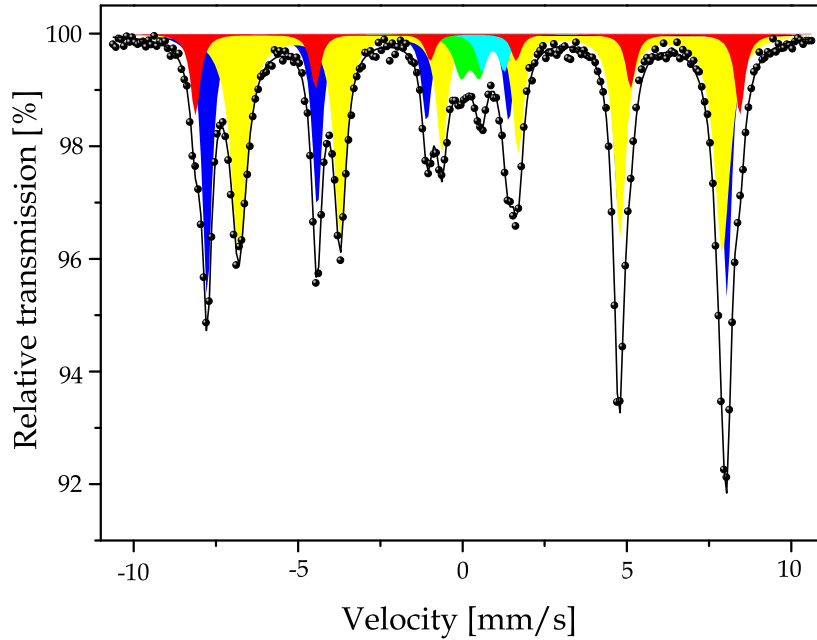


Figure 4.5: A typical Mössbauer spectrum fitted using the genetic algorithm. Three sextets and two doublets were fitted.

knowledge can be built in directly. In addition, its qualitative representation form makes fuzzy interpretations of data very natural and an intuitively plausible way to formulate and solve several problems. The fuzzy system was used to control and accelerate the least-squares fitting of a Mössbauer spectrum [Des 02]. "Good sense" rules can be implemented and can also be updated making this system useful to solve problems of which analytical solution is very difficult or not possible. A typical use of this technique is shown in table 4.1 where the number of fitting steps is decided based on the variation of the Mössbauer parameters of the line width (Γ) and the spectral area. They are based on the (fuzzy) idea that if the line width do not vary much (e.g., small) and the associated spectral area also does not vary their values can be fixed, accelerating the fitting process. The numbers in this table are given as percentage of cycles set of the missing fitting iterations. The number zero means both the line width and the line intensity can be fixed. This makes the fitting process fast. The number 50 means that at half of the iterations to end the fitting a new fuzzy inference will be done. The fuzzy inference ranks both variables as small, medium or large depending on their variation. As discussed, it is based on a general idea and no precise relationship is needed. This kind of decision is usually taken on human experience on the subject. The percentage unit indicated in table 4.1 refers to

the variation of the given parameter (e.g., spectral area or line width) in a given iteration interval.

Table 4.1: Fuzzy rules implemented to set up the number of interactions for each variables that should participate in the fitting process. These rules establish a dynamic stopping condition for these parameters.

	spectral area		
	small	medium	large
	< 5%	< 10%	> 10%
small (< 5%)	0	25	50
↵ medium (< 10%)	25	50	75
large (> 10%)	75	75	100

The fuzzy systems realize, from values of Mössbauer parameters during the fitting process, the updating of the input file to the fitting program at the next iterative step. The relevant variables to the fuzzy implementation were B_{hf} , line width (Γ , in mm/s), relative area of each subspectrum and the difference between the final and initial least-squares fitted values of isomer shift and quadrupole splitting, respectively. Correlation of the evolution of isomer shift and quadrupole splitting were implemented, but without indicating analytically their interdependence, if any exists [Des 99]. To decide if a fitting parameter has converged, the fuzzy logic was used. The fuzzy systems tends to substitute the analyst in taking decisions for the next step(s) of fitting the spectra. These decisions are, for example, the number of iterations to be used and which Mössbauer parameters still to be fitted. The use of fuzzy logic decreases the required time for the fitting process, resulting in a decrease of the obtained quality (fig. 4.6; [Des 99b]).

4.5 Mössbauer-mineral data bank

There are some useful data collections that can be found in the literature for Mössbauer reference data of a given compound. The most extensive compilation is the *Mössbauer Information System* (MIS) of the *Mössbauer Effect Data Center* (MEDC) at the University of North Carolina at Asheville. The MEDC has been collecting Mössbauer data since the discovery of the Mössbauer effect. The MIS contains about 40,000 bibliographic references, and its update entries are regularly published in the *Mössbauer Effect Reference and Data Journal* (MERDJ) [Ste 82]. One MERDJ contains 10 issues

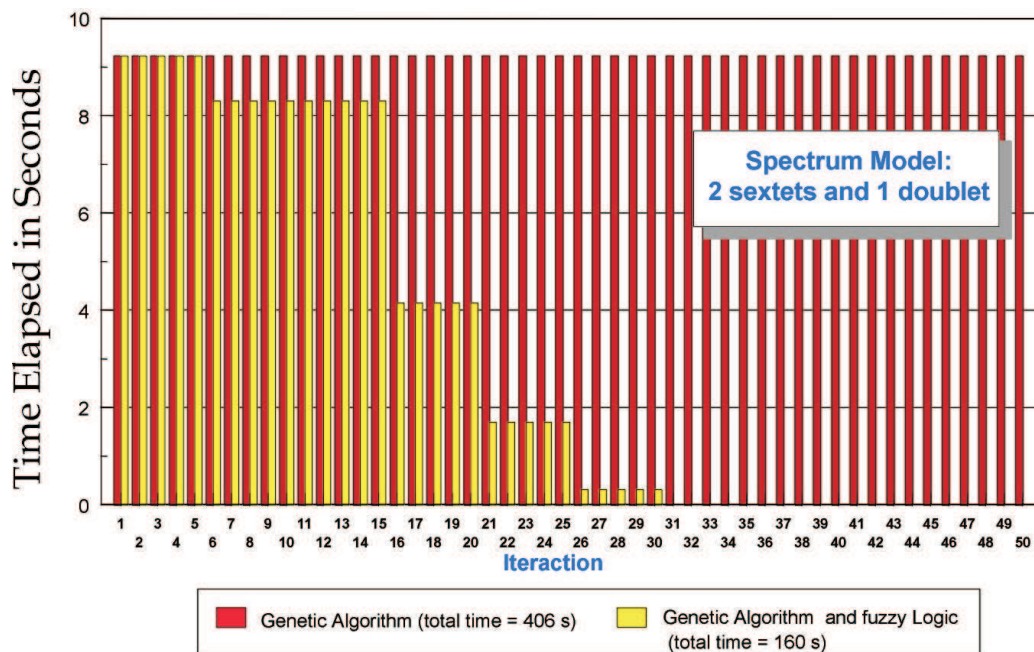


Figure 4.6: Comparison of the fitting with and without the fuzzy control. The fitting stopped after 30 iterations because of fuzzy inference, and after 50 using only genetic algorithm.

and a special index, covering one year of literature search.

A separate data bank of Mössbauer parameters and references of minerals containing iron reported in the literature from 1958 to 2001 has been created.³ This data bank contains information of source and its matrix, temperature of the absorber, isomer shift (δ , in mm/s), quadrupole splitting (Δ , in mm/s), internal magnetic field (B_{hf} , in Tesla), and the references. The stored data cover some 500 minerals and contain around 1,000 printed pages describing the published parameters. The data bank was developed in an user friendly environment. The limitation of the use of these databases is that no relative intensities among the phases are given.

Variation in the Mössbauer parameters may indicate minor differences in mineral phases (e.g., the quadrupole splitting in fayalite ($Fe_2[SiO_4]$), olivine ($(Mg, Fe)_2[SiO_4]$) and forsterite ($Mg_2[SiO_4]$). The dependence of the quadrupole splitting on the forsterite-like content in olivines is presented in figure 4.8. This graph is used to estimate the percentage of forsterite

³Cf. app. A for some of these minerals.

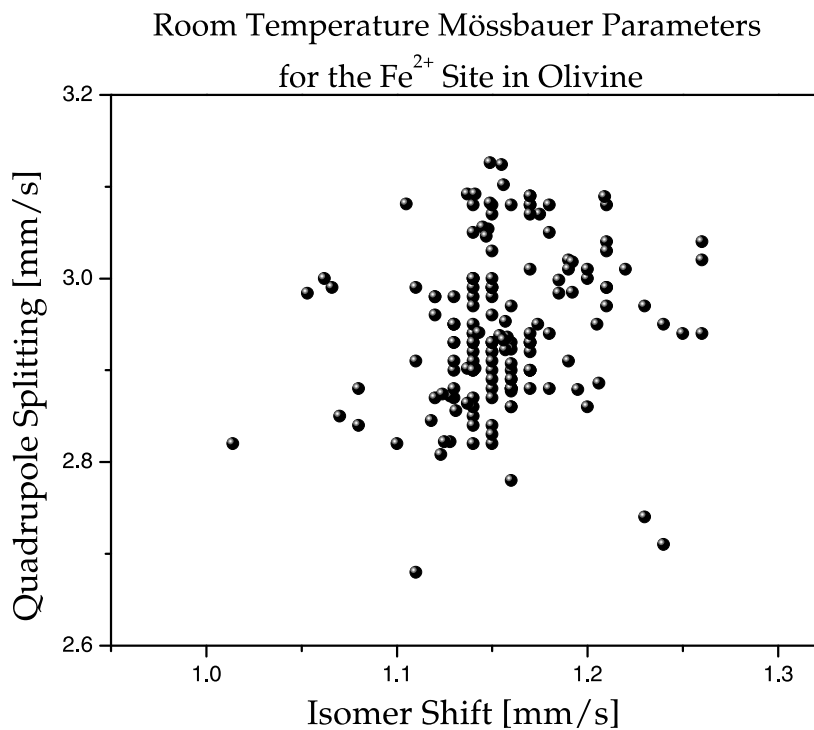


Figure 4.7: The plotting of quadrupole splitting against isomer shift for ferrous sites in olivine minerals. This data suite has been collected from 167 published measurements.

(Fo%) in the olivine found in Martian soils and rocks.⁴

4.6 Mössbauer phase identification

Temperature dependent Mössbauer spectra are being used for the characterization of minerals. Least-squares fitted Mössbauer parameters are primarily used for identification purpose as a unique finger-print signature for most minerals. Some of them, such as the nanophase ferric oxides found on Mars (sec. 6.4), cannot be clearly distinguished by a single Mössbauer measurement. For a unique identification further information is required. This information can be obtained from higher or lower temperature Mössbauer measurements. Additional data can also be collected by applying an external magnetic field to the sample during the Mössbauer measurement or analyzing data from other techniques such as X-ray diffraction, Raman, thermal emission and photoelectron spectroscopies, and others.

⁴Cf. sec. 6.4.2.

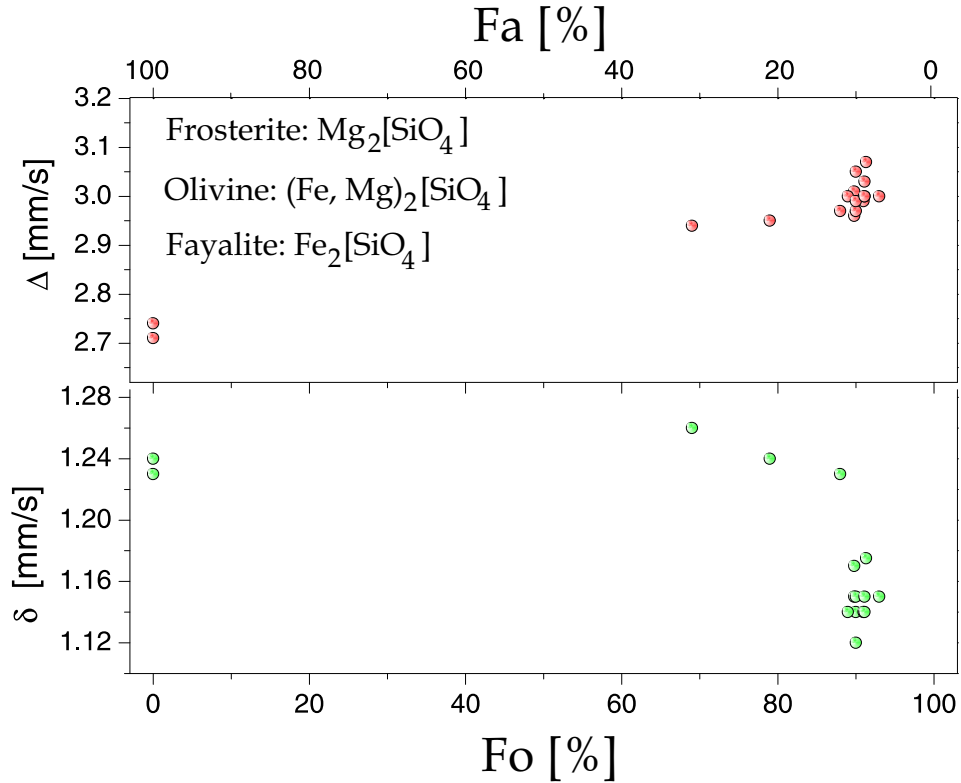


Figure 4.8: Dependence of the Mössbauer parameters of quadrupole splitting (Δ , in mm/s) and isomer shift (δ , in mm/s) against the content of forsterite (Fo, in %) or fayalite (Fa, in %) in olivines. The Mössbauer parameters were obtained at room temperature and published in the literature. Forsterite (iron-free olivine) has no detectable Mössbauer effect.

If only data from Mössbauer measurements are available, apart from chemical analysis and thermal emission spectroscopic data, which is the case for Mars Exploration Rover mission, a unique identification may not be obtained. Fortunately, for this mission, Martian diurnal temperature helps the identification, except for the nanophase ferric compounds found in Gusev Crater.

A comparison of the Mössbauer parameters is still the first approach used for mineral identification. With the corrected the isomer shift for a single standard at a given temperature, literature search for similar parameters is in some cases a reasonable starting point in Mössbauer phase identification. Nevertheless, considering the number of possible minerals, the number of subspectra associated to a single mineral, the interpretation strategy used to analyze the Mössbauer spectrum (e.g., number of lines in the spectrum

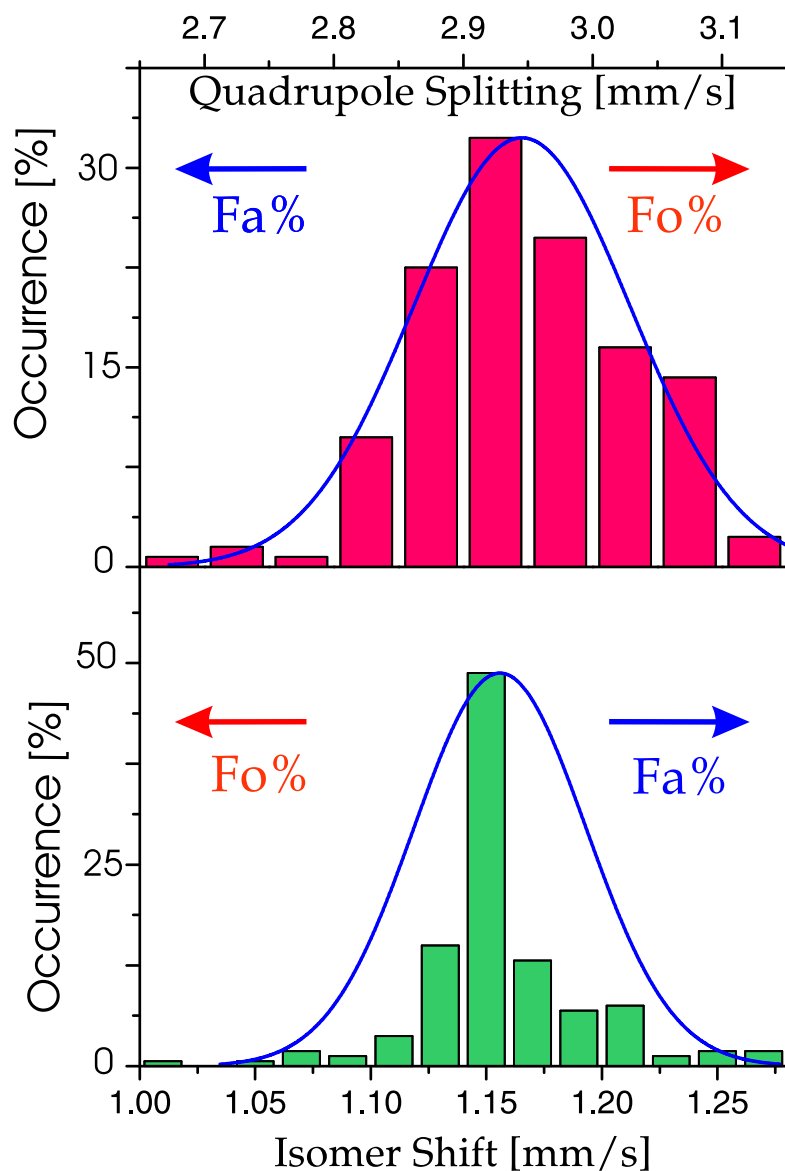


Figure 4.9: The distribution of 167 published Mössbauer parameters for ferrous site in olivine mineral obtained at room temperature. A similar normal distribution can not be obtained for all minerals; because it is dependent on the amount of data available, on the mineral diversity and how extensively and carefully it was reported.

or the use of distribution models for the parameters) the eventual presence of some special effects (e.g., Morin transition, super-paramagnetism), impurities (e.g., Al in goethites), among other odds, the identification can be difficult. In natural systems, the difficulty increase because of isomorphic substitution, crystallinity, partial physical or chemical weathering, grain size

distribution, and the presence of other major phases.

In addition to the Mössbauer data compilation, either in data bases or in private reference collections, artificial intelligence techniques were implemented to assist the identification of mineral phases Mössbauer data.

4.6.1 Neural identifiers

There are two main reasons that exclude the possibility of a wide identification of substances or the identification of some structural properties of these minerals from a Mössbauer set of data:

1. Mössbauer spectroscopy is a precise technique, enabling to find some small differences in interlaboratory measurements of the same sample [Dya 84, Way 86]; and
2. it is possible to find mistakes in the published parameters from spectral misinterpretation or lack of experimental care and precision.

The search for exact information using a conventional data bank is of limited help. Data bank search for exact information is incapable to differentiate the values of Mössbauer parameters within the experimental errors (e.g., $\delta=0.22$ mm/s from $\delta=0.23$ mm/s, but physically or depending on the experimental error, both values may be considered equivalent). Therefore, it is necessary to try a different approach in trying to identify the substance and its properties.

Artificial neural networks (ANN) was used to identify the substance studied and some of its crystalline properties. Artificial neurons learn from experience and data, generalizing previous examples to new ones. Under proper training this computer structure can extract essential characteristics from inputs containing irrelevant data. They have the ability to see through noise and distortion of the data environment. ANN were implemented and trained with the Mössbauer parameters published in the literature and stored in the compiled data bank. After proper training, it is able to identify several substances and their crystalline structures from new values of the Mössbauer parameters.

Interest in ANN has been growing rapidly over the last few years. It is possible to apply computation that make machines learn and remember in ways that bear a striking resemblance to human mental processes. ANN are

composed of elements that perform in a manner that is analogous to the elementary functions of the biological neurons. The elements are organized in a way that may or may not be related to the cerebral anatomy. Artificial neurons learn from experience, generalize from previous examples to new ones, and extract essential characteristics from inputs containing noisy or irrelevant data. ANN can modify their behavior in response to their environment. Given a set of inputs they self-adjust to produce consistent responses. Once the networks are trained, response can be insensitive to minor variations in its inputs. The ability to see through noise and distortion lies within is vital for pattern recognition in a real world environment. ANN have the ability to extract an ideal answer from imperfect inputs (like published wrong Mössbauer parameters). There have been some very impressive demonstrations of artificial neural network capabilities [San 92] using implementations either on software or on hardware that provide an alternative way for solving problems so far intractable. Neural computing, new developments, theory and practice have been reported (e.g., [Des 02] and references therein).

ANN have also been extensively used in different types of problems that need grouping or data mapping and mining (e.g., [San 92]). ANN derive its computing power through, first, their massively parallel distributed structure and, second, their ability to learn and therefore generalize; generalization refers to the ANN producing reasonable output for inputs not presented during training (learning). These two information-processing capabilities make possible for ANN to solve complex and large-scale problems that were currently intractable [Sim 96].

The use of ANN in Mössbauer analysis of corrosion products from Mössbauer spectra [Sou 93] and in identification of a substance from Mössbauer parameters of iron-bearing minerals has shown success [Des 98, Des 99]. Identification of non-magnetic phases [Sal 94], magnetic phases [Des 99] and possible martian iron-bearing minerals [Des 03a] have been reported. The interpretation of Mössbauer spectra in the energy and time domain was also proposed using ANN [Pau 00].

The present study involves the training of ANN with Mössbauer parameters of isomer shift, quadrupole splitting and hyperfine magnetic field from the literature. After adequate training it could successfully identify, from experimental Mössbauer data, the iron-bearing minerals and, for some of them, the crystalline structure of the studied sample.

4.6.2 The implemented neural network

A sub-set of the available data bank is used to train the artificial neurons and the rest of the data is used as a validation set to check and correct the training. Once the neural net is trained and validated, new data can be presented for identification.

Basically, the artificial neurons are represented as vectors imposed to change its coordinates according to a specific rule. The main goal of the ANN is to perform a vector copy (i.e., representation) of the data.

For the identification of minerals a hybrid learning was chosen [Hec 87] (supervised and unsupervised learning) and applied to a *learning vector quantization* (LVQ) network consisting of a self-organizing map [Koh 88]. The number of neurons at the LVQ is ideally three times more than in the input layer. Figure 4.10 depicts the architecture of the applied ANN and the function and data handling at each layer of neurons. The training phase consists of a vectorial copy the available data.

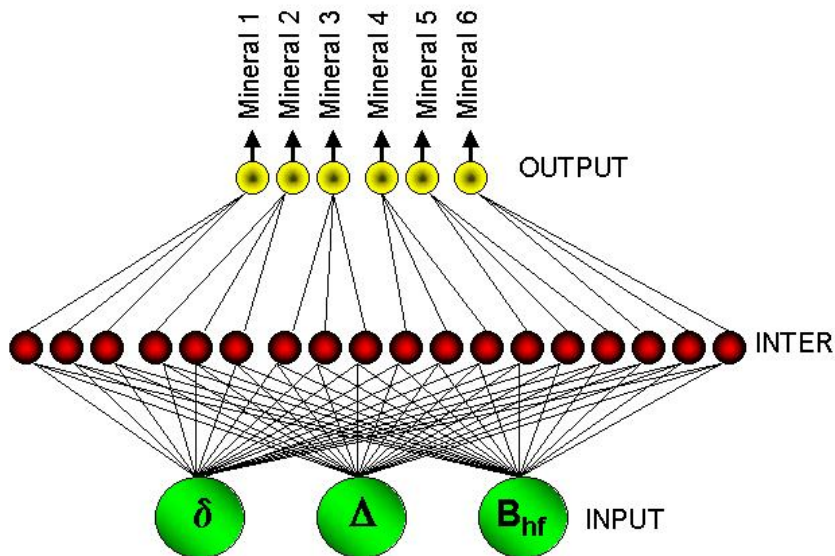


Figure 4.10: Architecture of the ANN used for the mineral identification based on the Mössbauer parameters of isomer shift, quadrupole splitting and hyperfine magnetic field.

The learning process in the LVQ network is implemented in two steps. The first one is a primary self-organizing map of neurons at the input setup space that is made by a classical Kohonen's layer in which an algorithm consists of the following phases (the index k refers to Kohonen's layer):

1. Initial weight vector \vec{W}_k (neurons) are defined by choosing small and random numerical values.
2. While the stopping condition does not occur, do steps 3-9.
3. For each input vector \vec{X}_i (input data, e.i., the Mössbauer parameters), do steps 4-6.
4. Find the input vector, obtain the distance between \vec{X}_i and the weight vectors \vec{W}_k .
5. For the input vector \vec{X}_i such that its distance from the weight vectors \vec{W}_k is minimum.
6. For all neurons within the specific neighborhood of the input vector as chosen in step 5, compute update of the weights, as follows:

$$\vec{W}_k^{new} = \vec{W}_k^{old} + \alpha(t)[\vec{X}_i - \vec{W}_k^{old}] \quad (4.4)$$

where $\alpha(t)$ is the learning rate, which is a slow decreasing function of time (or training epoch).

7. Update the learning rate $\alpha(t)$ by the following equation:

$$\alpha(t) = \alpha(0) \left(1 - \frac{t}{T}\right) \quad (4.5)$$

where $\alpha(0)$ is the initial learning rate, t is the actual epoch, and T is the number of iterations (stopping condition).

8. Reduce the reach of the topological neighborhood at specified times.
9. Verify the stopping condition.

The topological neighborhood may be chosen as a circle or other surface where the neurons inside this region are made to learn, and the neurons from outside keep their positions (weight vector coordinates). Before the use of the LVQ algorithm, it is necessary to distribute the LVQ neurons among the input vectors. Each specific group of neurons (typically three) will be responsible for each input. LVQ is a supervised learning technique that

uses class information to improve the quality of the classified decision region providing a fine-tuning adjustment at the self-organized map. After the use of Kohonen's learning algorithm, one turns to apply the LVQ algorithm to improve the mapping quality. In the LVQ algorithm, an input vector \vec{X}_i is picked at random from input space. If the class labels of the input vector \vec{X}_i and of the a weight vector of the LVQ layer (\vec{W}_L) agree, the vector \vec{W}_L is moved in the direction of the input vector \vec{X}_i . If the class labels of the input vector \vec{X}_i and the vectors \vec{W}_L disagree, the weight vector (\vec{W}_L) is moved away from the input vector \vec{X}_i . The LVQ algorithm proceeds as follows:

1. Suppose \vec{W}_L is the closest vector to the input vector \vec{X}_i . The weight vector \vec{W}_L is updated as follows:
2. If the desired class or the mineral name ($\mathcal{C}_{\vec{X}_i}$) of the input vector agree with the class of the weight vector ($\mathcal{C}_{\vec{W}_L}$), then

$$\vec{W}_L^{new} = \vec{W}_L^{old} + \alpha_L(t)[\vec{X}_i - \vec{W}_L^{old}] \quad (4.6)$$

where $\alpha_L(t)$ is the learning rate of LVQ assuming a small initial value, typically $\alpha_L(0) = 0.06$.

3. If $\mathcal{C}_{\vec{X}_i} \neq \mathcal{C}_{\vec{W}_L}$, then

$$\vec{W}_L^{new} = \vec{W}_L^{old} - \alpha_L(t)[\vec{X}_i - \vec{W}_L^{old}] \quad (4.7)$$

4. The other weight vectors \vec{W}_L are not modified.
5. Update the learning rate $\alpha_L(t)$.
6. Verify the stopping condition.

After several passes through the input data, the weight vectors might converge, and the training is completed.

The neural nets were trained to identify minerals from Mössbauer parameters of δ , Δ , and B_{hf} and crystalline structures from δ , Δ , and for some cases, the polyhedral volume of a coordination site V_p . Details on both training are given in the next two sections.

4.6.3 Neural identification of minerals

The implemented ANN for identification of substances (143 minerals studied by Mössbauer spectroscopy listed in app. A) from Mössbauer parameters has 429 units at the Kohonen's layer, three times the mineral phases to be identified. The fine-tuning of the first mapping is done by a LVQ network (supervised and competitive learning) using the same number of neurons to identify all minerals in the data set. The source program was written in C++ language.

The information used to train the ANN comes from the compiled data bank containing Mössbauer parameters of 143 substances from the literature recorded at room and liquid nitrogen temperatures.⁵ To use the ANN, the program restores the experimental Mössbauer parameters of δ , Δ , and B_{hf} obtained by the fitting program. The ANN output will give the identification of the corresponding substance, or up to three other options from which to choose. The options are given to eliminate possible errors in the ANN identification and let the operator choose from other available physical or chemical data or by the researcher's experience. Occasionally, the ANN gives the same name to three options. Once the ANN classifies the substance, the user may start the data bank mode to obtain the references of these substances that were published. Table 4.2 presents the summary of the result of 200 tests of the neural identification of iron-bearing minerals. An example of a neural error in the first option of the mineral identification is given by melanterite ($FeSO_4/7H_2O$, e.g., $\delta = 1.26$ mm/s; $\Delta = 3.21$ mm/s) and rozenite ($FeSO_4/4H_2O$, e.g., $\delta = 1.32$ mm/s and $\Delta = 3.17$ mm/s).⁶ The second option was corrected in 12 % of the tests, and in eight tests (4 %) it was equal to the first option. The third option was only correct when the previous two options were identical. The fourth option was correct only when all three previous options were incorrect.

The user can either obtain the Mössbauer parameter of a given substance or search the substance that holds the Mössbauer parameters in a given value range. In the database, literature references on published minerals are also compiled. New minerals cannot be uniquely identified using the present data base and the neural networks.

⁵Possible Mars minerals at this data bank are listed in app. A.

⁶Melanterite reported by Borek (S. L. Borek, ACS Symp. Ser. 550,1(1944)31); and rozenite by Montano (P. A. Montano, Characterization of iron-bearing minerals in coal. In *Advances in Chemistry Series* (1981)337).

Table 4.2: Summary of results obtained in 200 tests for the neural identification of minerals. Agreement means identification match with the literature.

Option	agreement rate	accumulated agreement
1 st	88 %	88
2 nd	12 %	97
3 rd	3 %	99
4 th	1 %	100

4.6.4 Neural identification of crystalline structures

Since the late sixties several correlations between Mössbauer parameters and structural properties were applied. A correlation between δ and Δ for a series of monosubstituted ferrocyanides was attempted by Grand [Bra 65]. Brady et al. [Bra 65] observed that the data then available showed no general correlation between δ and Δ in high-spin ferrous compounds. For anhydrous ferrous halides [Axt 68], ferrous chloride hydrates [Haz 68], and ferrous iodide hydrates [Axt 67], approximately linear relationships have been reported. The Δ data employed in the correlation were limited to compounds in the paramagnetic phase at temperatures sufficiently low such that the splitting attained a constant value. All the contained octahedrally coordinated Fe^{2+} sites, and the observed correlation indicated minimal contributions to the Δ in these compounds from the lattice spin orbit coupling [Haz 68]. Jorgensen [Jor 69] proposed that a linear correlation derives from a similar effect on both δ and Δ that are produced by differences in the central field covalency. Burger [Bur 72] and Bancroft and Platt [Ban 72] tried to correlate partial values of δ and Δ .

Burns [Bur 94] tried to relate different crystalline structures graphically using Mössbauer parameters of δ and Δ and correlating these parameters with various bond length-related parameters as mean metal-oxygen distance of a coordination site, and the volume per oxygen in a unit cell and polyhedral volume. But this method has had limited success in several cases to delimit δ ranges for Fe^{2+} and Fe^{3+} ions in silicates with tetrahedral, octahedral and five-fold coordination sites. For this purpose Burns reported [Bur 94] these parameters in pairs making it in two dimensional graphics. In some cases (e.g., orthopyroxenes $\delta = 1.12$ mm/s and $\Delta = 1.90$ mm/s, octahedral; and pigeonite $\delta = 1.12$ mm/s and $\Delta = 1.90$ mm/s, 6-7 coordination; both Martian candidates) there is superposition of clusters that make it impossible to determine precisely their crystalline structures using only δ and Δ .

For a correct identification it was necessary to make various two dimensional graphics. The same implemented ANN for mineral identification, with less units, was used for crystalline structure identification from the Mössbauer parameters. The program performed the identification of different degrees of distortion in octahedral crystalline structure of silicates with Fe^{2+} valences, the identification of different crystalline structures with the δ and Δ of silicates with Fe^{2+} valences, and the identification of different crystalline structures with δ and Δ and polyhedral volume of a coordination site (V_P) to silicates with Fe^{3+} valences. The values of V_P used here are as reported by Burns [Bur 90, Bur 93]. A summary of results is given in table 4.3.

Different degrees of distortion in octahedral crystalline structures of iron-bearing silicates were identified using ANN (table 4.3(a)). It was also possible to identify correctly the structure when the iron contained in the minerals was present as a minor constituent, particularly Mg- and Al-silicate phases containing low concentration of Fe^{2+} and Fe^{3+} substituting for Mg^{2+} and Al^{3+} ions in octahedral, tetrahedral, and five-fold coordination environments. Therefore, the Mössbauer parameters alone are not sufficient to distinguish these crystal structures. More information should be used, complementing the Mössbauer parameters, to distinguish those structures. Table 4.3(b) resumes the results obtained with the neural identification of different crystal structures from the Mössbauer parameters of δ and Δ .

The problem of classifying different structures, when the iron is a minor constituent, could be solved by introducing a third axis with the new parameter of polyhedral volume of a coordination site [Bur 93]. To perform this complimentary test, the architecture of the neural network was altered including a new neural dimension producing the following input data vector \vec{X}_i :

$$\vec{X}_i = (\vec{X}_1, \vec{X}_2, \vec{X}_3) = (\delta, \Delta, V_P) \quad (4.8)$$

Table 4.3(c) shows the neural identification of different crystalline structures using the polyhedral volume of a coordination site in addition to the Mössbauer parameters.

4.7 Summary

The analysis of a Mössbauer spectrum is a time-consuming task, requires excessive human effort, and depends on the specialist's experience. The use of genetic algorithm and fuzzy logic was proposed to obtain the Mössbauer parameters. An ANN, trained with published Mössbauer data from the data

Table 4.3: Identification of (a) different degrees of distortion in octahedral crystalline structure of silicates with Fe^{2+} valences, (b) different crystalline structures of silicates with Fe^{2+} and Fe^{3+} valences, and (c) crystalline structures where iron is a minor element and the polyhedral volume of a coordination site in addition to the Mössbauer parameters.

	δ [mm/s]	Δ [mm/s]	V_P [Å ³]	Mineral	Crystalline Structure
(a)	1.56	2.62		biotite	octahedral
	1.38	2.44		diopside	octahedral
	1.17	2.43		pigeonite	octahedral
	1.16	2.93		olivine	octahedral distorted
	1.12	2.02		orthopyroxene	octahedral very distorted
(b)	0.33	0.56		vesuvianite	5-CN
	0.21	0.48		sanidine	tetrahedral
	0.37	0.86		muscovite	octahedral
	1.12	1.96		pigeonite	6-7 CN
	1.12	1.90		orthopyroxene	octahedral
(c)	0.33	0.85	10.78	Fe-saphirine	octahedral
	0.29	1.23	11.63	Mg-saphirine	octahedral
	0.29	1.23	2.78	Mg-saphirine	tetrahedral
	0.36	1.00	9.82	yoderite	octahedral
	0.36	1.00	2.78	yoderite	5-CN

bank was capable to identify, from new experimental Mössbauer parameters (δ , Δ , and B_{hf}), the substance under study and its crystalline structure. The applied automation tools are described in a block diagram in figure 4.11.

The developed miniaturized Mössbauer spectrometer (MIMOS II) opens up many extraterrestrial and terrestrial applications. Non-destructive analysis of large samples can be aimed, in field, with this portable outdoor Mössbauer spectrometer. Both systems (data analysis and equipment) represent an interesting tool for the application of the Mössbauer technique in field and for non-specialists.

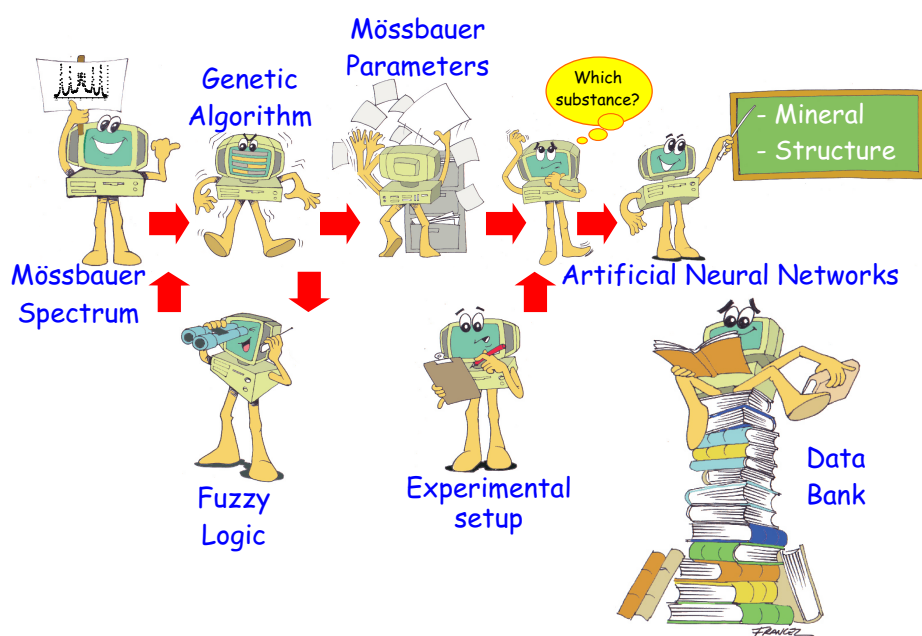


Figure 4.11: Automation in Mössbauer fitting and identification processes.

Chapter 5

Selected terrestrial outdoor applications

5.1 Introduction

Mössbauer spectroscopy is highly suited for the study of iron-bearing compounds present in environmental samples. Natural solid materials, such as rocks, soils, sediments and suspended particles (in air or in water deposits) typically contain iron in a suitable concentration for a Mössbauer study. Magnetic properties, valence state and crystalline arrangement can further be assessed using this technique. Outdoor experiments were performed with MIMOS II demonstrating applications of portable Mössbauer spectroscopy. Thanks to MIMOS II portability, robustness, low-power consumption and relative easy radiation shielding, in situ characterization became possible. These advantages of MIMOS II were explored in some outdoor applications such as in air pollution monitoring. Non-destructive analysis on ancient archaeological artifacts is also presented. Since the historical artifacts were relatively small in size, these specimens were brought to the laboratory. These samples could also be analyzed in field. An additional motivation for this study is the fact that the environmental application of space technology is also the ultimate effort expected from the space payload development endeavor.

5.2 Air pollution investigation

Long-term monitoring network have been used to detect visibility degradation in urban, industrial, and remote environments, to evaluate air quality trends with respect to emission changes, and to assess the effectiveness of air pollution control measures. A sampling system that serves one objective

does not necessarily meet other research needs. This is especially true for filter-based samplers designed to determine compliance with mass-based air quality standards, which might have limited applicability for chemical speciation. But this filter-based system, usually iron-free, should work fine for sampling airborne particles, and therefore, for Mössbauer characterization. Airborne particle sampling intend to determine compliance with air quality standards, helping also to examine the extent and causes of elevated concentrations, to apportion constituents of particulate matter to pollution sources, and to evaluate adverse health effects, among other reasons (e.g, [Cho 95]).

Special attention must be paid to the requirements for airborne aerosol sampling systems. These requirements include appropriate choice of size-selective inlets, select proper filters for sampling and their holders. In this study the size-selective inlets allows sampling of high-volume of air, collecting particles with aerodynamic diameters less than 100 μm . These particles are known as "total suspended particles" (TSP). An aluminum holder for silica or paper-based filters was selected.

The identification of air pollution sources is one of the main goals of any monitoring of the air quality in an industrial and urban region. Investment priorities to reduce the impact of these sources can only be determined with a good source assessment. The faster the pollution is monitored, the better will be the utility of the polluter source assessment. Most of the monitored urban areas in the world are recording only the dust concentration in the air. Some of them using on-line samplers (e.g., [Wat 01]). The characterization itself is performed in the laboratory. Since fine powdered dust may react with humidity and gases (e.g., O_3 , SO_x) late characterization could render the source identification and assessment difficult. In this situation, the control of an eventual problematic source will not be efficient. Nowadays, a better control presumes on-line and in situ monitoring.

Mössbauer spectroscopy is reported as a useful technique in the identification of iron-bearing phases present in airborne particles (e.g., [Web 00]). The identification of iron-bearing materials in the airborne particles in atmospheric aerosols in the metropolitan region of Vitória (MRV), Espírito Santo, Brazil, were performed using MIMOS II. The MRV covers an area of 1461 km^2 , consisting of the cities of Vitória, Vila Velha, Cariacica, Viana, and Serra. This region has nearly 1.3 million inhabitants, houses a large industrial complex, is undergoing an expansion and has to bear an intense traffic. During the second half of the eighties particulate matter (TSP) concentration above $80 \frac{\mu\text{g}}{\text{m}^3}$ was recorded. These concentrations did not comply with

the Brazilian air quality standards. High pollution concentration also were associated with a period of low pluviometric precipitation, strong winds, vegetation burnings and intense industrial activities.

MIMOS II was used in field, installed inside an airborne particle sampler. The necessary power was supplied by a 45 W battery. The instrument was installed with a mechanical isolation to avoid vibrations which would bring noise to the miniaturized Mössbauer drive. Additional shielding for the Mössbauer source was installed in the sampler. MIMOS II stably operated in field and the obtained results are in good agreement with the results recorded in the laboratory. Two sampling points were selected: Ilha do Boi in Vitória city (fig. 5.1) and Bela Aurora in Cariacica. The sampling points were chosen considering the predominant wind direction (Ilha do Boi, where wind blows from the industrial to the urban area) and where high concentration of particulate matter have been recorded (Bela Aurora).



Figure 5.1: Air pollution samplers located at Ilha do Boi, Vitória, Brazil.

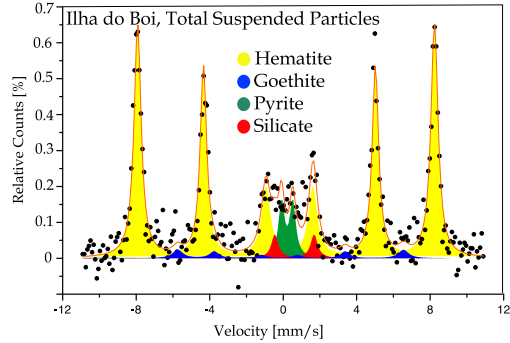


Figure 5.2: A Mössbauer spectrum obtained at Ilha do Boi.

Table 5.1: Airborne particles collected at Ilha do Boi and at Bela Aurora and in field analyzed with the MIMOS II.

Site	Phase	δ [mm/s]	Δ [mm/s]	B_{hf} [T]	Area [%]	Possible Source
Ilha do Boi	hematite	0.37	-0.21	51.7	89	industrial
	goethite	0.37	0.01	37.1	2	soil
	pyrite	0.30	0.50		2	coal
	Fe^{2+}	0.37	0.21		4	soil
Bela Aurora	Fe^{3+} phase	0.36	0.62		51	industrial
	hematite	0.37	-0.21	51.7	49	soil

The Mössbauer spectra obtained in Bela Aurora (fig. 5.3) contain a doublet (Fe^{3+}) and a hematite sextet. The Mössbauer measurement done in Bela Aurora were recorded simultaneously in both backscattering and transmission geometries. The calculated ratio of both phases in the Mössbauer spectra are similar in backscattering or transmission geometries. The outer lines of the sextet in transmission geometry seems to be shifted to the center, although the spectral statistics may cause this deviation in the fitting. This shift causes a little change in the quadrupole splitting and in the internal magnetic field, which is again, resulting from poor statistics for this minor phase. Another possible source for this distortion in the Mössbauer spectrum recorded in backscattering geometry can be the cosine-smearing effect. Despite this deviations, the sextet can be associated to hematite.

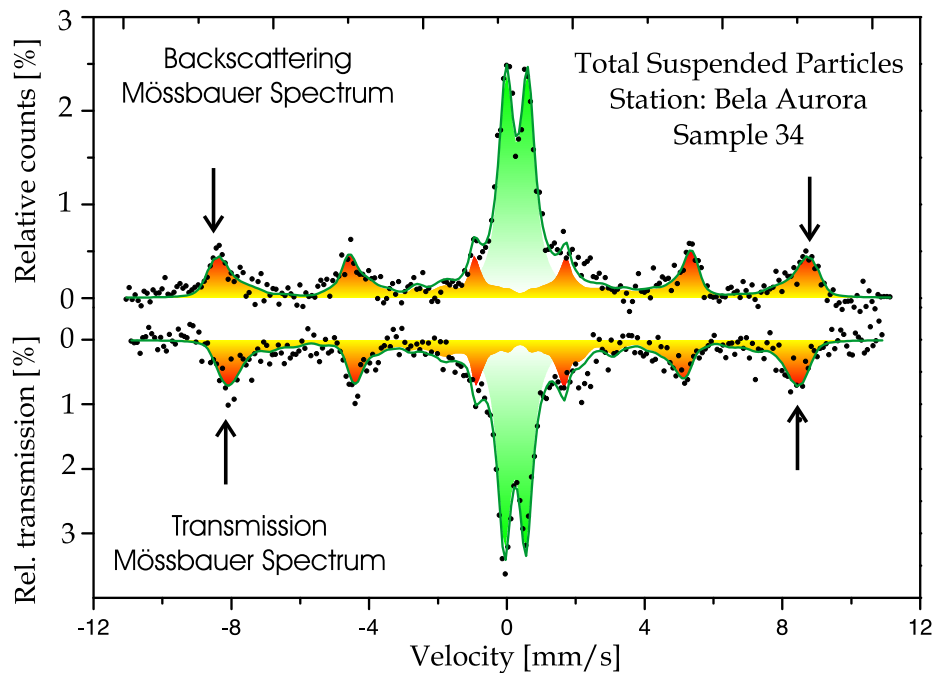


Figure 5.3: Simultaneous transmission and backscattering MIMOS II field measurement of aerosol particles collected at *Bela Aurora* air quality station, Cariacica, ES, Brazil ([Kli 02]). The shift of the external lines of the sextet in backscattering geometry may be resulting from cosine-smearing effect.

Mössbauer measurements at liquid nitrogen temperature taken on collected dust from Bela Aurora shows no Morin transition, similar to results also obtained from the soil collected in the surroundings. Therefore, this hematite can be associated with soil. The intense doublet is typical of indus-

trial emissions, collected from a local steel industry. Bela Aurora is located approximately 15 km away from the main complex center of MRV and houses an active steel-mill industry.

Hematite was identified as a predominant phase in the suspended particles from Vitória metropolitan region, Brazil. As subordinate phases goethite, pyrite, iron-containing silicates and, sometimes, an ultra-fine Fe^{3+} phase were detected. The hematite comes mostly from the industrial plants producing iron ore pellets (there are seven in VMR) and from soil, goethite from soil and pyrite from handling and storing coal in the industrial area. Ultra-fine particles are a result of strongly weathered tropical soils and industrial emissions. Eventually magnetite was also found. Magnetite is related to steelwork plants and silicates stem from soil and civil constructions.

The in situ analysis has the advantages that no sample preparation is necessary, the instrument can be installed in several places (e.g., in a chimney or in a different particle size sampler). On the other hand, the main disadvantage of the system is that it can not give quick results, e.g., every minute. Also, the required time for each measurement has to be estimated for each place and atmospheric condition. This deficiency can be mitigated with calibrations taking into consideration on-line monitoring of dust concentration.

5.3 Historical artifacts analysis

Many historical artifacts are unique pieces. From these specimens some information about ancient civilizations can be obtained. A proper characterization of these artifacts can reveal historical background on their manufacture process, use, or to which possible post-use treatment it was submitted. Being unique pieces, the best alternative for its characterization is to use non-destructive methods. Considering that iron-bearing minerals are important constituents of these artifacts, Mössbauer spectroscopy becomes an important technique for the analysis of ancient specimens. Some of these pieces are too large for most of conversion electron detectors of Mössbauer spectrometers. Therefore, MIMOS II has become an interesting instrument for the non-destructive analysis of such samples.

As described in detail, MIMOS II is a portable equipment. Klingelhöfer et al. [Kli 02b] reported an interesting application of MIMOS II in the field analysis of rock paintings in Brazil. Some other pieces were analyzed in the laboratory and the results are presented in the following sections.

MIMOS II was used to characterize corrosion products in iron-based archeological specimens, Chinese wall-painting from tombs, pigments in a

Greek vase, and an European illustration (miniature) dated to be of the fifteenth century and made on parchment.¹ These results are presented and discussed in this chapter.

5.3.1 Iron purity and corrosion

Most of iron pieces from centuries ago are completely corroded. Despite this fact, the corrosion products bring some information on the original piece and also on their conservation conditions. Moreover, the motivation of the present Mössbauer characterization is to determine how pure the pieces were centuries ago. For such a purpose, some additional techniques are also used for supplementary information, could the sample be consumed for study.

Carriage hub from "Hallstattzeit"

An iron carriage hub mounting ("Wagennabenbeschlag") originating from a tomb in Offenbach-Rumpenheim, Hessen, were excavated in 1973 [Ulr 73]. This tomb dates to the first half of the sixth century B.C.. The hubs made of ash wood were completely covered by iron sheet metal. This cover was made to give a special gleam to the carriage. Four-wheeled carriages represented an important status symbol during the "Hallstattzeit" (800 - 475 B.C.) and followed outstanding contemporaries into the grave. Four samples from the carriage were characterized.

The first Mössbauer measurement taken at room temperature in the powdered corrosion product resulted in a doublet associated with small particle size Fe^{3+} oxide or oxide-hydroxide (fig. 5.5).

A decrease in the hyperfine magnetic field usually results from isomorphic substitution of Fe by Al, Si or other elements (e.g., [Cor 03]). Considering the hypothesis that all substitution was caused by Al, it will be possible to quantify the maximum concentration of Al in goethites. For this purpose, artificially synthesized Al-goethite reference samples were used. All the reference samples and the powder material extracted from the rusted artifacts were characterized by ^{57}Fe Mössbauer spectroscopy at 4.2 K and by X-ray diffraction and superconducting quantum interference device (SQUID). The hyperfine magnetic field obtained at liquid nitrogen and helium temperatures are smaller than the expected value for pure and well crystallized goethite.

¹Dating information privately communicated by Dr. Claus Maywald- Pitellos from the Gutenberg Museum in Mainz.

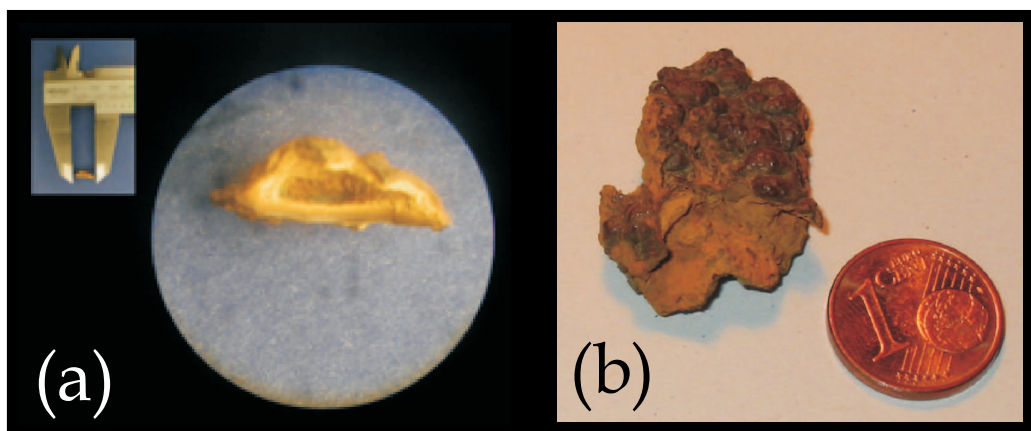


Figure 5.4: A corroded sample from the carriage tomb of Offenbach-Rumpenheim in Hessen (car C sample). (a) Shows a sample with the goethite removed in its normal size and 10 times enlarged, and (b) shows the sample from another artifact surface (car D sample) before the goethite removal.

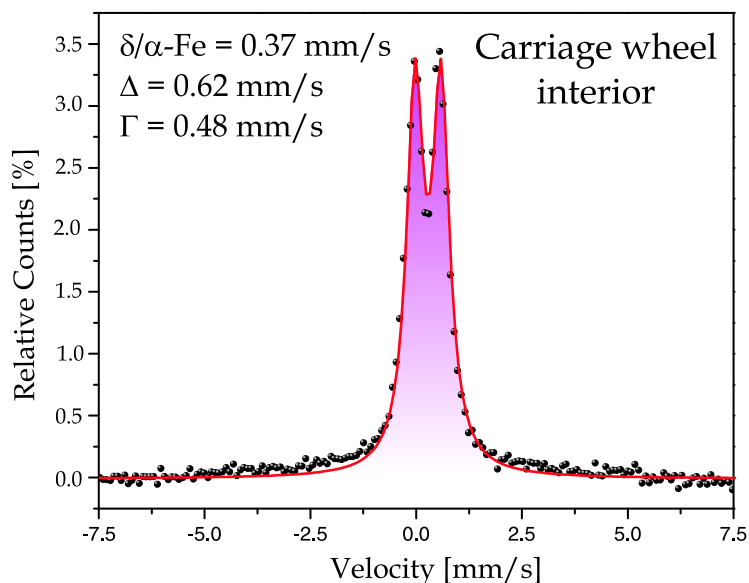


Figure 5.5: Room temperature Mössbauer spectrum of the carriage wheel interior which was in contact with wood (sample car A). The Mössbauer doublet is typical of superparamagnetic Fe^{3+} oxide or oxide-hydroxide.

Reference samples of Al-substituted goethite.

Six Al-goethite reference samples (containing 0; 1.6; 3.5; 6.6; 7.7 and 10.5 mol% Al), ² kindly provided by Prof. Dr. Dr. h.c. Udo Schwertmann were

²10 mol % substitution is equivalent to 0.1 mol mol^{-1} .

Table 5.2: Mössbauer parameters as function of temperature obtained from the rust scratched from the hub (car B sample). All B_{hf} values are obtained from the distribution of this parameter, but for the measurement at 4.2 K. Therefore, their values are not indicated.

Temp. [K]	δ [†] [mm/s]	Δ [mm/s]	Γ [mm/s]	$\langle B_{hf} \rangle$ [T]	Area [%]
293	0.37	0.56	0.44		56.6
	0.32	-0.21		Complex	43.4
220	0.44	0.64	0.34		56.6
	0.37	-0.22		Complex	
200	0.44	0.66	0.64		10.1
	0.44	-0.24		Complex	89.9
190	0.45	0.65	0.63		8.7
	0.45	-0.24		Complex	91.3
160	0.46	0.64	0.57		6.8
	0.46	-0.24		Complex	93.2
131	0.46	0.63	0.57		6.3
	0.47	-0.22		Complex	93.7
100	0.48	0.62	0.55		5.3
	0.48	-0.24		Complex	94.7
86	0.48	0.61	0.61		5.0
	0.48	-0.24		Complex	95.0
78	0.47	0.59	0.63		4.5
	0.49	-0.24		Complex	95.5
60	0.49	0.66	0.72		4.0
	0.49	-0.23		Complex	96.0
4.2	0.25	-0.25	0.40	50.3	100

Note: [†] related to $\alpha\text{-Fe}$; δ , and Δ errors = 0.02 mm/s.

Complex means distribution of the hyperfine field.

synthesized with precipitated solutions of $Fe(NO_3)_3$ and $Al(NO_3)_3$ using KOH and keeping in 0.3 M KOH at 70 °C for two week [Sch 91].

X-Ray Diffraction

A SIEMES D5500 diffractometer equipped with Cu tube, scanning in 2θ from 20° to 80°, was used to determine the crystalline structure of the goethite samples (fig. 5.6). The diffractogram peaks were fitted according to the JCPDF library and the network parameters calculated with the Unit Cell program [Hol 97]. Since goethite has a rhombohedral structure, the program

requires at least five reflections for the calculation of the network parameters and for the unit cell volume (table 5.4). For this work, nine reflections were used (table 5.3). A linear dependence of the unit cell edge length 'c' on the concentration of Al in goethite could be observed (fig. 5.8).

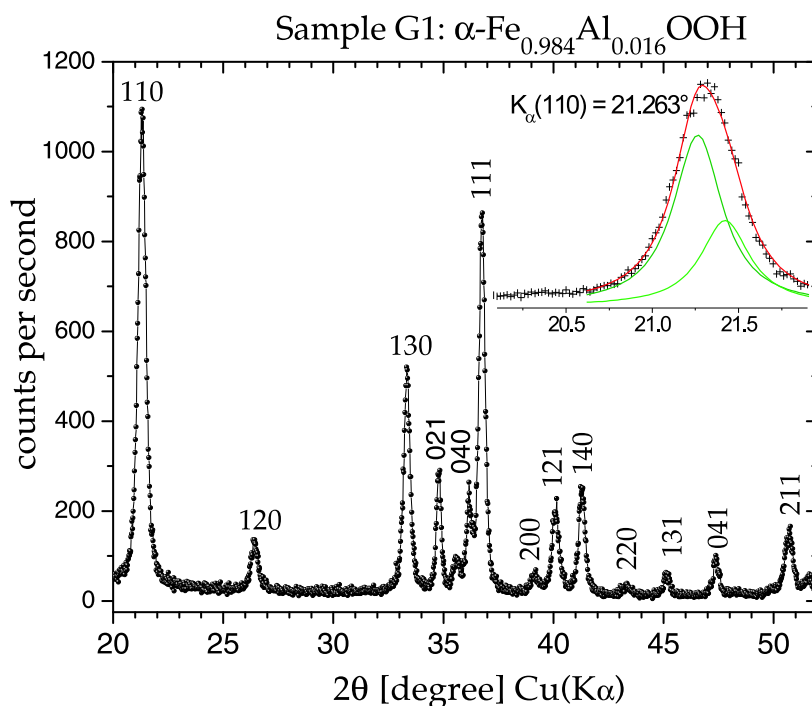


Figure 5.6: X-ray diffractogram obtained from the sample G1 (1.6 mol% Al in goethite) and a single peak detail (1 1 0) fitted using two Lorentzian curves. The Lorentzian curves are constrained to the first line being twice higher and to the same width as the second. The most most intense Lorentzian line position (K_{α}) is used to calculate unit cell edge lengths. For the diffraction plans indication the standard file PDF#290731 was used.

Table 5.3: The nine reflections calculated for the Al-goethite from the X-ray diffractograms.

Sample	Reflection positions, 2θ in degrees								
	1 1 0	1 2 0	1 3 0	0 2 1	1 1 1	1 2 1	1 4 0	0 4 1	2 1 1
G0	21.227	26.349	33.261	34.731	36.672	40.020	41.217	47.317	50.610
G1	21.263	26.389	33.316	34.766	36.721	40.055	41.259	47.349	50.646
G3	21.223	26.359	33.323	34.817	36.713	40.089	41.315	47.349	50.675
G7	21.268	26.461	33.359	34.817	36.786	40.127	41.330	47.443	50.737
G10	21.242	26.384	33.321	34.866	36.776	40.102	41.369	47.512	50.745
G15	21.274	26.481	33.424	34.922	36.855	40.208	41.431	47.632	50.785

Table 5.4: Unit cell parameters calculated from the reflections (table 5.3) obtained from the Lorentzian fitting (fig. 5.6).

Sample	a [nm]	b [nm]	c [nm]	V_{cell} [nm ³]
G0	0.4610(2)	0.9945(4)	0.3019(1)	0.1384(7)
G1	0.4604(1)	0.9934(2)	0.3018(2)	0.1380(3)
G3	0.4611(3)	0.9916(5)	0.3013(2)	0.1377(9)
G7	0.4598(2)	0.9917(3)	0.3012(1)	0.1373(5)
G10	0.4607(3)	0.9910(5)	0.3008(2)	0.1373(8)
G15	0.4602(2)	0.9882(4)	0.3003(1)	0.1366(6)

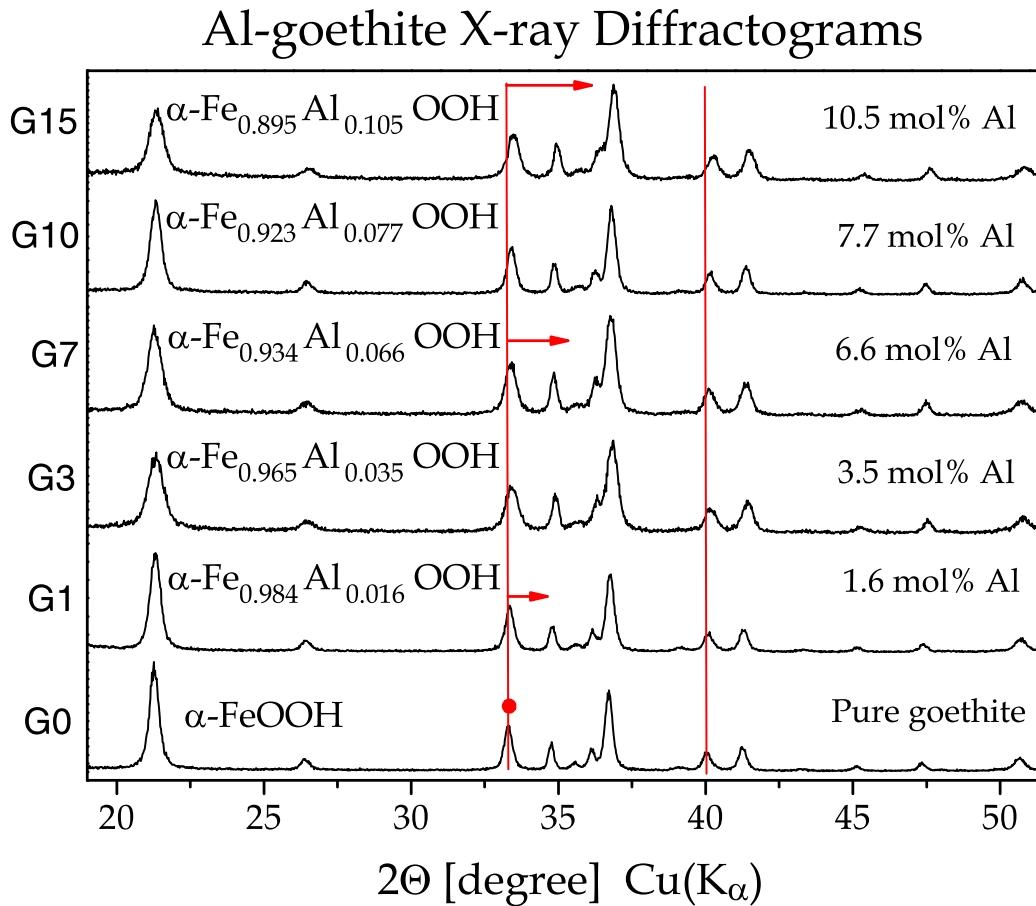


Figure 5.7: X-ray diffractometry patterns for the six reference samples. The vertical lines highlight the shift of the reflective plane to high 2Θ caused by the aluminum substitution. The higher the Al substitution of iron in goethite, the higher is the shift.

Magnetic susceptibility

Magnetic susceptibility of all reference goethites and four archeological samples were measured with a SQUID apparatus (Quantum Design, model MPSMXL at the Physics Institute of the University of Mainz). Two experimental setups were used, both with an external magnetic field of 10 kOe. First with temperature varying from 200 K down to 5 K to follow the antiferromagnetic behavior of the samples in this temperature range, recording the susceptibility every 3 K, step $3 \frac{\text{K}}{\text{min}}$. The second with temperature ranging from 400 K down to 200 K, step $1 \frac{\text{K}}{\text{min}}$ to calculate the Néel temperature (T_N). A set of temperature dependent molar magnetic susceptibility (χ_m)

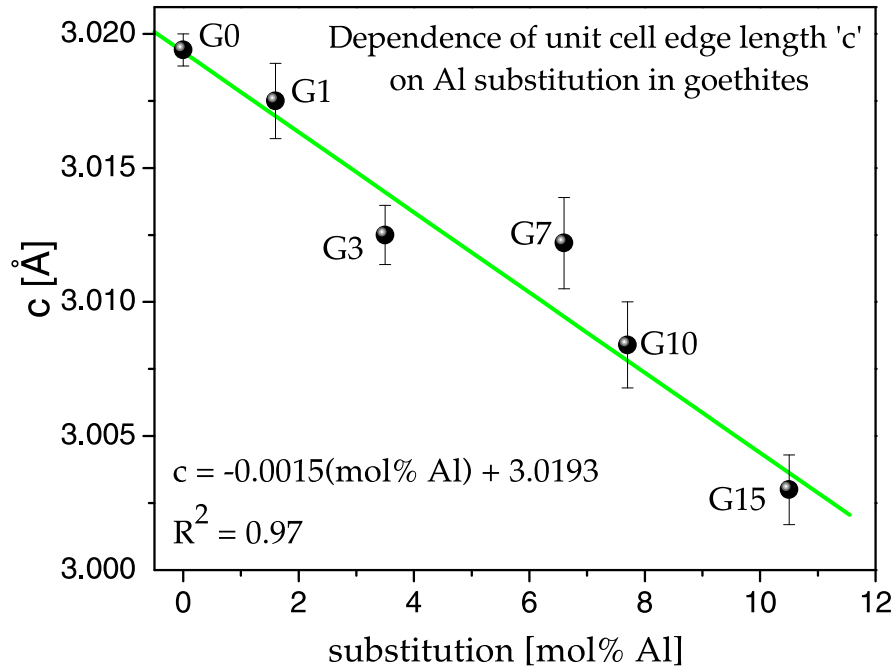


Figure 5.8: The linear dependence of the unit cell edge length 'c' of synthetic goethites against the level of structurally incorporated Al.

curves is shown in figure 5.9.

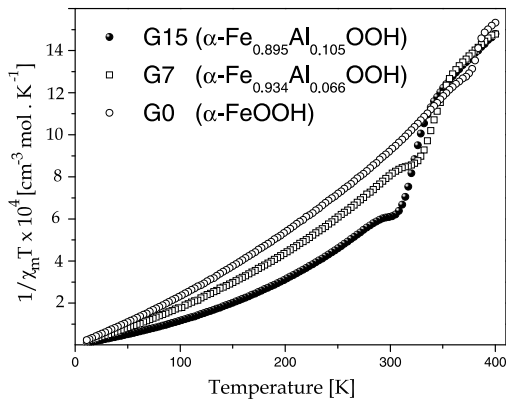


Figure 5.9: Temperature independent inverse of the magnetic susceptibility for three reference samples: (G0) pure goethite; (G7) with 6.6 mol% Al, and (G15) with 10.5 mol% Al. The Néel transition moves to lower temperatures as the Al content increases in the goethite.

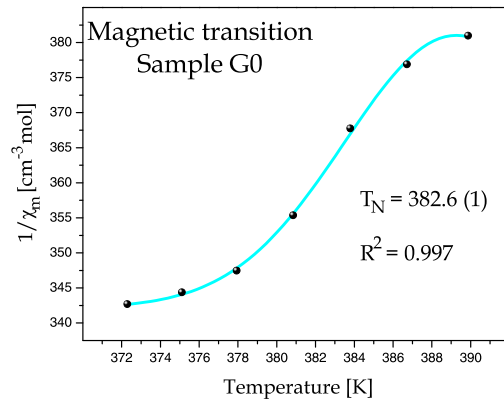


Figure 5.10: Magnetic transition on sample G0 (pure goethite) fitted with Boltzmann model.

The region where the magnetic transition is observed was fitted using a Boltzmann model where the transition point (considered as T_N) is calculated. The Néel temperature decreases linearly as the Al substitutes Fe in goethite (fig. 5.11). The obtained Néel temperature for pure goethite G0 was 382.6 K. Cornell and Schwertmann [Cor 03] reported Néel temperatures of 400 K for pure goethites.

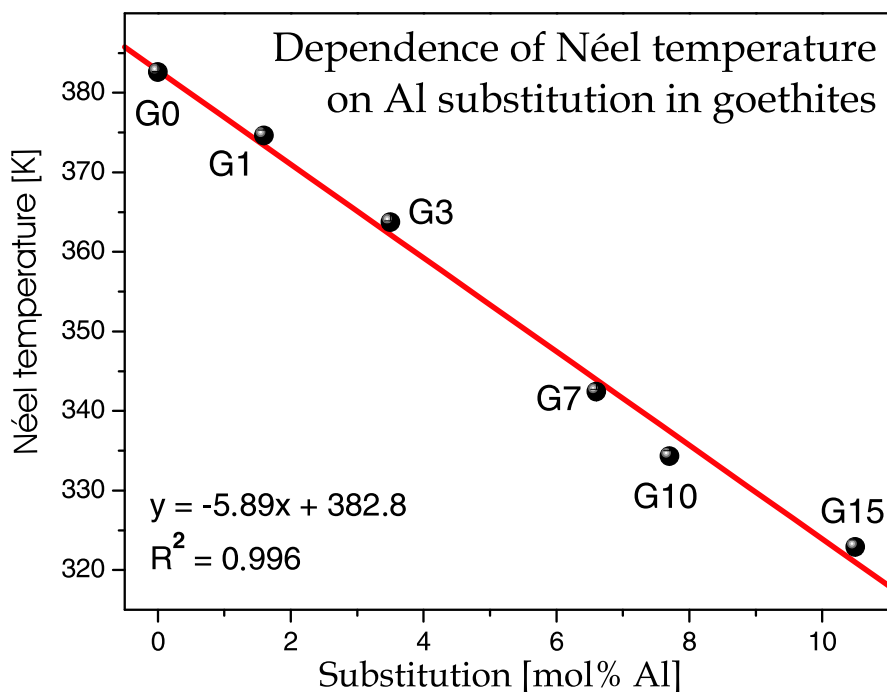


Figure 5.11: Linear dependence of the Néel temperature in Al substituted goethites.

Mössbauer spectroscopy

The Mössbauer measurements with the standard Al-goethite and the four archeological samples were measured at room (298 K), at liquid nitrogen (77 K), and at liquid helium (4.2 K) temperatures. Figure 5.5 shows the room temperature Mössbauer spectrum measured with MIMOS II on a sample (car A) of the interior of an ancient carriage wheel and figure 5.12 shows the least-squares fitted Mössbauer spectra for samples G0, G7, and G15 of Al-substituted goethites.

Super-paramagnetism and isomorphic substitution can be followed by

Table 5.5: Néel temperatures (T_N) for the standard and the sample removed from the archeological pieces.

Sample	mol% Al	T_N [K]	R^2
G0	0	382.6(0.1)	0.997
G1	1.6	374.6(0.7)	0.987
G3	3.5	362.7(0.2)	0.999
G7	6.6	342.4(0.3)	0.999
G10	7.7	334.3(0.7)	0.996
G15	10.5	322.9(0.9)	0.995

Figure in parenthesis are errors in Kelvin.

temperature dependent Mössbauer measurements and by other techniques such as X-ray diffractometry and susceptibility measurements.

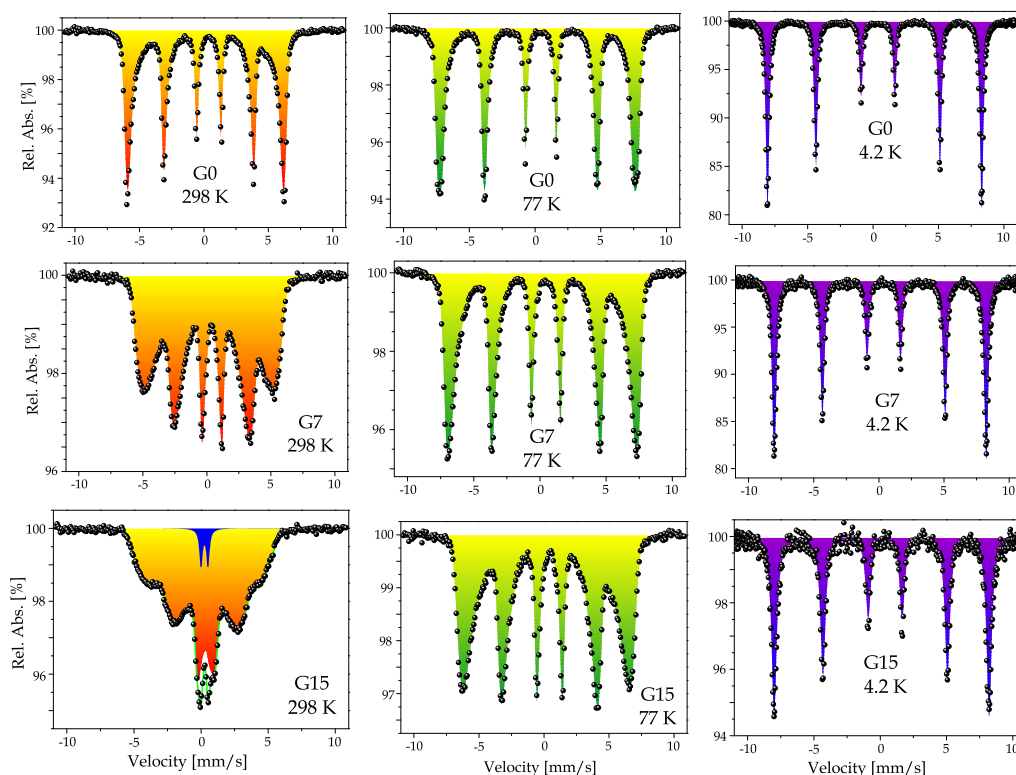


Figure 5.12: Mössbauer spectra recorded at 298 K, 77 K, and 4.2 K from three Al-goethite reference samples (G0, G1, and G15).

At room temperature, as the Al content increases in the goethite, an

increasing relaxation effect can be observed. At 77 K the relaxation effect is less intense, but an increase of the line width is observed as the Al content increases in goethite. At 4.2 K there is a saturation of the hyperfine magnetic field and all spectra are similar. Nevertheless, a decrease of the hyperfine magnetic field is observed as the Al content increases in goethite; considering that there are no differences in the average grain size in the samples. Therefore, to avoid other effects than the decrease of the magnetic field only the 4.2 K Mössbauer spectra are considered for the determination of Al content in the powdered goethite collected from the archeological samples. A linear relationship between the Al content in goethites and the hyperfine magnetic field at 4.2 K was observed (fig. 5.13).

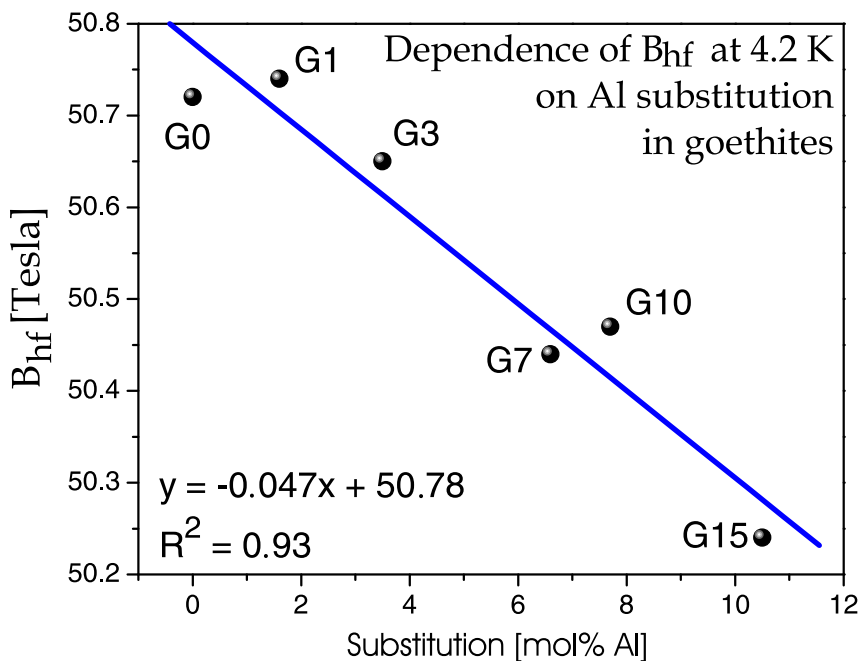


Figure 5.13: The linear relationship observed for the Al content in the goethite samples against the hyperfine magnetic field at 4.2 K.

Four samples from different artifacts were analyzed also by SQUID and Mössbauer spectroscopy at 4.2 K. The results obtained for the T_N and the calculated Al content is shown in table 5.6.

The limitation of this method to determine the Al content of goethite is to assume that the decrease of the hyperfine magnetic field is not caused by other elements (e.g., Si). Nevertheless, this gives an idea on the maximum Al content to be expected for the analyzed sample. The concentration of Al

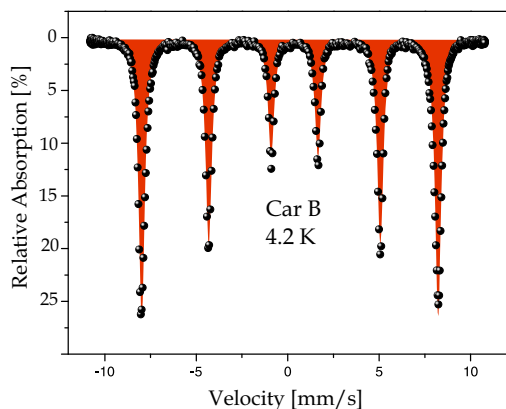


Figure 5.14: Least-square fitted Mössbauer spectrum of sample car B recorded at 4.2 K. Obtained $B_{hf} = 50.3$ T, resulting in a calculated Al concentration in goethite of 11.3 mol% Al.

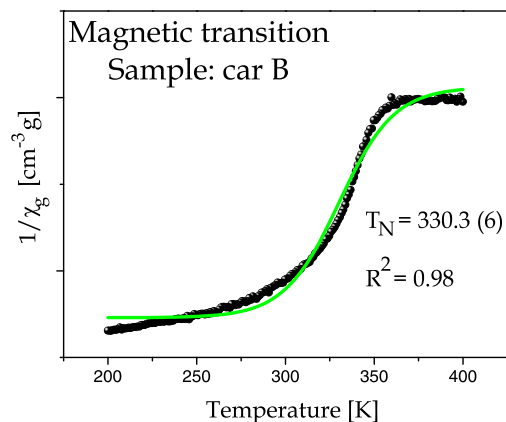


Figure 5.15: Magnetic transition on sample car B fitted with Boltzmann model. Obtained $T_N = 330.3$ K resulting in a Al concentration in goethite of 8.9 mol% Al, 21% smaller than the value calculated via Mössbauer spectroscopy.

obtained by chemical analysis is not sufficient to calculate the Al content substituting Fe in the goethite structure. Another potential use of this method is to decide either a piece belongs to the carriage or to another element found in the same excavation. Few mg will be required for this analysis. If powdered goethite from different fragments found at the same place diverge much, this would indicate that those pieces belong to different specimens. The use of SQUID will be of limited help in samples containing more than one iron oxide (e.g., magnetite) in addition to goethite. For such samples, Mössbauer spectroscopy measurements will be more appropriate.

Table 5.6: Al-goethite estimations from the calculated Néel temperatures (T_N) and from the hyperfine magnetic field B_{hf} obtained at 4.2 K.

Sample	Description	T_N [K]	mol% Al SQUID	B_{hf} [T]	mol% Al Mössbauer
car A	wheel/wood	305.0	13.2	50.5	6.0
car B	hub	330.3	8.9	50.3	11.3
car C	wheel	338.3	7.6	50.4	8.1
car D	unidentified	277.7	17.8	50.0	16.6

Table 5.6 presents the calculated values of Al in goethite (in mol%) for the four samples from the ancient carriage. Except for car A sample, data obtained from SQUID and Mössbauer show good agreement in the calculation

of Al content in goethite. The reason can be another element substituting iron in goethite (e.g., Si). Samples car B and car C are similar in Al concentration. These samples may have a close relationship in fabrication. The values of the hyperfine magnetic field are very close in these samples, which means that a very good Mössbauer spectrum has to be obtained for these calculations. The X-ray diffraction obtained from the archeological samples are poor in quality and they could not be used for Al estimation in the corrosion products. Considering the data manipulation necessary for the Boltzmann fitting, the Mössbauer data is preferable for these applications. Should another iron-bearing phase be present, in particular an oxide, the magnetic susceptibility will change drastically. In this case, only Mössbauer spectroscopy data will be effective.

5.3.2 Were iron artifacts burned in sacrifices?

Celtic helmet knob

The iron helmet knob ("Helmknauß") together with many other objects made of iron and bronze were discovered during an investigation of an area close to the village of Aldrans, Innsbruck, Tirol, Austria (fig. 5.16). The fired patina ("Brandpatina") on the findings suggests that these metal objects are the remains of a spot, where sacrifices were burnt. Since the third century B.C. it became customary in the eastern Alps to sacrifice weapons to *higher powers* by putting them into the flames on the altar.³ Afterwards these consecrations were deposited, i.e., buried somewhere in the grounds of the sanctuary. The motivation for this study is to determine if the Celtic helmet knob was burned in the past.

The helmet knob is depicted in figure 5.17 and its Mössbauer spectra obtained at room temperature is shown in figures 5.18 and 5.20. The Mössbauer spectra of the helmet surface show a doublet (likely to be $\beta, \gamma\text{-FeOOH}$) and three sextets (two associated to magnetite sites and one to $\alpha\text{-Fe}$). This set of lines was complemented by a broad hyperfine field distribution (fig. 5.19) with an isomer shift ($\delta_{av.} = 0.15$ mm/s) related to Rh. Least-squares fitted Mössbauer parameters are given in table 5.7. The profile of the hyperfine distribution can be decomposed into six Gaussians, centered at $B_{hf} = 33.0$ (fig. 5.19, 5.0%WSA, $\alpha\text{-Fe}$),⁴ 26.1 (3.8%, Fe-C or $\alpha\text{-FeOOH}$), 21.4 (3.5%, Fe_3C) Tesla. The other three Gaussians, centered at 12.2 (4.1%WSA), 9.7 (1.3%), and 4.8 (3.3%) Tesla, can be associated with super-paramagnetic

³The helmet knob of Aldrans is dated on third century B. C. according to data provided by the RGZM, Mainz.

⁴WSA denotes whole spectral area calculated by a fitting program.

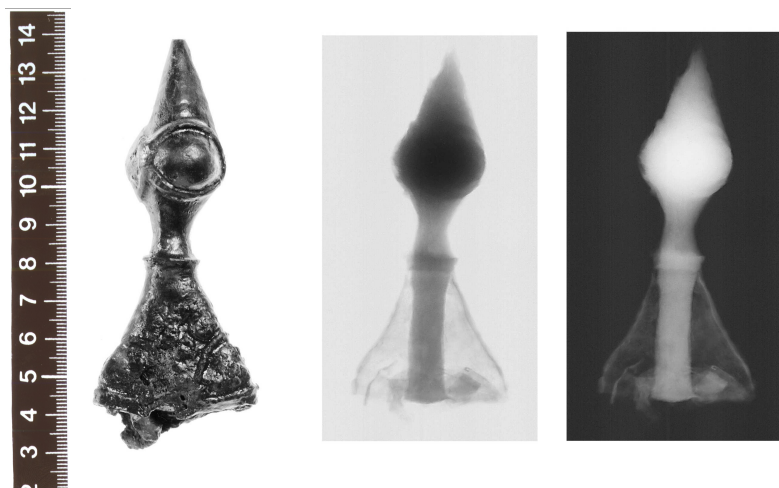


Figure 5.16: The analyzed Celtic helmet knob (left). The right picture is the X-ray photo of the piece and in the middle the diapositive of this photo.

goethite ($\alpha\text{-FeOOH}$).

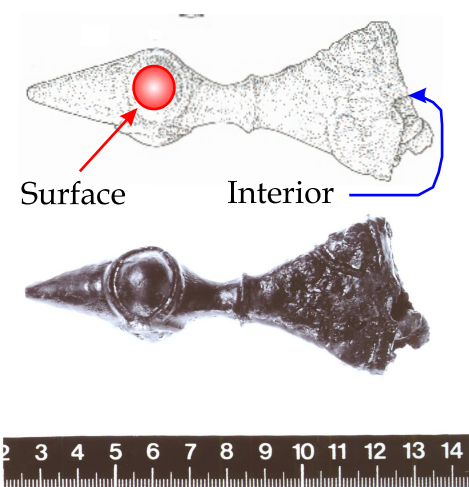


Figure 5.17: The analyzed regions of the Celtic helmet knob.

The room temperature Mössbauer spectrum of the helmet knob interior (fig. 5.20) has essentially the same spectral features of the surface: one doublet, three sextets and a broad hyperfine field distribution with an isomer shift ($\delta_{av.} = 0.15$ mm/s) related to Rh, however, with different phase concentrations. The hyperfine field distribution profile can be decomposed into

eight Gaussians, centered at $B_{hf} = 37.4$ (fig. 5.21, 4.0%WSA, likely to be associated to $\alpha\text{-FeOOH}$), 34.6 (2.0%, $\alpha\text{-FeOOH}$), 30.5 (4.5%, $\alpha\text{-Fe}$ and/or $\alpha\text{-FeOOH}$), 26.7 (10.7%, Fe-C and/or $\alpha\text{-FeOOH}$), 22.9 (2.4%, Fe_3C) Tesla. Super-paramagnetic oxide-hydroxide can be associated to the hyperfine field contributions at 15.1 (3.9%WSA), 9.7 (3.3%), and 5.3 (2.4%) Tesla.

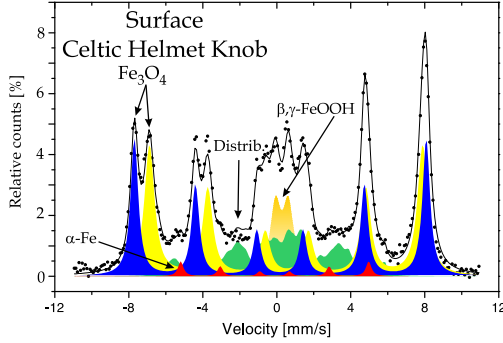


Figure 5.18: Room temperature Mössbauer spectrum of the Celtic helmet knob surface, least-squares fitted with four sites and a hyperfine field distribution.

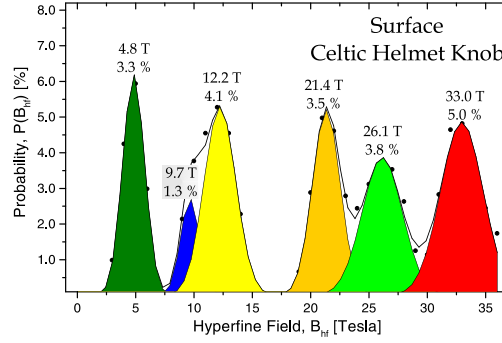


Figure 5.19: The distribution profile was numerically decomposed in six Gaussians.

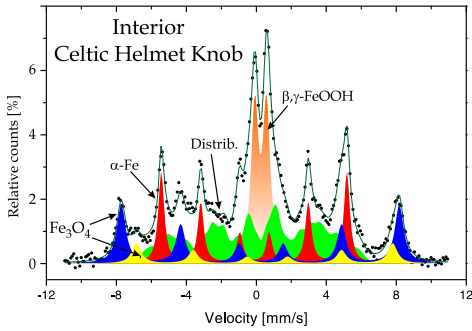


Figure 5.20: Room temperature Mössbauer spectrum of the Celtic helmet knob interior, least-squares fitted with four sites and a hyperfine field distribution.

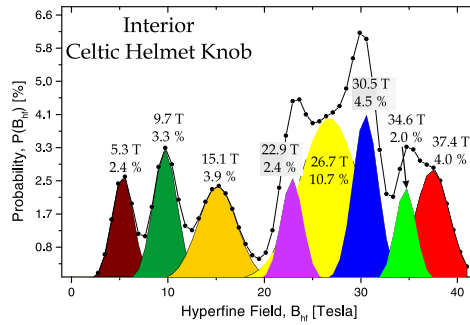


Figure 5.21: The distribution profile was numerically decomposed in eight Gaussians.

The room temperature Mössbauer spectrum of magnetite has twelve superimposed lines (two sextets). Each sextet represents different crystallographic sites. Site A (tetrahedral) is populated exclusively by Fe^{3+} ions and site B (octahedral) is populated by both ferric and ferrous ions. The magnetite observed at the surface of the Celtic helmet knob is, despite the slightly higher spectral area assigned to tetrahedral sites, almost stoichiometric. On the other hand, the same tetrahedral sites detected in the magnetite

of the knob interior is noticeably more intense. In addition, slightly higher values of B_{hf} were found for these tetrahedral sites. Both differences from the stoichiometric magnetite may occur because of oxidation of Fe^{2+} , transforming partially magnetite to maghemite ($\gamma-Fe_2O_3$). The substitution of Fe^{2+} by Ti^{2+} or Cr^{2+} can also cause the decrease of the Mössbauer spectral area related to the octahedral sites in magnetite. Both maghemite and the tetrahedral site of magnetite would not be clearly distinguished (as the reported parameters for both phases are quite similar). The transformation of magnetite to maghemite is possible at temperatures between 200 °C to 250 °C [Cor 03]. The higher the porosity of the rust magnetite, the lower the temperature and the easier is the oxidation of magnetite to maghemite. As no hematite is present, the temperature certainly did not exceed 300 °C (the temperature required to form the hematite from magnetite, e.g., [Cor 03]). Substituted magnetite and the non-stoichiometry also supports the hypothesis of partial oxidation of Fe_3O_4 by heating. Therefore, a corrosion process formed magnetite and, afterwards, the piece was heated at temperatures below 300 °C. This heating would be produced during a burning sacrifice. Burning evidences (such as ashes) substantiates such hypothesis.

Table 5.7: Room temperature Mössbauer parameters of the Celtic helmet knob.

Region	δ [mm/s]	Δ [mm/s]	B_{hf} [T]	Area [%]	Phase
Surface	0.29	0.02	48.9	29.2	Site A
	0.63	-0.04	45.8	37.5	Site B † magnetite
	0.00	0.00	31.5	2.3	α -Fe
	0.39	0.70		10.0	β, γ -FeOOH
				21.0	Distribution
Interior	0.36	-0.05	49.3	19.4	Site A
	0.66	-0.16	45.4	7.0	Site B magnetite
	0.00	-0.03	32.9	20.0	α -Fe
	0.36	0.70		20.4	β, γ -FeOOH
				33.2	Distribution

† similar Δ value as found for maghemite ($\gamma-Fe_2O_3$).

5.3.3 Identification of fragments

Once a historical artifact is found broken apart, the restorator has to collect the pieces that has some common properties (e.g., geometrical fit, surface

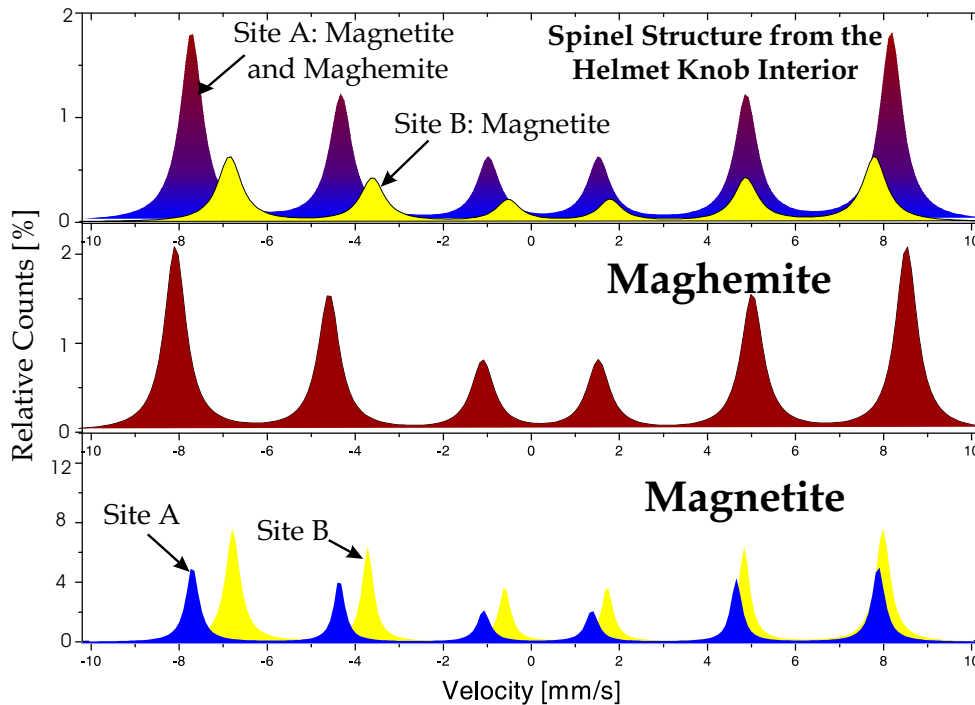


Figure 5.22: Standard magnetite, maghemite and the inverse spinel structure detected at the helmet knob interior.

texture, thickness, and color). Sometimes these property evidences are not clear and the restoration work cannot be done completely. The motivation of this study is to provide another method to determine if a given piece belongs to a broken artifact. As a case, a broken iron-bronze Roman mask was provided by the RGZM in Mainz.

Iron-bronze roman mask

A roman mask was found in excavations at "Villa von Allmend", Saarland, Germany. The mask is made of iron, covered externally by bronze. This kind of objects were used in war games during the height Roman times. During the excavations around the mask other metallic objects were also found. Some clearly belong to the mask, such as the left ear (fig. 5.23), among other fragments that cannot be associated with the mask without further investigation. Some of these unidentified fragments, as well as the left ear, were investigated using backscattering Mössbauer spectroscopy. The objective was to determine whether the fragment was a piece of the roman mask or was part of another object laying in the excavated area.

The room temperature Mössbauer spectrum of the roman mask (left ear



Figure 5.23: Left ear of the Roman mask.

without the bronze cover) was least-squares fitted using a set of two doublets, three sextets and a distribution of hyperfine field (fig. 5.24); which indicated then to be wüstite. Wüstite ($Fe_{1-x}O$) is a cation deficient oxide, which is equivalent to the fcc (face centered cubic) structure. This wüstite was formed during the confection of the mask, probably for the fixation of the bronze or for the formation of a patina layer. The temperature required for the formation of wüstite ranges from 570 °C to 750 °C. Two sextets are assigned to a stoichiometric magnetite. This magnetite could be formed by corrosion processes. The other sextet can be associated with maghemite or hematite. This ferric oxide may have been formed by heating of the magnetite, supported by the fact that this Roman village where the mask was found is known to have been burnt. Least-squares fitted Mössbauer parameters are given in table 5.8. The profile of the hyperfine field distribution can be decomposed into six Gaussians, centered at $B_{hf} = 46.1$ (fig. 5.25, 0.5 %WSA, $\alpha-FeOOH$), 40.91 (1.2 %, $\alpha-FeOOH$), 37.4 (4.2 %, $\alpha-FeOOH$), 33.1 (4.0 %, $\alpha-Fe$ or $\alpha-FeOOH$) Tesla. The other two Gaussians, centered at 27.8 (1.6 %WSA) and 23.6 Tesla (0.7 %) can be assigned to super-paramagnetic goethite ($\alpha-FeOOH$).

Two regions of the unidentified pieces were analyzed: inner and outer parts. The inner part was in contact with the user's face, should the mask be used. The outer surface was covered by bronze. The results obtained from those regions are clearly different. The room temperature Mössbauer spectrum of the unidentified piece shows maghemite, crystalline and super-paramagnetic hematite, but the outer region has magnetite (29.4 %WSA). The most important information obtained from the fragment is the absence of a detectable sign of wüstite. This identified phase at the mask is associated

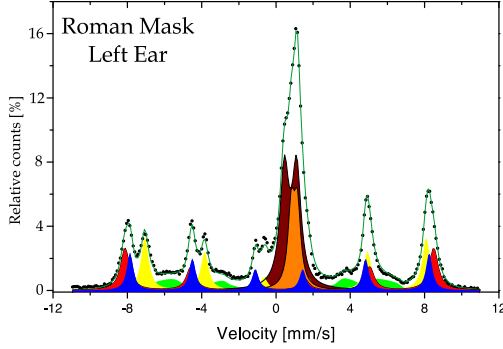


Figure 5.24: Room temperature Mössbauer spectrum of the left ear of the Roman mask.

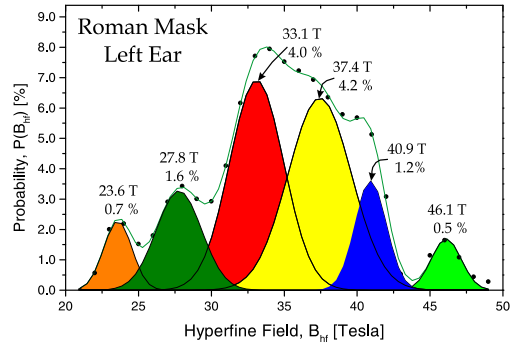


Figure 5.25: The distribution profile was numerically decomposed into six Gaussians.

to its manufacturing process. Therefore, the unidentified fragment cannot be associated with the Roman mask. This information is particularly important to the restoration work on the mask and could be obtained using a non-destructive technique (fig. 5.30).

Table 5.8: Least-squares fitted Mössbauer parameters of the Roman mask samples.

Region	δ [mm/s]	Δ [mm/s]	B_{hf} [T]	Area [%]	Phase
Roman Mask <i>Left Ear</i>	0.29	0.03	49.9	14.0	Site A
	0.64	-0.03	46.9	19.7	Site B magnetite
	0.32	-0.05	51.5	16.60	γ - Fe_2O_3
	1.10	0.32		12.5	wüstite, Fe_xO
	0.89	0.65		25.0	
			12.2	Distribution	
Fragment <i>Inner</i>	0.33	0.03	49.9	28.0	γ - Fe_2O_3
	0.39	-0.21	51.8	8.7	α - Fe_2O_3
	0.38	0.60		12.5	α - Fe_2O_3 , sp
				44.7	Distribution
Unident. Fragment <i>Outer</i>	0.32	0.03	51.5	10.6	γ - Fe_2O_3
	0.30	0.02	49.9	16.9	Site A
	0.64	-0.03	46.9	12.5	Site B magnetite
	0.39	-0.21	51.8	10.6	α - Fe_2O_3
	0.38	0.60		2.5	α - Fe_2O_3 , sp.
			46.9	Distribution	

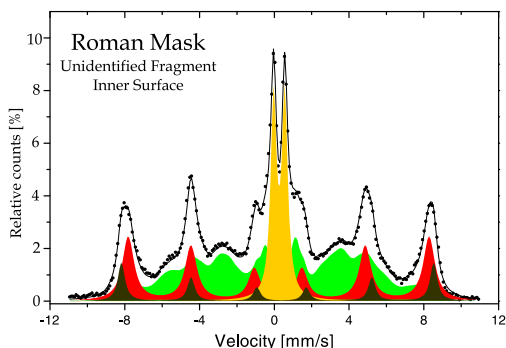


Figure 5.26: Room temperature Mössbauer spectrum of the unidentified fragment (inner surface) found close to the Roman mask during the excavations.

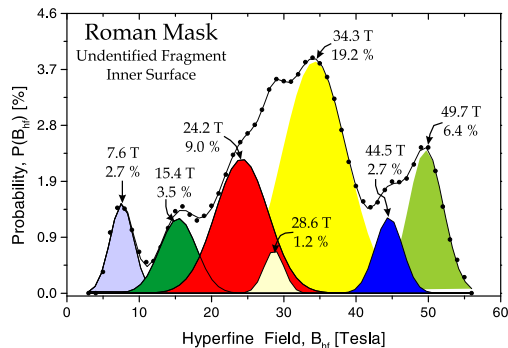


Figure 5.27: The distribution profile was numerically decomposed into seven Gaussians.

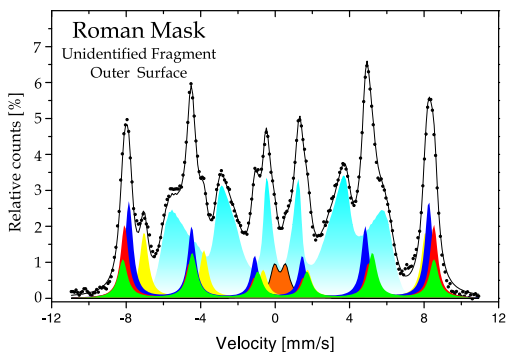


Figure 5.28: Room temperature Mössbauer spectrum of the unidentified fragment (outer surface) found close to the Roman mask during the excavations.

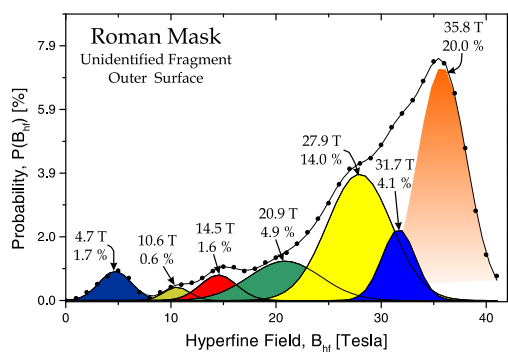


Figure 5.29: The distribution profile was numerically decomposed into seven Gaussians.

5.3.4 Pigment characterization

The literature reports the use of Mössbauer spectroscopy as an important tool for pottery and pigment analysis (e.g., [Des 03b] and references therein). These studies were performed either in fragments or in powdered samples. An entire archeological piece could not be studied by Mössbauer spectroscopy without scratching its surface or powdering the fired clay material. An ancient vase or its pigment (as shown in fig. 5.31) cannot be analyzed using a standard Mössbauer laboratory setup. A suite of archeological pieces were analyzed to demonstrate the use of MIMOS II in the non-destructive analysis of pigments. The selected pieces were from a Greek vase, a piece of a Chinese wall painting and a manuscript (miniature) illustration.



Figure 5.30: Right face of the reconstructed roman mask.

Greek vase

A Lekythos vase (500 years B.C.), kindly provided by the Römisch-Germanisches Zentralmuseum of Mainz (RGZM O. 24790), was analyzed by backscattering Mössbauer spectroscopy. This Lekythos vase has three black figures with red details painted on a yellow fired clay (fig. 5.31).

The Lekythos was built as an oil or perfume jar having an ellipsoidal body (wheel-made), narrow neck, flanged mouth, curve handle (hand made) from below the lip to the shoulder, and a narrow base terminating in a foot: used chiefly for ointments and religious (funerary) ceremonies. This is substantiated by the fact that Lekythoi have been found in and around tombs and excavated from ancient homes. A Lekythos is quoted in *The Odyssey*: "*Nausicaa receives bath oil in a golden Lekythos which she uses to refresh Ulysses after landing at the island of the Phaeaces before returning to Ithaca*".⁵

Mössbauer backscattering spectra were recorded at room temperature with MIMOS II in three different regions of the Lekythos vase (fig. 5.31). One was on non-painted surfaces (region 1) and the other was on the painted surfaces (only black painted, and black with red details). Figure 5.31 illustrates typical results obtained at the other two regions. The analyzed Lekythos vase has three black figures with red details painted on a yellow fired clay (fig. 5.31). Identification of the iron-bearing phases in the fired clay would require low temperature Mössbauer measurements on powder samples.

⁵Homer, *The Odyssey* VI: 79 ff.

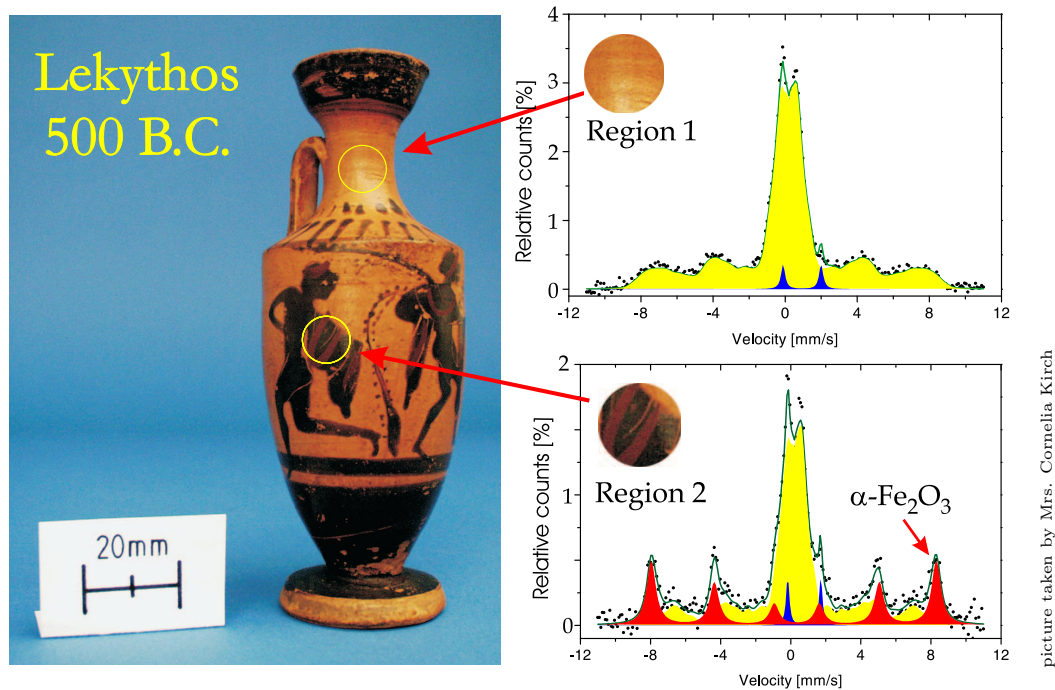


Figure 5.31: ^{57}Fe Mössbauer backscattering spectra of the Greek vase (*Lekythos*) measured at room temperature with a source of $^{57}\text{Co}/\text{Rh}$. Free painted surface shows a broad spectrum that can be associated with poor-crystallized iron oxides produced during the firing clay process. The painted surfaces shows, in addition to the characteristic non-painted area, a well defined sextet. The Mössbauer parameters of this sextet corresponds to a well-crystallized hematite. The Mössbauer spectrum taken over the red painted details shows no significant difference from the non-painted surface. Therefore, the red details are presumably iron free [Des 03b].

This cannot be done without damaging the vase.

Sampling depths can be estimated by calculation and by laboratory measurement. Direct calculation indicates that the sampling depth is $\sim 50 - 200\mu\text{m}$ for solid basaltic rock and $\sim 500 - 2000\mu\text{m}$ for fine grained basaltic dust for 15 keV γ -rays (i.e., approximately the same energy as the 14.4 keV). These calculations [Mor 00] were confirmed by backscatter Mössbauer measurements [Mor 01] of basaltic dust deposited to various thickness on rock substrates. This thickness includes the painted surface of the analyzed *Lekythos*.

Chinese wall paintings

The wall paintings of banqueting, acting, traveling and horse riding were discovered in the tombs group of the periods of Han and Wei dynasty. These paintings have great scenes and hectic atmosphere and reflect the fact that at that time the material richness and cultural life reached remarkably high standards.⁶

The samples come from an excavation that has been accomplished together with a Chinese Institute [Rgz 03]. The wall paintings come from a grave of a high military, dating to the Eastern-Han Dynasty. The site is in the district of Xunyi, Shaanxi Province, China. The later, or Eastern-Han Dynasty is referred to A.D. 25-220. In A.D. 25, a noble of the Western Han Dynasty, Liu Xiu who had participated in peasant insurrection and had eliminated other insurrection forces, founded his dynasty, and ascended to the throne, setting the capital in Luoyang. Liu Xiu called himself Emperor Guang Wu. Historians call his dynasty "Eastern Han Dynasty".⁷ The Han Dynasty is the East Asian counterpart of and contemporary with Rome in its golden age. During the Han Dynasty the Buddhism is introduced to China, at A.D. 43 Tonkin and Annam (southern and central regions of Vietnam) are conquered,⁸ paper began to be used at court by Ts'ai Lun (A.D. 105), and in A.D. 166 traders from the Roman Empire arrived in Tonkin.

A sample of 1 inch-square of an ocher wall-painting piece was studied by 14.4 keV Mössbauer spectroscopy. A backscattering geometry at room temperature and at 200 K with 100 mCi $^{57}\text{Co}/\text{Rh}$ source was used for both painted and non-painted sides for iron-bearing mineral investigations. Table 5.9 depicts the fitted Mössbauer parameters from the samples.

The Mössbauer spectra were recorded from the painted surface (ocher) and from the bottom of the piece removed from the wall. Both spectra show intense doublets and a low-intensity sextet. The Mössbauer spectrum was squared-fitted using three doublets (one as Fe^{2+} and two as Fe^{3+}) and one sextet (hematite). The Mössbauer parameters of the doublets are consistent with Fe-smectites (clays). The room temperature Mössbauer spectrum of the painted surface shows, in addition to the three doublets and the hematite, a broad sextet typical of goethite. Therefore, this broad sextet is the painting

⁶The development of wall paintings and mural-decorated tombs in the Han period, *The Bulletin of History and Philology, Academia Sinica* (March, 1986), vol. 57, pt.1. pp. 156-159.

⁷The English term for "China" comes from the name of the previous dynasty Ch'in

⁸R. J. Cima, *Vietnam a country study*, (Washington DC; US Government Printing Office, 1989); Duiker, William J., *Historical Dictionary of Vietnam*, (Metuchen, NJ, Scarecrow Press Inc., 1989).

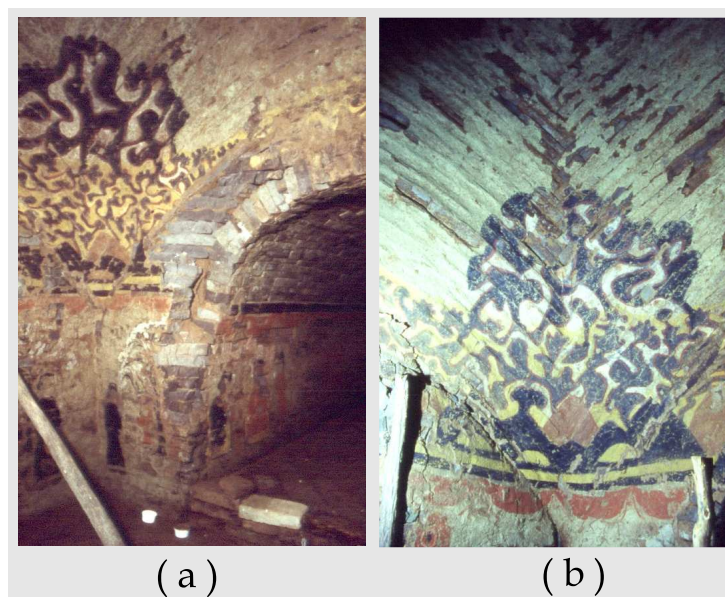


Figure 5.32: The wall painting, dating to the Eastern-Han Dynasty, found in the district of Xunyi, Province Shaanxi, China. The analyzed piece (fig. 5.33) was taken from the above yellow-ocher region(a): in detail (b).

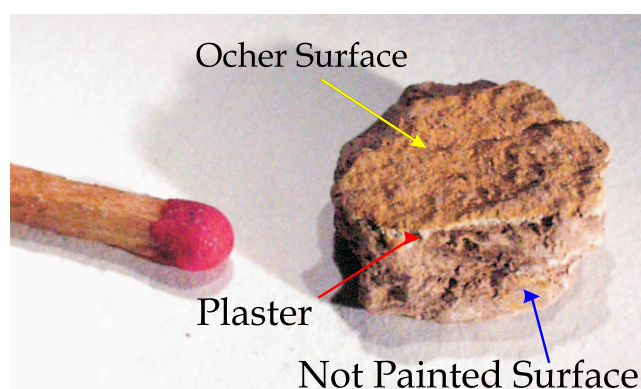


Figure 5.33: The analyzed piece of the wall painting. The upper part of the piece is the ocher painting, the lower is the wall itself (not painted) and the white layer between these surfaces is a carbonate plaster.

signature. Goethite, as already seen, is strongly temperature dependent. To ensure the presence of this goethite, a measurement of the sample was taken at 200 K. At this measurement the MIMOS II sensor head was also cooled at this temperature in a vacuum chamber. Powdered ocher painting material was measured at 78 K. The Mössbauer parameters are very consistent with goethite. Since no spectral relaxation was detected at 78 K, the grain size of

this pigment goethite is larger than 20 nm [Cor 03]. Therefore, the Chinese used fine-grained goethites for their other pigments in wall-paintings.

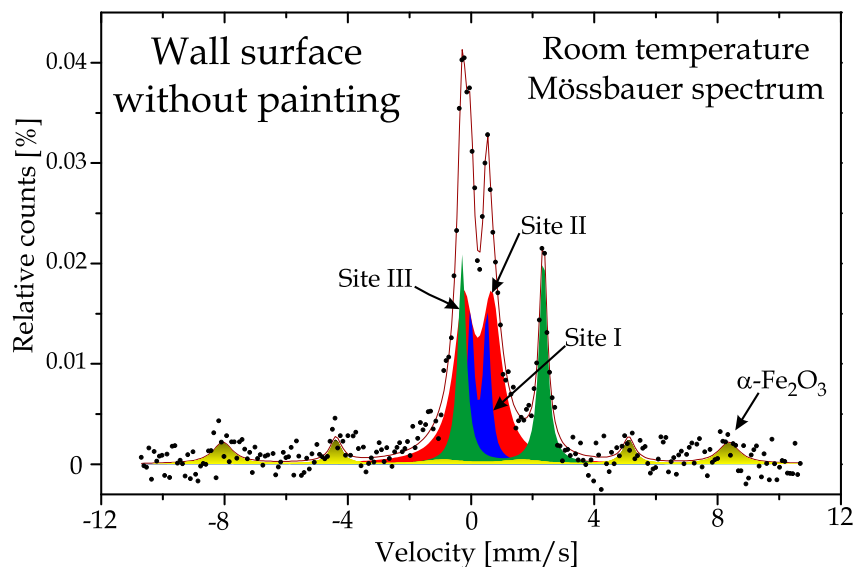


Figure 5.34: Mössbauer spectrum of the wall surface without painting recorded at room temperature.

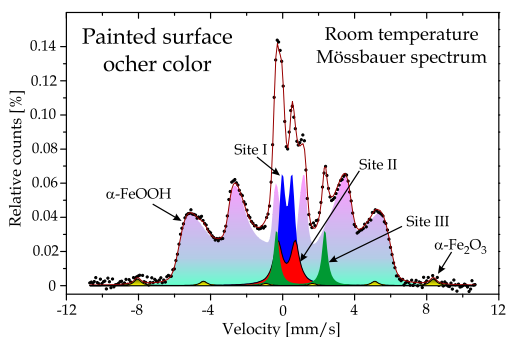


Figure 5.35: Room temperature Mössbauer spectrum of the ocher surface of the Chinese wall painting. The broader sextet corresponds to the painting material (goethite, α -FeOOH).

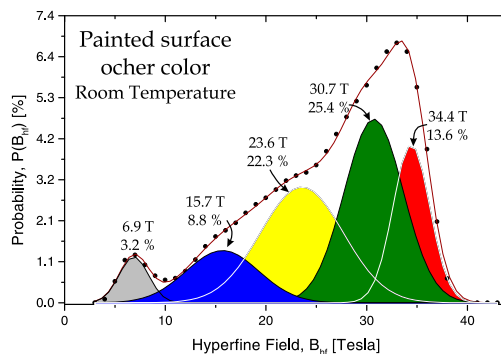


Figure 5.36: The distribution profile was numerically decomposed into five Gaussians.

Ocher pigment of a manuscript

A hand-made miniature, kindly provided by the Gutenberg Museum in Mainz, painted in vivid colors (e.g., mennige red, copper green and azurit blue) and

Table 5.9: Least-squares fitted Mössbauer parameters of the Chinese wall painting.

Region	δ [mm/s]	Δ [mm/s]	B_{hf} [T]	Area [%]	Phase
Not Painted	0.36	0.53		15.7	Site I: Fe^{3+} octa
	0.33	0.91		45.1	Site II: Fe^{3+} octa
	1.14	2.63		25.8	Site III: Fe^{2+} tetra
	0.37	-0.21	50.9	13.4	$\alpha-Fe_2O_3$
Ocher Color RT	0.36	0.54		12.3	Site I: Fe^{3+} octa [†]
	0.33	0.96		6.9	Site II: Fe^{3+} octa
	1.11	2.68		5.8	Site III: Fe^{2+} tetra
	0.37	-0.21	50.9	1.7	$\alpha-Fe_2O_3$
				73.3	Distribution
Ocher Color 200 K	0.36	0.58		14.9	Site I: Fe^{3+} octa [†]
	0.38	1.12		5.9	Site II: Fe^{3+} octa
	1.03	2.86		7.2	Site III: Fe^{2+} tetra
				72.0	Distribution [‡]
Ocher Color 78 K	0.44	0.59		20.4	Site I: Fe^{3+} octa [†]
	0.44	1.41		2.7	Site II: Fe^{3+} octa
	1.28	2.84		9.6	Site III: Fe^{2+} tetra
	0.48	-0.25	48.9	67.3	$\alpha-FeOOH$

[†] Site I may include super-paramagnetic $\alpha-FeOOH$; [‡] including $\alpha-Fe_2O_3$.

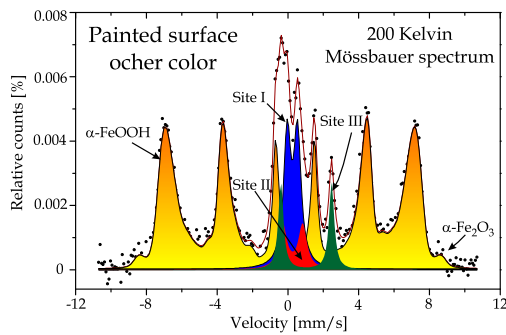


Figure 5.37: Mössbauer spectrum of the ocher surface of the Chinese wall painting recorded at 200 K.

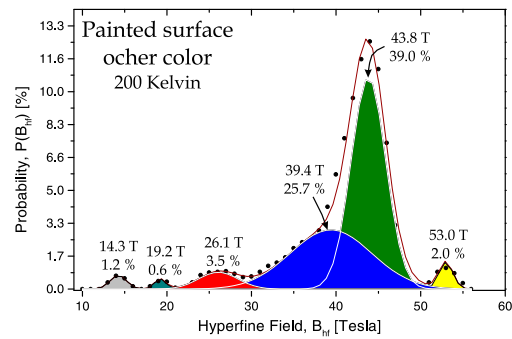


Figure 5.38: The distribution profile was numerically decomposed into six Gaussians. Hematite was included in the distribution.

with details in gold on parchment is dated to be from fifteenth century. The piece, probably made in the Netherlands, used as "Book of Hours", illus-

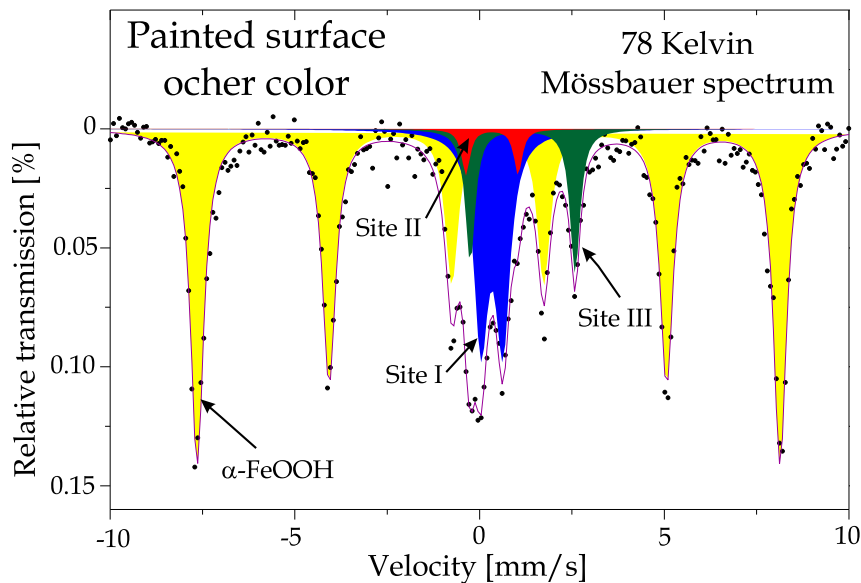


Figure 5.39: Powdered ochre painted surface recorded at 78 K at transmission geometry.

trates St. Christopher and has a prayer in the backside written in Latin. The motivation of this measurement was the non-destructive identification of possible iron-bearing compounds, understanding better the materials once used in the fabrication of the miniature.

From the analyzed regions, the only one with a detected Mössbauer effect was the yellow painted spot indicated in the figure 5.40. This illustration of soil below a tree is painted in two layers: an ochre ink under thin gold stripes.

The Mössbauer spectrum was recorded at room temperature during more than four days of measurement using a $^{57}\text{Co}/\text{Rh}$ source of 80 mCi. The Mössbauer effect was quite small (0.12 %). The Mössbauer spectrum shows a single doublet. The least-squares fitted Mössbauer parameters obtained are not related to any known published mineral ($\delta = 0.02$ mm/s, related to $\alpha\text{-Fe}$, and $\Delta = 1.05$ mm/s). This fact supports the conclusion that the pigments were artificially made and natural substances that were not used for the ochre pigment. The isomer shift value is consistent with Fe^{3+} . Brown yellow ("Braune Ocker") is reported by Schramm and Haring [Sch 80] as a mate color used in the time this miniature was fabricated. The brown yellow is related by these authors to tonerde (containing $\text{Fe}_2\text{O}_3 \cdot n\text{H}_2\text{O} \cdot \text{SiO}_2$) which is consistent to the ferric doublet obtained in the Mössbauer spectrum. The use of gold and fully detailed ornaments show how careful was its use and could explain how well conserved was such miniature [Kau 00].

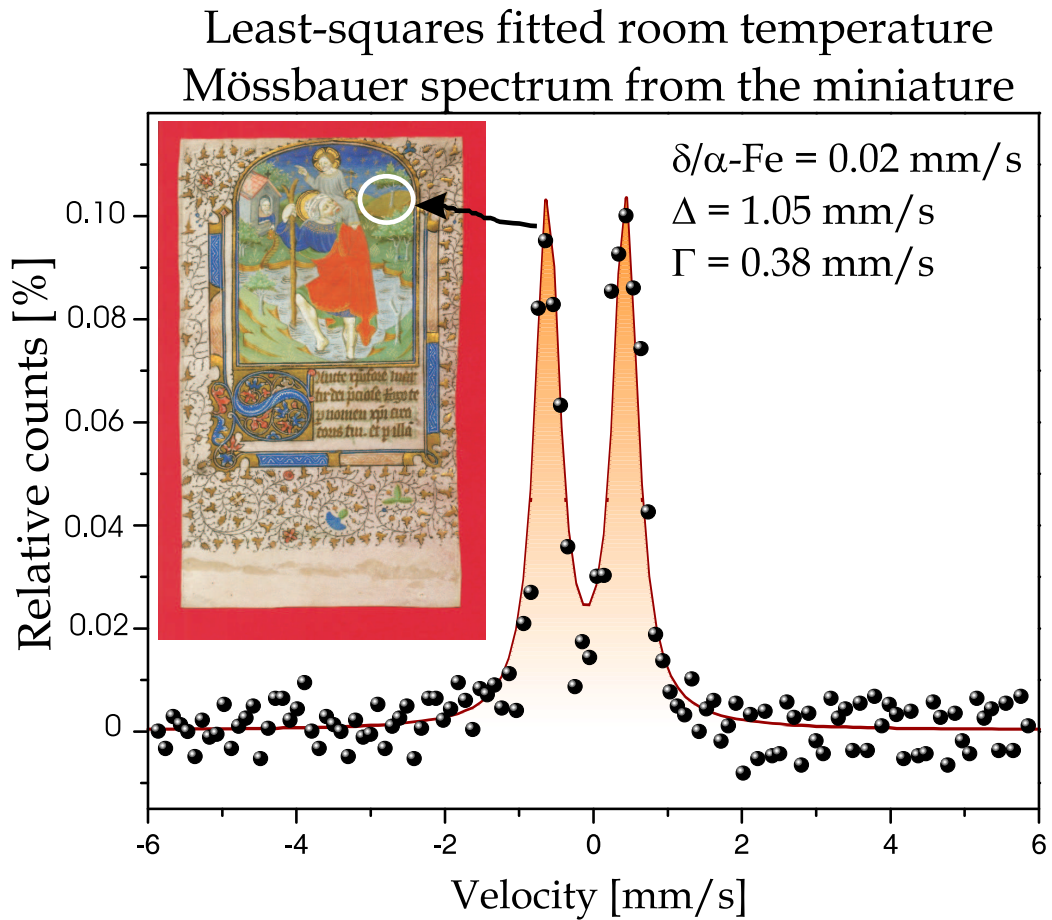


Figure 5.40: Room temperature Mössbauer spectrum of the miniature (ocher region highlighted in white) measured with MIMOS II. This Mössbauer spectrum was accumulated during $4 \frac{1}{2}$ days using a $^{57}\text{Co}/\text{Rh}$ Mössbauer source with 80 mCi of activity. The brown yellow is related to tonerde (containing $\text{Fe}_2\text{O}_3 \cdot n\text{H}_2\text{O} \cdot \text{SiO}_2$ as reported by [Sch 80]).

Chapter 6

Extraterrestrial applications

6.1 Introduction

^{57}Fe Mössbauer spectroscopy has been used in Earth-based laboratories to study the mineralogical composition of iron-bearing phases in a variety of planetary samples, including lunar samples brought to Earth by American Apollo astronauts and Soviet robotic missions, and meteorites that have asteroidal, Martian and Lunar origins (e.g., [Kli 03] and references therein). A variety of terrestrial samples that are analogues of Martian surface regions have also been studied by ^{57}Fe Mössbauer spectroscopy (e.g., [Mit 92] and references therein). Until recently, no in situ Mössbauer spectroscopy measurement was done as part of any planetary mission (e.g., [Mor 04]).

The scientific motivation for landing a Mössbauer spectrometer on Mars is extensively discussed by Knudsen et al. [Knu 92]. The scientific objectives of the MIMOS II on Mars are to identify the mineralogical composition and to measure the relative abundance of iron-bearing phases (e.g., silicates, oxides, carbonates, phyllosilicates, oxide-hydroxides, phosphates, sulfides, and sulfates), to distinguish between magnetically ordered and paramagnetic phases and provide, from measurements at different temperatures, information on the size distribution of magnetic particles, and to measure the distribution of iron among its oxidation states (e.g., Fe^{2+} , Fe^{3+} , and Fe^{6+}). Once obtained the data, it will be used to characterize the present state of Martian surface materials and provide constraints on climate history and weathering processes by which the surface evolved to its present state. The Mössbauer spectrum could, for example, identify primary igneous minerals such as iron-bearing olivine and pyroxene and weathering products which do (e.g., jarosite) and do not (e.g., hematite and maghemite) contain volatiles as a part of their structures.

Iron oxide particles can be formed by many different processes. Some of them were associated to Mars crustal formation (e.g., palagonitization [Mor 01] and hydrothermal associated with an impact event of a meteorite into a water-rich surface [Mar 92]). The Mössbauer analysis of Martian samples at different temperatures will help to understand which processes were involved in the iron oxide formation. Another question is whether the Martian meteorites can be related to actual materials on the Martian surface. Mössbauer spectroscopy can directly address this question through comparison of laboratory Mössbauer spectra from Martian meteorites and in situ spectra for the Martian surface, as done here with some meteorites (sec. 6.2) and Adirondack rock (fig. 6.16).

Because of the complexity of sample preparation, backscatter measurement geometry is the choice for an in situ planetary Mössbauer instrument (e.g., [Mor 88, Gal 89]). In this geometry, no sample preparation is required because the instrument is simply presented to the sample for analysis. On MER, the MIMOS II sensor head is mounted on a robotic arm that places it in physical contact with the analysis target (e.g., rock or soil) [Squ 03]. MIMOS II was similarly mounted on Beagle 2 [Sim 02].¹

As discussed above,² successful acquisition of Mössbauer spectra depends on accurate knowledge of the relative velocity of the source and the sample. External vibrations will cause poor Mössbauer spectrum. This degradation ranges from slight line broadening in mild cases to complete obliteration of the Mössbauer spectrum in severe cases. External vibrations are not generally a problem in laboratory settings because the sample and velocity transducer are rigidly held. On Mars and on outdoor terrestrial experiments, wind-induced vibrations are an obvious environmental factor that might degrade the quality of Mössbauer spectra. However, backscatter spectra obtained for hematite with a prototype of the MIMOS II instrument during field tests did not show detectable line broadening [Arv 98]. A noisy Mössbauer spectrum was recorded during the flight of the MIMOS II to Mars. Vibration or other physical effect could very the functionality of the drive of the Mössbauer instrument as observed in the health test performed during the flight to Mars (fig. 3.14). Fortunately, the first health check of the Mössbauer instrument after landing on Mars proved the instrument was working (fig. 3.15). The MER Instrument Deployment Device (IDD), a robotic arm used to place the Mössbauer instrument on targets, has been designed to assure that velocity

¹Beagle 2 is the name of the lander from the Mars Express mission from European Space Agency lost during entry to the Martian atmosphere on Christmas 2003.

²Cf. above sec. 2.2.1.

noise at the MIMOS II sensor head will not exceed 0.1 mm/sec [Squ 03].

This chapter describes the use of MIMOS II to characterize iron-bearing minerals in some metallic, chondrite and martian meteorites. Martian mineralogy is briefly discussed. Some of the measurements taken by MIMOS II onboard *Spirit* is presented, as well as the calibrations taken on Mars and the adopt strategy for data analysis.

6.2 Meteorites

Apart from Moon rocks, meteorites are the best extraterrestrial material available. Meteorites are classified into three main categories: stones, stony-irons and irons (called here metallic), depending on their composition. Irons are mostly metallic in composition, consisting of iron, nickel, and sulphur alloys. Stones are similar to common terrestrial rocks regarding their mineral composition which is dominated by silicates, a common rock-forming mineral on Earth. Stony-irons are combinations of irons and stony meteorites; which contain metallic and silicate phases in approximately equal amounts. Stones are subdivided into two classes: chondrites and achondrites. Chondrites are so named because most of them contain chondrules, tiny mineral spherules made mostly of silicates. Although some may be as large as a few millimeters in diameter, most chondrules are less than 1 mm across. Chondrites are the most primitive meteorites known. Achondrites represent more processed materials, like Earth's surface rocks. Detailed meteorite classification and characterization is given in many references (e.g., [Mcs 00]).

This section is devoted to analyze extraterrestrial materials and compile the mineralogy of some martian meteorites to further comparison with the analysis done on rocks and soil on Mars. The data provided from Mars surface from previous landing (Viking 1 and 2, and Mars Pathfinder) is the best information obtained before MER rovers on sample composition and indirect mineralogy from the surface of Mars. Mars analogue rocks are not common on Earth because of their high Br, S, and Cl composition. Comparing to terrestrial soils and rocks, Mars has much higher salt concentration probably because of the lack of recent water cycle.

A set of metallic and chondrites meteorites that fell in Brazil were kindly provided by the Brazilian National Museum in Rio de Janeiro for the MIMOS II characterization. Some fragments of Martian meteorites were provided by this museum as well.

6.2.1 Metallic meteorites

Instead of very thin slices or powdered pieces of the meteorites, entire meteorite surfaces or some large pieces were analyzed with MIMOS II. The advantage of this analysis is to preserve as much as possible of some unique samples and, no matter how big they are, they can be analyzed.

Five metallic meteorites (table 6.1) were measured by Mössbauer spectroscopy namely: Balsas, Crateus, Nova Petrópolis, and Pirapora. The relative amount of iron-bearing phases in the analyzed meteorites are shown in table 6.1 and the Mössbauer spectra obtained in two of them are presented in figure 6.1. Another metallic meteorite, Santa Catharina, studied in great detail by many authors (e.g., [Dan 79, Mit 92] and references therein) was also measured by the MIMOS II. The Mössbauer spectrum (fig. 6.1) shows two major components: an ordered/disordered Fe:Ni ($\sim 50:50$) phase with 43 %, and a paramagnetic phase associated with $\sim 28\%$ Ni, according to Danon et al. [Dan 79]. The results obtained by MIMOS II in this meteorite are in good agreement with the literature, where standard laboratory spectrometers were used.

Table 6.1: Relative spectral area of iron-bearing phases in the analyzed "Brazilian" metallic meteorites.

Meteorite	α -Fe	kamacite
	Area [%] [†]	
Balsas	98	2
Crateus	100	
Nova Petrópolis	100	
Pirapora	100	

[†] error $\sim 1\%$.

Figure 6.1 shows the Mössbauer spectra recorded at room temperature from Santa Catharina, Balsas and Crateus metallic meteorites. Barbacena presents in addition to α -Fe a small amount of kamacite (α -FeNi) (e.g. [Des 97]). Kamacite has usually a broad sextet pattern associated with a singlet ($\delta=0.05$ mm/s). Crateus, Nova Petrópolis, and Pirapora meteorites are dominated by α -Fe in their composition. These measurements were performed at room temperature during 12 hours using a $^{57}\text{Co}/\text{Rh}$ Mössbauer source of 100 mCi of activity. Such conditions will produce spectral statistics comparable to those obtained with MIMOS II during very long integration measurements on Martian surface.

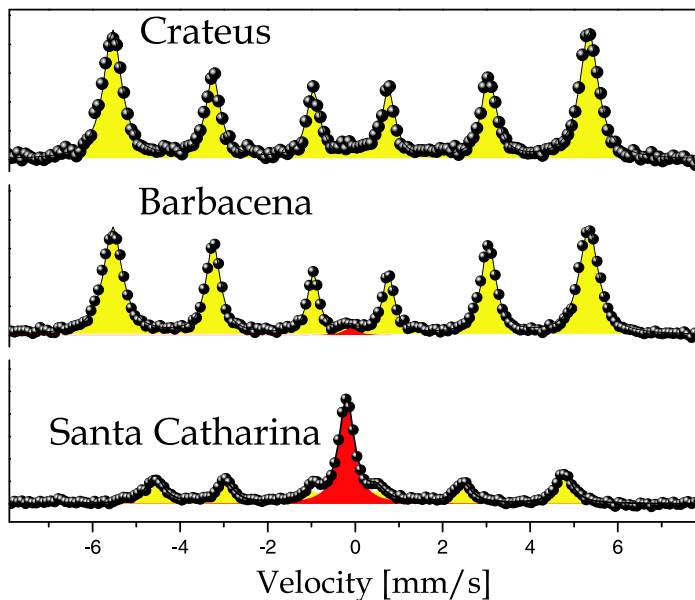


Figure 6.1: Least-squares fitted Mössbauer spectra of three metallic meteorites recorded at room temperature by MIMOS II.

6.2.2 Chondrite meteorites

Most common mineral phases containing iron in chondrite meteorites are olivine, pyroxenes, super-paramagnetic (sp.) Fe^{3+} , taenite ($Ni-Fe$), troilite (FeS), and metal iron ($\alpha-Fe$). The representative Mössbauer parameters of these phases are shown in table 6.2. These parameters can change depending on the sample. Figure 6.2 presents the Mössbauer spectra recorded by MIMOS II in four chondrite meteorites (namely Avanhandava, Uberaba, Macau, and Itapicurum-Mirin). Other two chondrites (Parambu and Paranaíba) were also studied. The relative concentration of the iron-bearing minerals in these meteorites is presented in table 6.3.

Resulting from Earth weathering between fall and the characterization some super-paramagnetic (sp.) Fe^{3+} can also be found. Some references associate sp. Fe^{3+} to weathering of troilite of other metal phases (e.g., [Mit 92]).

It is important to point-out the data quality obtained with MIMOS II in the measurements done on these meteorites. For these chondritic samples, up to seven iron-bearing phases were identified. In table 6.3 all meteorites but Avanhandava are also ordered as olivine content decreases. These meteorites are interesting for MIMOS II application on Mars because they have a high diversity of iron-bearing minerals. Avanhandava meteorite has a small taenite concentration and high concentration of olivine and of the M2 pyroxene

Table 6.2: Least-squares fitted Mössbauer parameters recorded at room temperature on some Chondrite meteorites.

Phase	δ [†] [mm/s]	Δ [mm/s]	B_{hf} [T]
olivine	1.14	2.99	
pyroxene M1	1.11	1.47	
pyroxene M2	1.14	2.08	
sp. Fe^{3+}	0.39	0.67	
Ni-Fe	0.00	0.04	33.6
troilite	0.75	-0.16	31.2
α -Fe	0.00	0.00	33.0

[†] related to α -Fe; errors in δ and Δ are 0.02 mm/s.

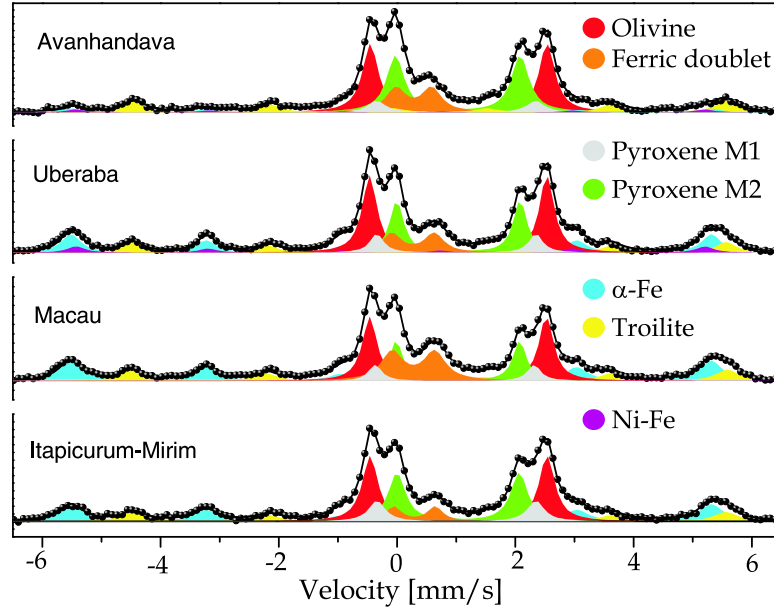


Figure 6.2: A series of chondrite meteorites analyzed by MIMOS II.

site.

Table 6.3: Relative Mössbauer spectral area for the iron-bearing phases found in the studied chondrite meteorites.

	Fe_T	<i>olivine</i>	<i>pyroxene M1</i>	<i>pyroxene M2</i>	<i>sp. Fe³⁺</i>	<i>taenite</i>	<i>troilite</i>	α -Fe
Meteorite	[%]	Area [%]						
Parambu	18.95	52.8	20.1	14.9	2.3	0.0	8.8	1.1
Paranaíba	20.86	38.1	16.0	22.7	3.6	4.0	11.2	4.4
Uberaba	26.08	29.8	6.8	18.8	9.5	18.6	10.8	5.7
Macau	26.27	25.0	5.8	14.4	16.7	24.4	13.4	0.3
Avanhandava	27.17	31.0	5.8	28.5	13.3	4.4	14.2	2.8
Itapicuru-Mirim	29.58	29.2	9.5	22.4	6.2	21.7	11.0	0.0

Note: errors in the spectral area are typically 0.3 % for doublets and 0.4 % for sextets; † average iron concentration reported by [Kei 80].

6.2.3 Martian meteorites

Evidence supporting "Mars as parent body" of SNC meteorites has been reviewed [Mcs 94].³ The SNC meteorites include volcanic (Nakhlites), basaltic (Shergottites) and plutonic (ALH84001, Iherzottites, and Chassigny) rocks [Mcs 00].

This section presents the analysis done with MIMOS II in five Martian meteorites (namely Governador Valadares, Zagami, NWA1068, Chassigny, and Dag476). On section 6.4 these results are briefly compared with the measurements taken on Martian rocks. Table 6.4 presents the results of the Mössbauer analysis of these Martian meteorites.

The relatively rich olivine and pyroxene content is a characteristic of SNC meteorites. Therefore, from these meteorites a high $\frac{Fe^{2+}}{Fe_T}$ ratio should be expected. No magnetic phase was detected in the five SNC meteorites analyzed here. Weathering products such as octahedrally ordered Fe^{3+} would also be expected. The genesis of these super-paramagnetic Fe^{3+} phases can be associated with water. The Fe^{2+} found in NWA1068 can be associated with ilmenite ($\delta = 1.11$ mm/s, related to α -Fe, and $\Delta = 0.70$ mm/s). Martian mineralogy is briefly discussed in the next section.

³Shergottites, Nakhlites and Chassigny: a group of differentiated meteorites for which Mars is suggested as the parent body.

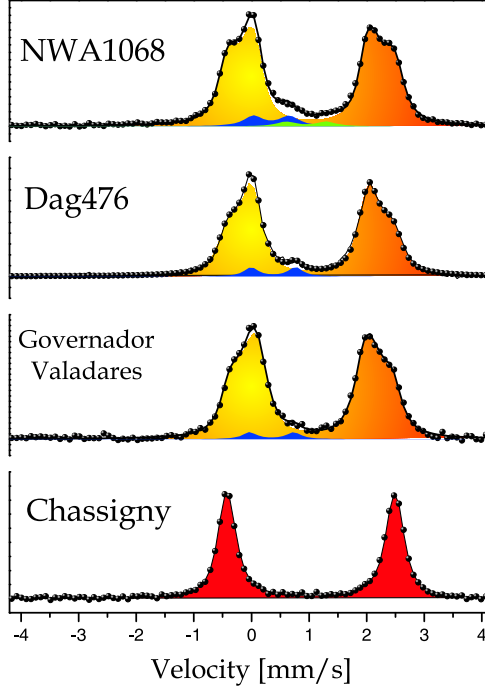


Figure 6.3: Mössbauer spectra of four SNC meteorites analyzed by MIMOS II and least-squares fittings with distribution of Fe^{2+} .

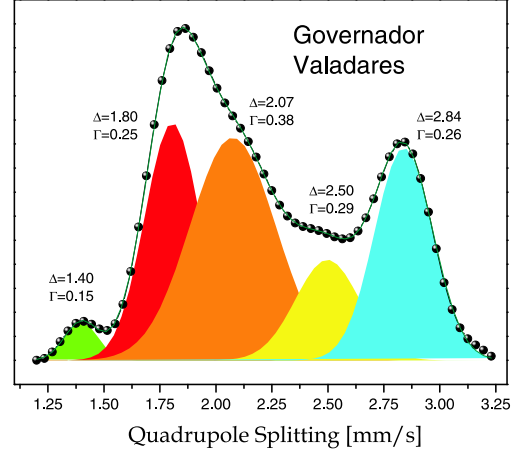


Figure 6.4: Least-squares fitting of the quadrupole distribution for the Governador Valadares meteorite. Five gaussians were used to fit the profile. This indicates that up to five distinct doublets can be used for fitting using distinct sites. Γ is the LWHM of the gaussian and Δ is its central value of the quadrupole splitting in mm/s.

Table 6.4: Relative spectral area of iron-bearing minerals in the Martian meteorites.

Meteorite	Fe_T			
	olivine	pyroxenes	sp. Fe^{3+}	Fe^{2+}
	[%]	Area [%] [†]		
Governador Valadares	19	78	3	
Zagami		96	4	
NWA1068	31	60	6	3
Chassigny	100			
Dag476	23	73	4	

[†] error $\sim 1\%$.

6.3 Martian mineralogy

The mineralogy of the surface materials on Mars has been directly measured in situ by NASA rovers [Squ 03]. The mission goals are to determine the aqueous, climatic, and geologic history of sites on Mars where conditions may have been favorable for the preservation of evidence of possible biotic processes. Martian lithosphere has been investigated by spacecraft accessing its age, structure, chemical composition, and petrogenesis [Mar 92].

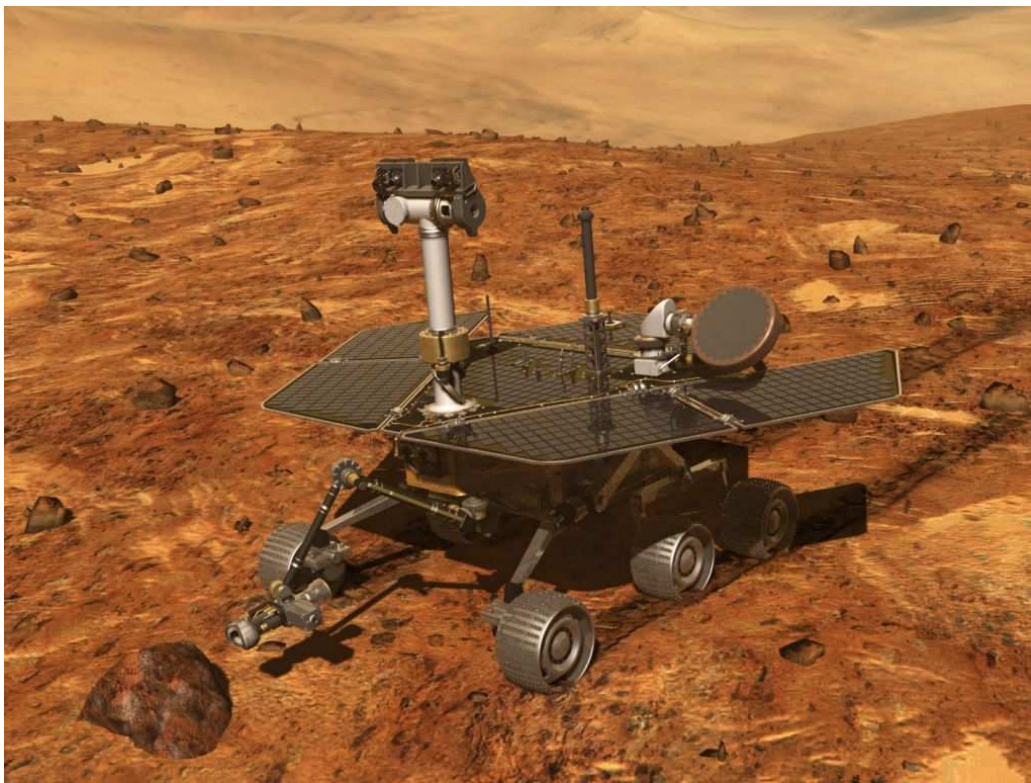


Figure 6.5: An illustration of one of the rovers from the Mars Exploration Rover mission, NASA.

Before this mission, by the use of various indirect approaches, including chemical correspondence to the surface analysis, spectral analogies, simulation of Viking lander experiments, some predictions on mineralogy were made. The direct analysis of the soil of Mars surface were performed by Viking landers (1 in Chryse Planitia - 13 samples; and 2 in Utopia Planitia: 8 samples). Clark et al. [Cla 77] reported results of all 21 samples. The sum of oxides is considerably less than 100% (table 6.5). Several reasons for this difference can be stated: light elements ($Z < 12$) could not be detected and

therefore, absorbed water, some hydroxides, carbonates, and nitrate minerals; certain elements such as Na, P, and Mn could not be detected because of interferences from major Mg, Cl, and Fe peaks in the X-ray fluorescence spectra; grain size and mineral heterogeneities cause lower-than-expected peak heights for major elements because of weathering rings or coating of large grains by smaller ones.

Table 6.5: Average chemical results from Viking and Mars Pathfinder.

Approximate Oxide Concentration		
$SiO_2 \sim 40\%$	$SO_3 \ 6.6 - 9.2\%$	$Cl < 1\%$
$Fe_2O_3 \sim 18\% \dagger$	$TiO_2 \sim 0.6\%$	$Br \text{ trace}$
$Al_2O_3 \sim 7\%$	$K_2O < 0.15\%$	$P \text{ tentative}$
$MgO \sim 6\%$	$CaO \sim 6\%$	$P+Mn+Cr+Na = 2 - 3\%$

\dagger considering all iron as Fe^{3+} .

The very high iron content coupled with low levels of expected trace elements and low K/Ca ratio pointed to a *mafic or ultramafic* source material. The sulfur concentration is two orders of magnitude higher than typical igneous rock. Viking and Pathfinder missions could not collect lithic fragments that would not contain S and Cl. Clark and Baird [Cla 79] suggested that the S and Cl content result from the addition of these elements as volcanic gases. Correcting the Viking fluorescence data in this manner produces a much different igneous composition, which closely matches the Shergotty meteorite, as first pointed out by McSween and Stolper [Mcs 80].

In addition to chemical results obtained by Martian landers, studies on Martian meteorites are also important. Nevertheless, the question of what is Martian and what is terrestrial contamination in SNC meteorites is still not resolved. A compilation of candidates of minerals proposed by studies based on chemical correspondence with the elemental analysis of the soil, the remote sensing of spectral observations on Mars, simulations of Viking biology and other Viking lander experiments, Pathfinder, *Spirit* and *Opportunity* results, and various thermodynamic modeling efforts were and still being reported by many authors.

The presence of clays on Mars is quite controversial. Smectites were considered by some authors (e.g., [Goo 78, Ban 83, Ban 85, Hub 79]);⁴ nontronite was assumed to be part of Martian mineralogy [Cla 77] and also excluded [Goo 78]. Beidelite was suggested also as a Martian surface mineral

⁴Cf. table A.15 for a list of phyllosilicate minerals.

[Zol 87]. Iron oxides were proposed as an important Martian mineral phase [Sod 78, Gui 87], both amorphous [Sin 85] and cryptocrystalline [Mor 85]. Silicates were suggested [Bur 87, Hug 82, Too 77]. Sulfates [Goo 78b], calcium rich sulfates [Wen 88], and sulfates of sodium or magnesium [Cla 81] were also proposed. Jarosite was suggested by Burns [Bur 86]. Sulfide such as pentlandite ($(Fe, Ni)_9S_8$), pyrite (FeS_2), and pyrrhotite ($Fe_{1-x}S$) were reported (e.g., [Mar 92] and references therein). Carbonates were also considered [War 87].

Weathering processes can be traced and inferred from the characterization of mineral phases. The physical and chemical weathering have been an important subject of Mars investigation. Physical weathering processes include frost riving, temperature cycles and wind abrasion (dust and ice projectiles). The chemical weathering process, on the other hand, includes oxidation (uptake of oxygen to form oxides or more highly oxidized silicates), hydration (uptake of water to form minerals with structural OH^- or H_2O), carbonation (uptake of CO_2 to form carbonate minerals), and solution (dissolving of minerals in water).

6.3.1 Published Mössbauer parameters on Mars analogue minerals

Published Mössbauer parameters were organized for each mineral candidate to be found on Mars.⁵ The entire data bank contains Mössbauer data of 478 minerals containing iron were collected. There are, in this data bank, over 140 minerals containing iron and at least one other element found on Mars. This set of *Mars Analogue minerals* constitutes a well organized and complete electronic Mössbauer library [Des 03a]. There is an important reason to consider all possible minerals with this particular Martian composition (table 6.5): Mars was never investigated, in situ, before MER, by Mössbauer spectroscopy. Despite detailed literature on Mars analogue minerals, a conservative analysis is required and selecting all possible minerals once studied by Mössbauer spectroscopy might be an appropriate strategy. All elements in this broad list of minerals were studied in detail considering the statistics of the reported Mössbauer parameters (number of published parameters, average value, maximum, minimum and the calculated standard deviation of each parameter).⁶ Possible conditions that may affect the Mössbauer parameters

⁵Details are given in sec. 4.5.

⁶Cf. above fig. 4.9.

have been studied in great detail. Those conditions are cation substitution, concentration of Fe^{2+}/Fe_T , crystallinity, grain size, temperature, overlapping of other mineral spectral signature, etc. Some of these remarks are listed in the tables of app. A. This data set was also useful during fitting exercises with Mössbauer data obtained on Mars. This data set was also used to train an artificial neural network.⁷ This program was used during real-time surface operations of the MER mission (e.g., [Des 03a, Mor 04]).

6.4 Mössbauer experiments on Mars

The rover *Spirit* (MER-A) landed within the ~ 160 km diameter of the Gusev Crater (14.5692°S, 175.4729°E) on 3 January 2004. *Spirit* landed in a flat plain in Gusev Crater with local undulations at meters scale. Some hills reach ~ 150 m elevation to the east of the landing site (LS). Numerous small depressions are visible from LS referred as "Columbia Memorial Station" (CMS, fig. 6.6).⁸ Floors are partially filled with finer-grained, high albedo material.⁹

The floor of the plain consists of notably smaller rocks than in the three previous landing sites of Viking landers 1 and 2, and Pathfinder. The shape of the rocks at the CMS range from rounded to angular. The first soil observation yields results showing resistance to deformation by applied forces associated with deployment of the IDD and the rover wheels. Other soils, particularly beneath and around rocks like Adirondack, are darker, have a pebbly appearance, and also appear cemented. There are evidences for aeolian action at CMS such as high albedo wind tails behind rocks. Variable dust covering likely accounts for the appearance of lighter rocks and all observed so far are propositionally consistent with olivine basalts.¹⁰

This section starts describing the calibrations taken by MIMOS II at Gusev Crater on Mars which includes temperature measurements, the dependence of the spectral area of the measured internal calibration sample

⁷Cf. above sec. 4.6.1.

⁸Tentative designation not formally adopted by the International Astronomical Union.

⁹Albedo is the portion of light reflected by a body or surface. The albedo of snow is near the unit and for charcoal is near zero.

¹⁰Many hazardous, navigation, and panorama camera images can be accessed from the NASA website (www.nasa.gov).

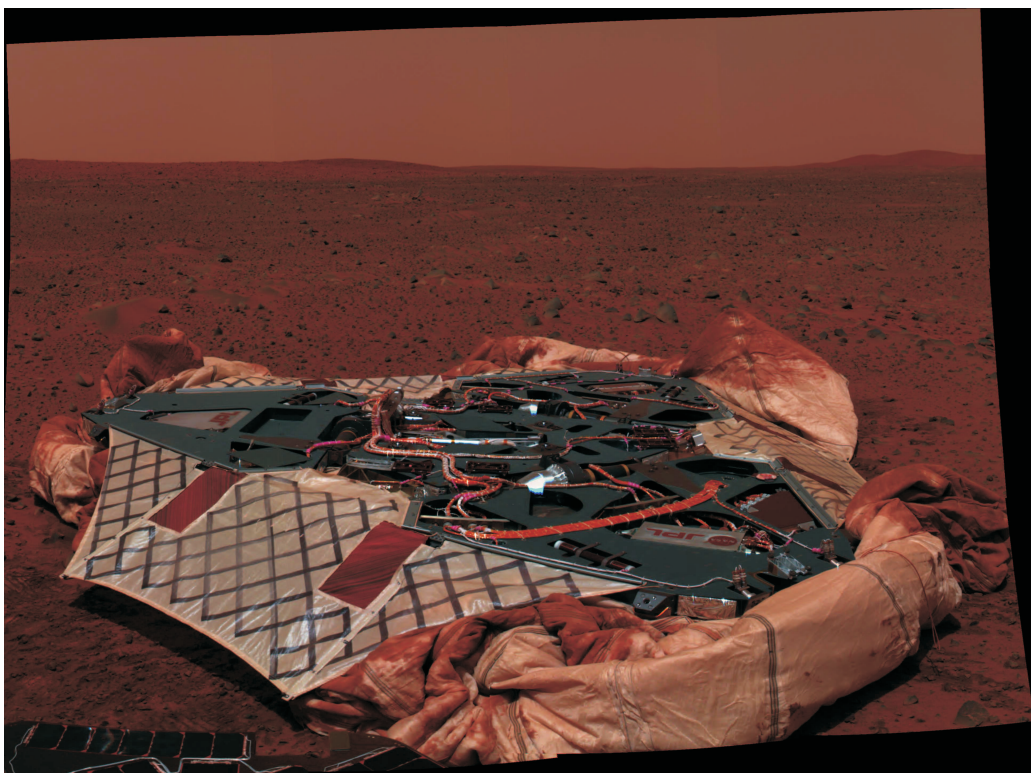


Figure 6.6: Pancam image of the Columbia Memorial Station, Gusev Crater, Mars (14.5692°S , 175.4729°E).

and of the hyperfine magnetic field on temperature, the applied strategy of data analysis, and, finally, some Mössbauer measurements taken by MIMOS II onboard *Spirit* on a Martian rock and soils around the landing site.

6.4.1 MIMOS II calibrations taken on Mars

Since the Mössbauer parameters are temperature dependent, it is important to know the temperature of the studied samples during Mössbauer measurements. The temperature on the Mars surface at the rovers landing sites varies from few positive degrees in Celsius down to approximately -80°C . Figure 6.7 illustrates the Martian surface temperature measured by a sensor installed in the MIMOS II sensor head. Temperature were recorded from 1210 LST-B (12:10 A.M., Local Solar Time - *Opportunity*) sol 10 to 1130 LST-B (11:30 A.M.) sol 11. Simultaneously to each Mössbauer measurement a calibration spectrum is recorded for a given temperature window. This window is set for the temperature measured by the thermometer installed at

the contact ring.

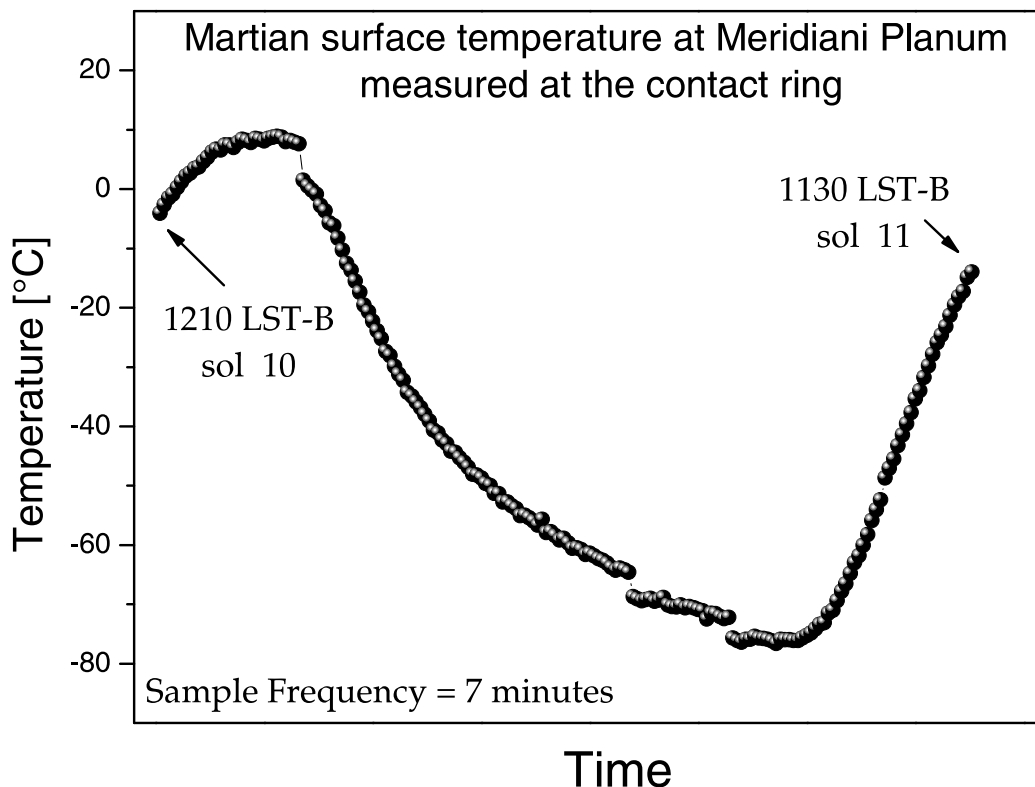


Figure 6.7: Martian temperature dependence on time at Meridiani Planum over a period of almost 24 hours. At the three discontinuity points temperature was not recorded because of data transmission (UHF passes). LST-B means Local Solar Time for *Opportunity* (MER-B).

Three parameters observed in the calibration of MIMOS II taken on Mars are discussed here: temperature dependence of the Mössbauer spectrum area and of the hyperfine magnetic field, and the isomer shift for the α -*Fe* in the internal calibration sample. Temperature behavior of the Mössbauer drive and the temperature effect on the energy spectrum (i.e., detectors and this electronics) will not be detailed here.

In the standard Mössbauer experiments, the increase of the spectral area (or effect) mainly results from the increase of the f_A as temperature decreases, since the source and the detectors are kept at room temperature. On Mars, the sample, the source, and the detectors are approximately at the same temperature. This results in a significant increase of the spectral area (ca. 2.5% per 10 °C decreased) and in an increase of the signal to noise ratio (fig.

6.8). In the temperature range of the Martian surface a significant change in the isomer shift was not observed. The recorded isomer shift for the α - Fe in the internal calibration sample was $\delta = -0.114(2)$ mm/s, relative to the rhodium matrix.¹¹

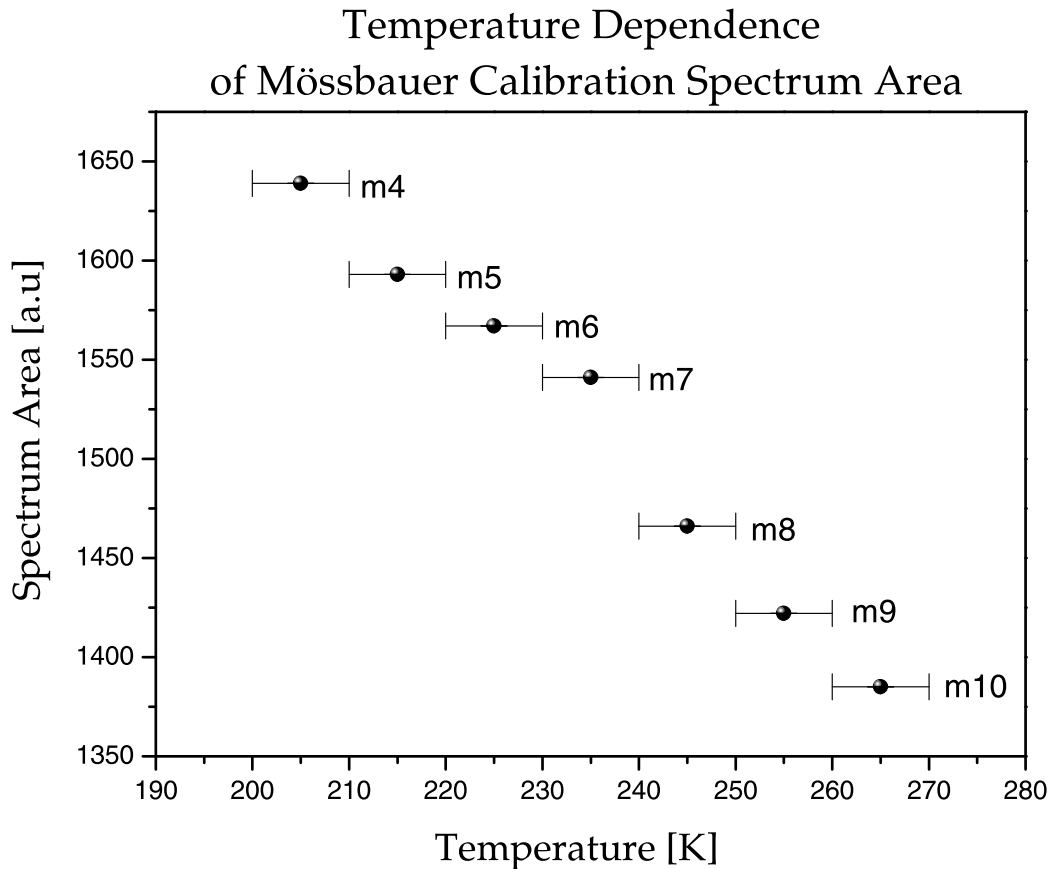


Figure 6.8: Temperature dependence of calibration spectrum area of the measurements performed on Mars by the MIMOS II onboard *Spirit*. All these measurements, recorded during the first 65 sols, were performed at the same drive velocity. Error bars in temperature stands for the temperature range of each window (10 K).

The hyperfine magnetic field (B_{hf}) for the α - Fe in the internal calibration sample is strongly temperature dependent. With the purpose of obtaining good spectral statistics, all Mössbauer measurements done in a given temperature range (from 200 - 210 K for m4, up to 270 - 280 K for m11) were integrated in a separate spectrum. Figure 6.9 depicts the temperature dependence of B_{hf} and shows the Mössbauer spectrum of compiled from all

¹¹Cf. above sec. 3.7.3.

measurements taken through the first 65 sols in the m9 range (250 - 260 K).

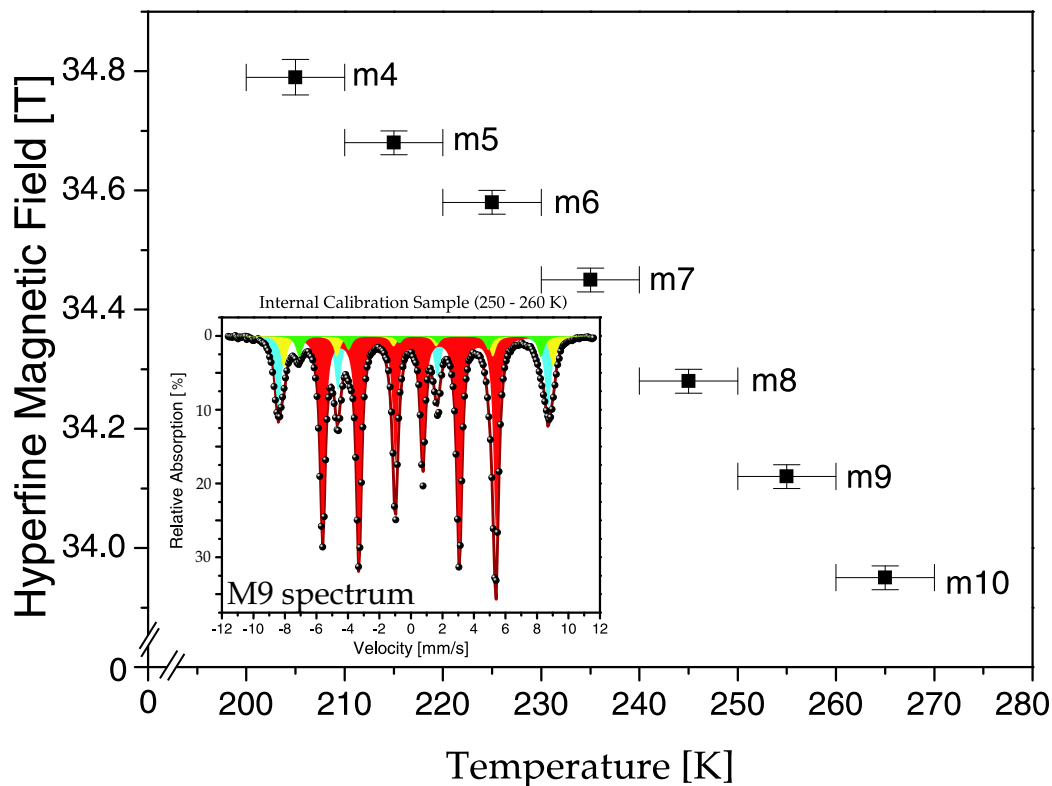


Figure 6.9: Hyperfine magnetic field dependence on temperature for α -Fe in the internal calibration target recorded on Mars shows a linear relationship. The fitted Mössbauer spectrum corresponds to the sum of all data accumulated during the first 65 sols in the m9 temperature window (250 - 260 K). At this temperature interval the hematite in the spectrum suffered Morin transition (see sec. 2.3.4).

6.4.2 In situ experiments on a Martian rock and soils

Several Mössbauer measurements taken on Mars surface were performed by MIMOS II Consortium lead by Dr. Göstar Klingelhöfer from the Institute of Inorganic and Analytical Chemistry of the Johannes Gutenberg University in Mainz, with support of MER engineering and science teams. In this thesis three soil and two rock measurements taken by *Spirit* at Gusev Crater will be presented and discussed. Data obtained by the rover *Opportunity* is not reported here. Table 6.6 presents details of the measurements on soils and on Adirondack rock, both on dusty and brushed surfaces. Brushing was done

using the RAT device (Rock Abrasion Tool, [Gor 03]).

Table 6.6: Mössbauer measurements on three soils and on a dusty and brushed region of Adirondack rock taken by MIMOS II on *Spirit* at Gusev Crater.

Target Name	Sol	Integration Time	Temperature Range [K]	Remarks
First Soil	14	3h 25min	232-273	Soil at CMS, Fig. 6.6
SugarLoaf1	65	27min	242-245	Touch&Go, Fig. 6.10
Trout1	46-47	9h 25min	209-255	pre-trenching †
Adirondack	Dusty	17-18	12h 26min	211-238
	Brushed	33	6h 13min	236-267

Note: † trenching is an activity to expose subsoil using a rover wheel for IDD experiments.

6.4.3 Strategy of Mössbauer data analysis

The Mössbauer spectra obtained from natural systems are complex. The number of singlets, doublets or sextets sometimes is not unique for a given mineral and several fitting results can be obtained. Relaxation effects sometimes also takes place in minerals. This problem can also increase on Martian temperature variation. Nevertheless, for most of the samples measured at Gusev Crater the Mössbauer spectra show small or none temperature dependence. Therefore, some Mössbauer spectra of the same sample recorded at different temperatures could be added improving statistics (sec. 3.5). An initial least-squares fitting using a distribution of quadrupole doublets for Fe^{2+} was used to support the decision on how many doublets should be used for the final fitting of the spectra. Systematically, three Fe^{2+} sites were obtained for all Mössbauer spectra recorded at Gusev Crater (fig. 6.12).

The Mössbauer spectra obtained with good statistics from rocks and soils at Gusev Crater (*Spirit*), during the first 65 sols of operations, are similar. The only difference seen in the spectra is the variation in the detectable relative concentration of iron-bearing species. The fitting strategy includes the preliminary fitting with quadrupole splitting distribution for Fe^{2+} , keeping the same isomer shift value ($\delta_{av} = 1.072$ mm/s, relative to the source of $^{57}\text{Co}/\text{Rh}$). The obtained distribution profile was fitted using three Gaussians which indicates the presence of three distinguishable sites ($\Delta_1 = 1.96$ mm/s, $\Gamma_1 = 0.24$ mm/s; $\Delta_2 = 2.27$ mm/s, $\Gamma_2 = 0.26$ mm/s; and $\Delta_3 =$

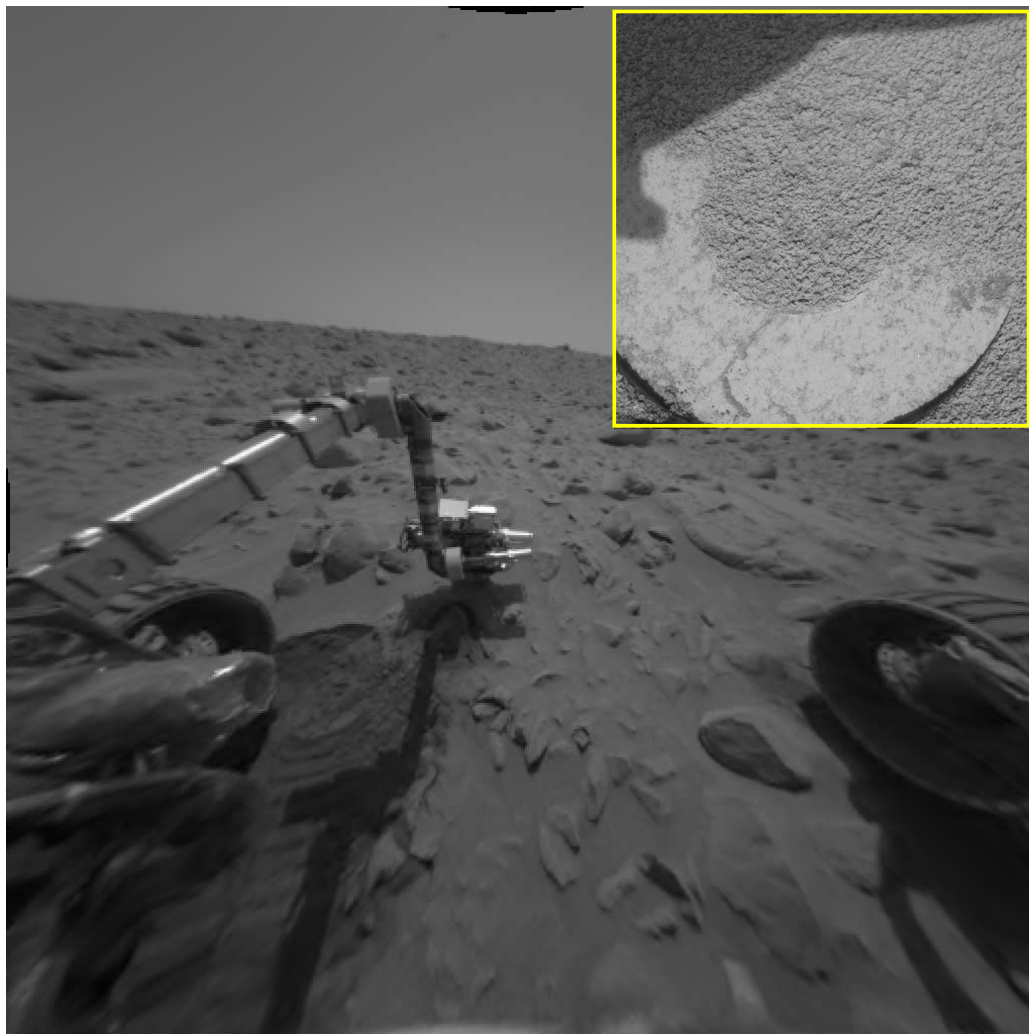


Figure 6.10: Front HazCam image recording the IDD placement in a soil spot on Sugar Loaf flats. A microscope image of the MIMOS II nose print is presented in detail.

3.10 mm/s, $\Gamma_3 = 0.46$ mm/s). Figure 6.12 illustrates the quadrupole splitting profile obtained for the dusty surface of Adirondack rock (*Spirit*, sol 18). The quadrupole splitting varied from 1.4 to 3.8 mm/s, keeping the isomer shift constant ($\delta_{av} = 1.072$ mm/s, relative to the source). The results obtained from least-squares fitting using the distribution approach can be slightly different from the fitting using separate doublets.

The least-squares fitted Mössbauer spectrum from the dusty Adirondack rock surface is presented in figure 6.11. This fitting, as for the majority of the recorded spectra, shows the presence of doublets related to olivine, pyroxene/glass and to a Fe^{3+} component. Good statistical Mössbauer spec-

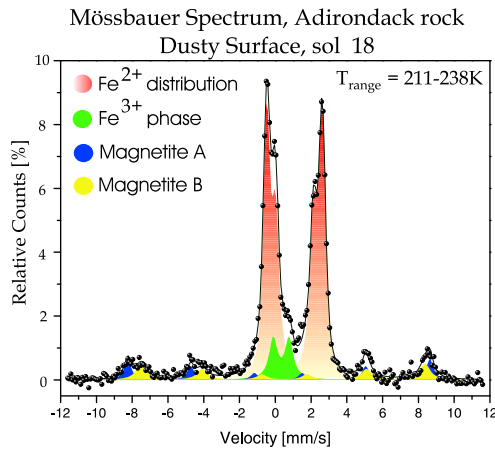


Figure 6.11: Least-squares fitted Mössbauer spectrum measured at the dusty surface of Adirondack rock. The spectrum was fitted with magnetite sextets, a Fe^{3+} doublet and the distribution of quadrupole splitting values. The quadrupole distribution is presented in figure 6.12

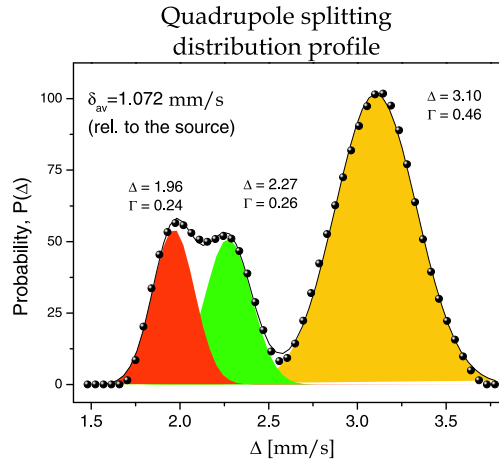


Figure 6.12: Least-squares fitted profile of the quadrupole splitting distribution obtained from dusty surface of the Adirondack rock. Three gaussians were used to fit the profile. This indicates that three distinct doublets have to be used for the final fitting. Γ is the LWHM of the gaussian and Δ is its central value of a given gaussian in mm/s.

tra recorded on soil show a small sextet assigned to magnetite [Mor 04]. Magnetite has been systematically detected in Martian rocks. Short time Mössbauer measurements on soil presented in this thesis may have a magnetite signal that could not be distinguished from noise. Therefore, magnetite was not considered in the fitting of short time measurements. Only long integration Mössbauer spectra on a soil spot show magnetite. Trout1 is one example of this long integration where a magnetic contribution could be detected and fitted.

6.4.4 Selected Mössbauer results from Mars

During the first 65 sols of *Spirit* at Gusev Crater many soils were measured. Some of these measurement activities were named "touch and go" (measurements on targets of opportunity, typically with an integration time longer than 15 minutes and shorter than 1 hour; e.g., Sugar Loaf),¹² "short inte-

¹²The name Sugar Loaf was chosen because of its resemblance to a mountain located in Rio de Janeiro, Brazil. Names are assigned to geographic features by the science team for planning and operations purposes. They are not formally recognized by the International

gration” (as constrained by other rover activities; e.g., First Soil), and also ”long integration” (e.g., Trout1). The soil measurements can be associated with trenching activities when all but one rover wheel are stopped. Table 6.7 shows least-squares fitted Mössbauer parameters obtained experimentally on soil samples. The Mössbauer spectrum was obtained from the integration of all temperature intervals. Therefore, a small line broadening of each sub-spectrum should be expected.

First Mössbauer Spectrum Recorded on Martian Surface, January 17, 2004

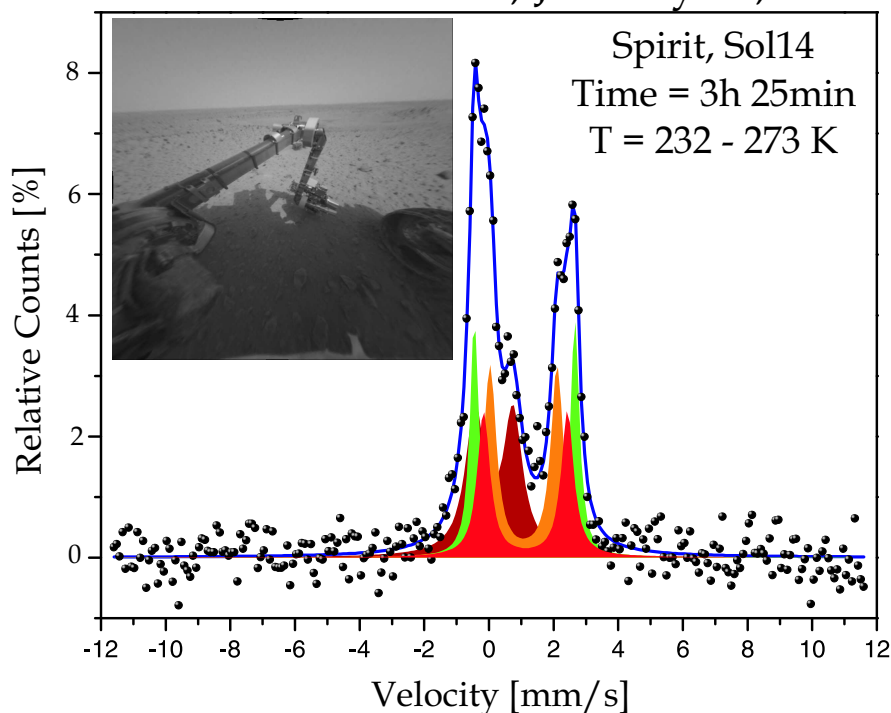


Figure 6.13: First Mössbauer spectrum measured on Mars surface. It was recorded during 3 hours and 25 minutes of sol 14 by rover *Spirit* at Gusev Crater. As supported by the fitting strategy, three Fe^{2+} doublets were applied, as well as one Fe^{3+} doublet. No magnetite signature was detected because of poor spectral statistics. In detail, a front hazcam camera image taken for this measurement is shown.

The ferrous concentration in Martian samples reported here are from 0.7 % to 0.75 % (see table 6.7). These results cannot be generalized for all Martian surface samples, even few kilometers around the landing sites.

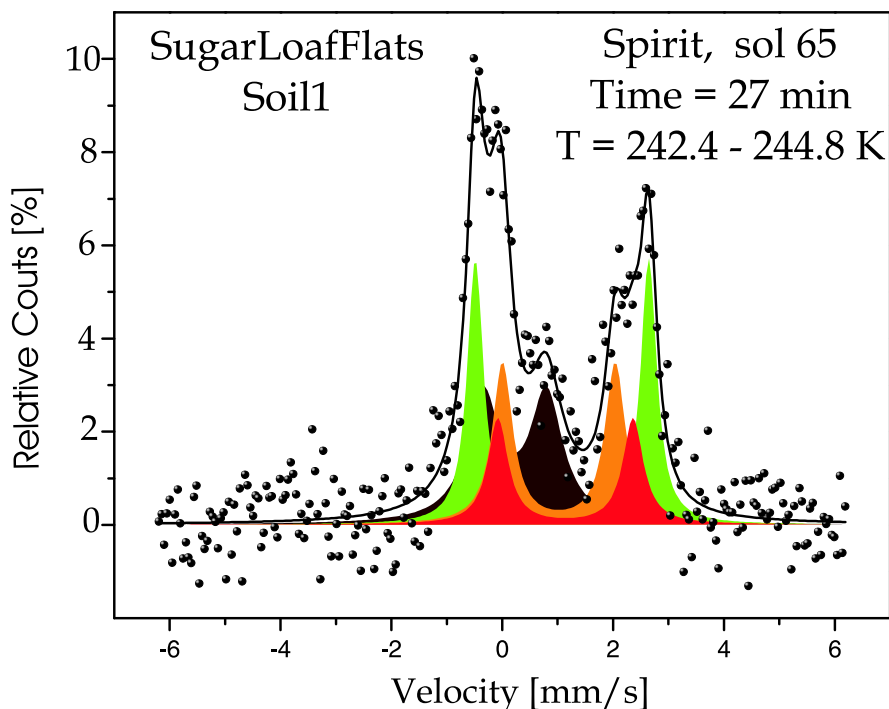


Figure 6.14: Touch and Go Mössbauer spectrum taken on a soil spot called "Sugar Loaf" during 27 minutes of sol 65 by rover *Spirit* at Gusev Crater. To improve statistical quality of this Mössbauer spectrum the velocity range was decreased.

Systematic measurements taken by the alpha particle X-ray spectrometer (APXS; e.g. [Bru 03]) chemical variations among the surface, brushed, and ground portions of Adirondack and other rocks are reported by McSween et al. [Mcs 04]. Mars soil is enriched in sulfur compared to Martian meteorites and Pathfinder rocks. According to McSween et al. [Mcs 04] estimated the composition of rock end members by an extrapolation of the sulphur concentration to 0.3 %wt., which is the average abundance of this element in Martian basaltic meteorites [Bru 03]. McSween et al. [Mcs 04] also reported that other rocks analyzed on Gusev Crater until sol 90 have chemical compositions comparable to Adirondack.

All Mössbauer spectra measured by the *Spirit* rover are characterized by three ferrous doublets (olivine and probably pyroxenes) and a ferric doublet (tentatively nanophase ferric oxide). Two magnetic sextets resulting from non-stoichiometric magnetite are observed for Adirondack rock on both

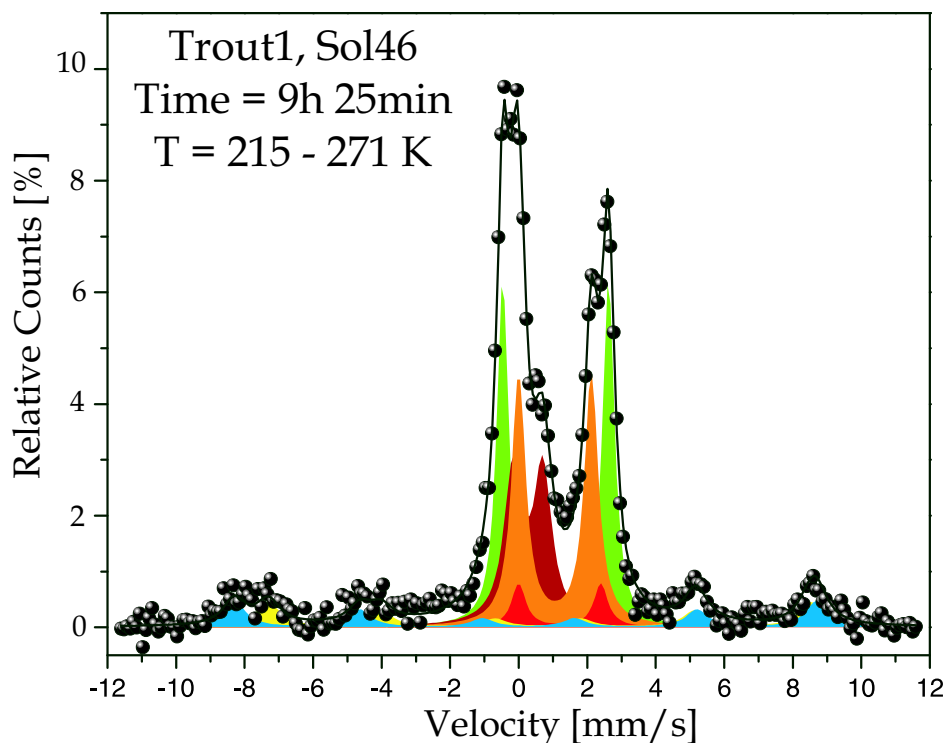


Figure 6.15: The least-squares fitted Mössbauer spectrum of soil spot called "Trout1" measured during 9 hours and 25 minutes. Magnetite sextets are taken into account in this fitting.

dusty and brushed surfaces. The $\frac{Fe^{2+}}{Fe_T}$ ratio increases from undisturbed soil to rock surfaces (table 6.7 and table 6.8). Adirondack rock has the same olivine-bearing basalt, enriched in olivine relative to soil, and the mineralogical composition of olivine in rock and soil is comparable. Iron-bearing sulfides (e.g., pyrite and pyrrhotite) and carbonates (e.g., siderite) were not conclusively detected. The mineralogy indicates that physical rather than aqueous, chemical weathering processes dominate the current mineralogical surface of Gusev Crater (e.g., [Mor 04]). The same group of ferrous minerals (olivine and pyroxenes) found on some Martian meteorites are also found in Adirondack rock and, surprisingly, in Gusev soil measurements. The relative amount of olivine varies much on Martian meteorites. The forsterite content (Fo%) in rock seems to be higher on Gusev samples than in the analyzed SNC meteorites. The Fe^{3+} in some the Martian meteorites has a quadrupole splitting of ~ 0.7 mm/s, which was not conclusively found on Martian measurements.

In table 6.7 the least-squares fitted Mössbauer parameters obtained for

Table 6.7: Least-squares fitted parameters obtained from the Mössbauer measurements taken on soil samples. Each Mössbauer spectrum was obtained from the sum of all temperature intervals.

Target Name	Site	δ † [mm/s]	Δ [mm/s]	B_{hf} [T]	Area [%]
First Soil (232 - 273 K)	Olivine	1.22	3.11		23.2
	Fe^{2+a}	1.24	2.59		20.2
	Fe^{2+b}	1.18	2.08		26.4
	Fe^{3+}	0.27	1.18		30.2
No magnetite was considered in this fitting.					
SugarLoaf1 (242 - 245 K)	Olivine	1.19	3.13		30.8
	Fe^{2+a}	1.25	2.44		15.6
	Fe^{2+b}	1.13	2.03		23.7
	Fe^{3+}	0.34	1.14		29.9
No magnetite was considered in this fitting.					
Trout1 (209 - 255 K)	Olivine	1.19	3.09		30.6
	Fe^{2+a}	1.31	2.40		4.6
	Fe^{2+b}	1.17	2.12		26.4
	Fe^{3+}	0.38	0.86		20.8
	magnetite-A	0.36	-0.08	52.7	8.7
	magnetite-B	0.69	0.05	49.1	8.9

† related to α -Fe; errors in δ and Δ are 0.02 mm/s.

the soil measurements are shown. Despite the relatively high concentration of the Fe^{3+} doublet, the spectral statistics of touch and go and short integration measurements do not allow a precise calculation of its quadrupole splitting. Because no magnetite was considered in poorer statistical fittings, the absence of the central lines of the magnetite sextets may have influenced the quadrupole splitting values of the Fe^{3+} doublet. Therefore, it cannot be associated to a different ferric phase in, for example, Trout1. Nevertheless, it can be associated to a mineral mixture of different octahedrally-ordered Fe^{3+} site rather than to a single phase.

The ferric doublet ($\delta = 0.38$ mm/s, $\Delta \sim 0.9$ mm/s) in Trout1 results from octahedrally coordinated Fe^{3+} (oct- Fe^{3+}) and is not mineralogically specific.¹³ As reported by Morris et al. [Mor 04], there are several geologically reasonable pathways to oct- Fe^{3+} doublets, including direct incorporation into silicate phases during crystallization (e.g., pyroxene and glass) and

¹³Crystalline structure was identified by the neural networks (cf. sec. 4.6.4)



<http://marsrovers.nasa.gov/gallery/press/spirit/20040119a.html>

Figure 6.16: True color image taken by the panoramic camera onboard *Spirit* shows "Adirondack" the first rover's analyzed rock. Images from the panoramic camera's blue, green and red filters (480, 530 and 600 nm filters, respectively) were combined to make this picture.

oxidative alteration (weathering) products of primary ferrous silicate phases to form certain ferric oxides. Ferric oxides include the super-paramagnetic forms of hematite and goethite, lepidocrocite, akaganéite, schwertmannite, hydronium jarosite, ferrihydrite, and the ferric pigment in palagonitic tephra. It is possible that the sulfur in Gusev Crater soils is present in part as sulfate sorbed on fine-grained ferric oxides under acidic conditions, a process reviewed by Myneni [Myn 00]. One or more of these processes may have happened around Gusev plains and are represented by their products as a broader sextet seen in all soil measurements.

The genesis of the soil at Gusev plains should be strongly associated with physical weathering. As Mars is known to have intense wind activity and there might exist different forsterite content (Fo%) in rocks at the surface, soil samples are likely to be mixtures containing different amounts of Fo% contents.

Table 6.8: Least-squares fitted Mössbauer parameters obtained from the measurement taken on dusty and brushed surfaces of Adirondack rock (figures 6.16 and 6.17).

Andirodack Surface	Site	δ [mm/s]	Δ [mm/s]	B_{hf} [T]	Area [%]
Dusty	Olivine	1.19	3.13		40.9
	Fe^{2+a}	1.26	2.43		11.0
	Fe^{2+b}	1.17	2.07		22.5
	Fe^{3+}	0.34	1.05		7.7
	magnetite-A	0.31	0.05	52.5	8.9
	magnetite-B	0.51	-0.08	49.1	9.0
Brushed	Olivine	1.20	3.08		38.4
	Fe^{2+a}	1.32	2.39		10.5
	Fe^{2+b}	1.17	2.09		29.3
	Fe^{3+}	0.33	1.05		7.9
	magnetite-A	0.29	0.07	52.5	5.2
	magnetite-B	0.66	-0.13	49.1	8.7

Note: Δ values deviate from those obtained from distribution (cf. fig. 6.12); $\Delta_1 = 1.96$ mm/s; $\Delta_2 = 2.27$ mm/s, and $\Delta_3 = 3.10$ mm/s).

[†] Related to α -Fe; errors in δ and Δ are 0.02 mm/s, and 0.5 % in area.

The ferrous doublet with $\delta \sim 1.2$ mm/s and $\Delta \sim 3.1$ mm/s is assigned to the mineral olivine with a high degree of confidence; because, for this common rock-forming minerals, this value of Δ is virtually mineralogically specific for olivine [Mor 04], as also identified by the implemented neural network.¹⁴ The presence of olivine is not unexpected, on the basis of observations from Martian orbit and petrographic and Mössbauer studies of Martian meteorites. The quadrupole splitting values for olivines decrease as the temperature increases over Martian temperature range. The quadrupole splitting ($\Delta = 3.08$ mm/s for dusty to $\Delta = 3.13$ mm/s for brushed) shows that Adirondack olivine has an intermediate composition.¹⁵ This quadrupole splitting value, the results of the figure 4.9, resulting from 167 published Mössbauer parameters recorded at room temperature, and the results reported by Morris et al. [Mor 04] indicate the composition of Adirondack olivine smaller than $\sim Fo_{90}$. Based on chemical analysis, the Adirondack rock is olivine normative ($\sim Fo_{50-60}$) [Mcs 04]. Mini-TES spectra of Adirondack and other

¹⁴Check sec. 4.6.1.

¹⁵Cf. fig. 4.8 and 4.9.

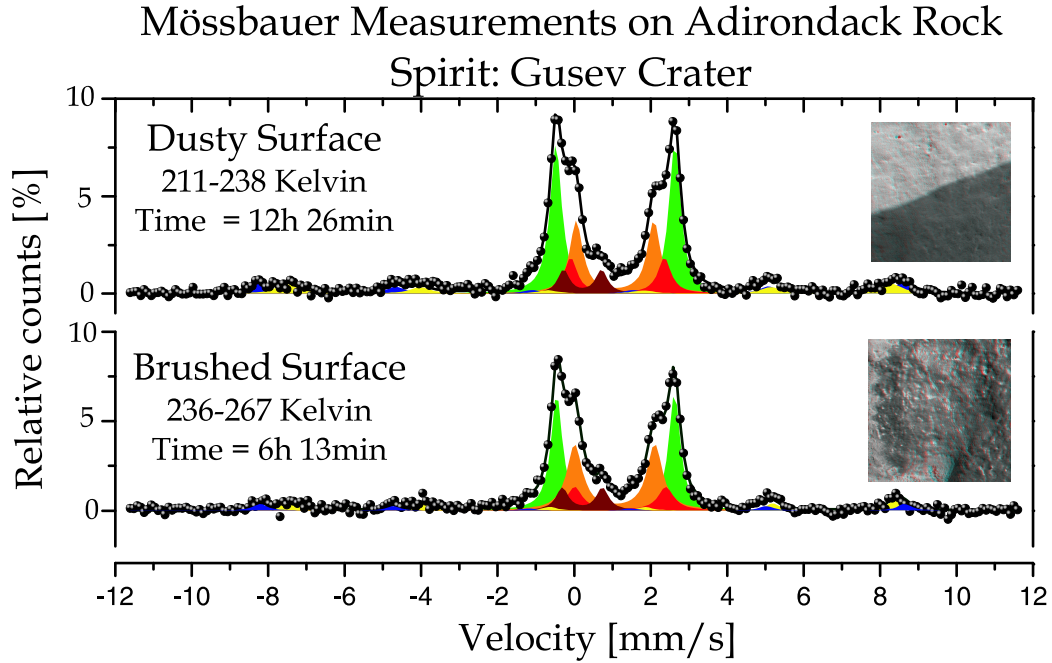


Figure 6.17: Mössbauer spectra measured on the dusty and brushed Adirondack surfaces. Microscopic images (3 cm x 3 cm) are shown at the right side of the spectra. All temperature accumulation are added for each Mössbauer spectrum. The least-squares Mössbauer parameters are given in table 6.8. Compare above figures 6.11 and 6.12 where the ferrous contribution is fitted using three doublets associated with olivine and pyroxenes sites (cf. table 6.8).

rocks on Gusev Crater suggest (Fe_{35-60}).

The Mössbauer spectra of many martian rocks and soils are characterized by a two sextet pattern whose peaks progressively overlap from low to high velocity. This pattern is characteristic of magnetite, where the sextets are derived from the octahedral (Fe^{2+} , Fe^{3+}) and tetrahedral (Fe^{3+}) sites. Magnetite has not been reported in the Mössbauer spectrum of any bulk martian meteorite, although Vieira [Vie 86] describes a magnetite spectrum from a mineral sample from Nakhla and in the believed fossilized structures of ALH84001 (e.g., [Gol 04] and references therein). The intensity ratio of octahedral to tetrahedral sites in stoichiometric magnetite is $\sim 1.9 : 1$. For Gusev magnetite the ratio is about the 1:1, so it is non-stoichiometric, resulting from oxidation and/or substitutional impurities (e.g., Ti). Nevertheless, there is a real lack of unequivocal proof of isomorphic substitution in magnetite. The Mössbauer experiment for such purpose has to be performed longer to increase the spectral statistics in a high magnetite contact

target. Nevertheless, there will be no guarantee this particular sample has non-stoichiometry.

The mineralogical composition of the strongly magnetic component in Martian surface materials has been investigated since Viking with permanent magnets on landers [Har 79]. At least at Gusev Crater, the Mössbauer results point to non-stoichiometric magnetite as that component. The phase is present in rocks and in soils. Considering the chemical composition presented by McSween et al. [Mcs 04] and the relative spectral area shown in table 6.7 and in table 6.8, the magnetite weight concentration will be of few percentages (~ 2 %wt.).

Martian meteorites and Adirondack ferrous components are similar. The magnetite identified in Adirondack and in Martian soils were not detected in the SNC meteorites analyzed here. Also, the quadrupole splitting obtained for all SNC meteorites points to a poor Fo%.

Until sol 65 no clear trace of crystalline hematite, maghemite, jarosite, and goethite was detected by MIMOS II measurements. As suggested earlier in this thesis,¹⁶ clay-rich aqueous sediments on Earth frequently hold high concentration of biogenic organic matter. Therefore, clay materials such as smectites (e.g. the ones found in Chinese wall paintings reported in sec. 5.3.4) are candidates to hold evidence for past Martian life. Nevertheless, until sol 65 of operations in Gusev Crater, iron-bearing smectites were not clearly detected by MIMOS II observations.

In resume, reported Martian mineralogy of rocks and soils from Gusev Crater are similar. Its iron-bearing components are forsteritic olivine, pyroxene, and magnetite. An octahedrally ordered ferric doublet, possibly oxide, hydroxide or oxide-hydroxide, not mineralogic specific, was found. Physical weathering was the major process on Gusev surface.

¹⁶See above chap. 1 and passim on sec. 6.3.

Chapter 7

Summary, conclusions and outlook

7.1 Summary of results

The miniaturization of a Mössbauer spectrometer (MIMOS II) was initiated in the early nineties by Prof. Dr. Egbert Kankeleit at the Technical University of Darmstadt and was further developed by Dr. Göstar Klingelhöfer and co-workers at the Institute of Inorganic and Analytical Chemistry of the Johannes Gutenberg University in Mainz. The instrument meets the requirements for space applications as low power consumption, small mass and volume, and mechanical robustness. The velocity calibration of the miniaturized drive, the energy detector calibration, temperature dependent measurements, internal and external reference samples, field tests, health checks were planned and performed by the MIMOS II Project Group in Mainz and are concisely presented here. Resulting from its constructive and operational characteristics, the instrument, developed originally for space missions, offers also many outdoor terrestrial applications as exemplified in the present thesis.

Mars mineralogy was not directly measured in situ before the use of MIMOS II installed at the *Spirit* and *Opportunity* rovers. A data bank containing Mössbauer parameters of all possible minerals containing iron and one or more chemical elements found on Mars surface by previously landed missions was compiled. More than 400 studied iron-bearing minerals (over 140 candidates Martian minerals) were already studied by ^{57}Fe Mössbauer spectroscopy. A database containing the Mössbauer parameters classified by each iron-bearing mineral reported in the literature for given temperatures from liquid nitrogen (77 K) to room temperature (298 K) was compiled. A

search engine in SQL database searches for exact information. Since small differences in the studied samples result in small deviations of the Mössbauer parameters, another method for quick match of the measured and the stored parameters was developed. A search engine based on artificial neural networks was successfully implemented and tested, and was used during real-time Martian surface operations to identify mineral phases and crystalline structures from Mössbauer parameters. From the Mössbauer parameters of the studied phases can be identified.

The data analysis of a Mössbauer spectrum can be time-consuming. To overcome this problem a fitting routine based on genetic algorithm was implemented. This method allows the fitting of a Mössbauer spectrum from a vague input data set, resulting in a fast convergence of the fitted parameters. The Mössbauer parameters are obtained from this fitting process. The fitting routine was controlled using fuzzy logic (e.g., setting the number of iterations for each Mössbauer parameter).

The database, the genetic algorithm controlled by fuzzy logic and the artificial neural network became useful tools for the Mössbauer data analysis, in particular for those not familiar with Mössbauer spectroscopy on minerals. Indeed, it is also an effort to meet the major difficulties with which the unexperienced spectroscopist will find himself confronted in this data analysis.

The data analysis tools associated with the portable Mössbauer spectrometer open new possibilities of outdoor applications. Some of them were exploited in this thesis like the pigment characterization of archaeological artifacts and in situ air pollution studies. The usefulness of MIMOS II goes further than these examples, and it is also proposed here as an additional method for checking the authenticity of ancient archaeological pieces, and identifying applied materials in the manufacture artifact processes.

To demonstrate the capability of MIMOS II to characterize extraterrestrial materials before the launch of the mission to Mars, a suite of chondrite, metallic, and Martian meteorites were measured.

The first-ever Mössbauer experiment performed on the surface of another planet was received from the MIMOS II spectrometer aboard *Spirit* rover on January 17, 2004 and was presented here. It was recorded by the MIMOS II Consortium headed by Dr. Göstar Klingelhöfer and the Athena Science Team at the Jet Propulsion Laboratory, California Institute of Technology in Pasadena, California. In addition to this Mössbauer spectrum, the spectra of

two soils and two measurements on Adirondack rock were taken by MIMOS II onboard *Spirit* at Gusev Crater and are presented and discussed in the thesis.

Martian mineralogy in Gusev rock and soils reported in this thesis are dominated by forsteritic olivine, pyroxene, magnetite, and by an octahedrally ordered ferric doublet which was not conclusively identified. Based on the reported data, it is concluded that physical weathering was an important alteration process at Gusev plains.

7.2 Conclusions and outlook

As future work an update of the compiled data base with new published data, including Ph.D. theses and research reports is proposed. The use of evolutionary algorithms is an alternative for the genetic algorithm in the fitting procedure.

Many industrial applications such as quality control of iron-based products (e.g., iron ore pellets, steel, magnetic tapes) can be explored locally using MIMOS II as a mobile spectrometer.

The results obtained with metallic and iron-bearing minerals on archaeological artifacts are interesting and further characterization of such samples is encouraged.

As future work a systematic analysis of 6.4 and 14.4 keV Mössbauer spectra recorded in Martian samples by *Spirit* and *Opportunity* rovers is proposed, associated with laboratory calibration with an engineering model of MIMOS II. An overview on Martian soil and rock diversity should be done.

A systematic study of the olivine mineral group will be needed for better understanding the Mössbauer data obtained on Mars surface. This includes a whole series of natural and synthetic olivines; from fayalite to forsterite, studied within the Martian temperature range.

Chemical weathering of basalts in the laboratory under controlled conditions should be investigated in detail for better understanding of Martian mineralogy and, therefore, the surface evolution.

It is important to analyze the Fe^{3+} doublet variety (e.g., the isomer

shift, quadrupole splitting, line widths, relative area, possible relationship with chemistry) from sample to sample, and for each temperature window of Martian measurements. This ferric phase might be related to weathering and other processes than the surface material genesis process itself and should be carefully investigated.

It can be concluded that the space technologies can be applied to many outdoor terrestrial applications. Some of them require a friendly data analysis system. The success of a space mission depends on many factors, and if all requirements are met, still luck remains as an important factor. The use of these payloads on terrestrial problems in industry, environmental sciences, and archaeology can start even before the mission launch.

Bibliography

- [Agr 92] D. G. Agresti, R. V. Morris, E. L. Wills, T. D. Shelfer, M. M. Pimperl, M. Shen, B. C. Clark, and B. D. Ramsey, *Hyp. Interact.* 72(1992)285.
- [Aho 97] H. Ahonen, P. A. de Souza Jr., and V. K. Garg, *Nucl. Instrum. Meth. Phys. Res.* B124(1997)633.
- [Alf 62] V. P. Alfimenkov, Yu. M. Ostanevich, T. Ruskov, A. V. Strelkov, F. L. Shapiro, and W. K. Yen, *Soviet Physics - J.E.T.P.* 15(1962)713.
- [Ara 70] F. Aramu and V. Maxia, *Nucl. Instrum. Meth.* 80(1970)35.
- [Arv 98] R. E. Arvidson, . Acton, D. Blaney, J. Bowman, S. Kim, G. Klingelhöfer, J. Marshall, C. Niebur, J. Plescia, R. S. Saunders, and C. T. Ulmer, *J. Geophys. Res.* 103(E10)(1998)22671.
- [Arv 02] R. E. Arvidson, *J. Geophys. Res.* 107,E11(2002)1.
- [Axt 67] R. C. Axtman, Y. Hazony, and J. W. Hurley Jr., *Chem. Phys.* 52(1967)3309.
- [Axt 68] R. C. Axtman, Y. Hazony, and J. W. Hurley Jr., *Chem. Phys. Lett* 2(1968)673.
- [Ban 72] G. M. Bancroft and R. H. Platt, *Adv. Inorg. Chem. Radiochem.* 15(1972)59.
- [Bea 54] H. J. Beattie and R. M. Brissey, *Anal. Chem.* 36(1954)36.
- [Ban 83] A. Banin and L. Margulies, *Nature* 305(1983)523.
- [Ban 85] A. Banin, L. Margulies, and Y. Chen, *J. Geophys. Res.* 90(1985)C771.

- [Bla 85] N. Blaes, H. Fischer, and U. Gonser, Nucl. Instrum. Meth. Phys. Res. B9(1985)201.
- [Bra 65] P. R. Brady, J. F. Duncan, and K. F. Mok, Proc. Roy. Soc. A287(1965)343.
- [Bur 72] K. Burger, Inorg. Chem. Acta Rev. 6(1972)31.
- [Bur 86] R. G. Burns, Nature 320(1986)55.
- [Bur 90] R. G. Burns and T. C. Solderg. In *Spectroscopy characterization of minerals and their surfaces*; L. M. Coyne, S. W. S. McKeever, D. F. Blake eds. (Am. Chem. Soc., Washington, 1990).
- [Bur 93] R. G. Burns. In *Remote geochemical elemental analysis and mineralogical composition*, Chap. 14; C. M. Pieters and P. A. J. Englert eds. (Cambridge Univ. Press, Cambridge, 1993).
- [Bur 94] R. G. Burns, Hyp. Interact. 91(1994)739.
- [Bur 87] R. G. Burns, J. Geophys. Res. E92(1987)570.
- [Bru 03] J. Brückner, G. Dreibus, R. Rieder, and H. Wänke, J. Geophys. Res. 108, E12(2003)8094.
- [Cho 95] J. C. Chow, J. Air Waste Management Assoc. 45,5(1995)320.
- [Cla 77] B. C. Clark, A. K. Baird, H. J. Rose Jr., P. Toulmin III, K. Keil, A. J. Castro, W. C. Kelliher, C. D. Rowe, and P. H. Evans, Science 194(1977)1283.
- [Cla 78] B. C. Clark, Icarus 34(1978)645.
- [Cla 79] B. C. Clark and A. K. Baird, J. Geophys. Res. 84(1979)8395.
- [Cla 81] B. C. Clark and D. C. van Hart, Icarus 45(1981)370.
- [Cla 82] B. C. Clark, A. K. Baird, R. J. Weldon, D. M. Tsusaki, L. Schnabel, and M. P. Canelaria, J. Geophys. Res. 87(1982)10059.
- [Cor 68] C. W. Correns. In *Einführung in die Mineralogie: Kristallographie und Petrologie*, (Springer-Verlag, Berlin, 1968).
- [Cor 03] R. M. Cornell and U. Schwertmann, *The iron oxides: structure, properties, reactions, occurrences and uses*, (Wilhey-VCH, Weinheim, 2003).

- [Dan 79] J. Danon, R. B. Scorzelli, I. S. Azevedo, W. Curvello, J. F. Albertsen, and J. M. Knudsen, *Nature* 277(1979)283.
- [Des 97] P. A. de Souza Jr., J. D. Fabris, W. N. Mussel, and V. K. Garg, *Hyper. Interact. (C)*2(1997)47.
- [Des 98] P. A. de Souza Jr., *Hyper. Interact.* 113(1998)47.
- [Des 98b] P. A. de Souza Jr., O. D. Rodrigues, T. Morimoto, and V. K. Garg, *Hyp. Interact.* 112(1998)133.
- [Des 99] P. A. de Souza Jr., *Lab. Rob. Autom.* 11(1999)3.
- [Des 99b] P. A. de Souza Jr. and V. K. Garg. In: *Mössbauer spectroscopy in material science*, NATO Science Series, 3. High technology, Vol. 66(1999)359.
- [Des 00] P. A. de Souza Jr., R. S. Queiroz, T. Morimoto, A. F. Guimarães, and V. K. Garg, *J. Radional. Nucl. Chem.* 246(2000)85.
- [Des 01a] P. A. de Souza Jr., G. Klingelhöfer, B. Bernhardt, C. Schröder, T. Morimoto, and P. Gütlich, 94th Annual Meeting and Exhibition of Air and Waste Management Association, Orlando, FL, 2001, Sect. AB-2D, 569.
- [Des 01b] P. A. de Souza Jr. and G. Klingelhöfer, *Cz. J. Phys.* 51, 7(2001)651.
- [Des 01c] P. A. de Souza Jr., G. Klingelhöfer, and T. Morimoto, *Hyp. Interact. (C)*5(2001)487.
- [Des 02] P. A. de Souza Jr., V. K. Garg, G. Klingelhöfer, R. Gellert, and P. Gütlich, *Hyp. Interact.* 139(2002)705.
- [Des 03a] P. A. de Souza Jr., R. V. Morris, and G. Klingelhöfer, Sixth International Conference on Mars, Abs. # 3143 Houston, TX, 2003.
- [Des 03b] P. A. de Souza Jr., B. Bernhardt, G. Klingelhöfer, and P. Gütlich, *Hyp. Interact.* 151(2003)125.
- [Dya 84] M. D. Dyar, *Am. Mineral.* 69(1984)1127.
- [Dzy 58] I. Dzyaloshinsky, *J. Chem. Solids* 14(1958)241.

- [Evl 93] E. N. Evlanov, V. A. Frolov, O. F. Prilutski, A. M. Rodin, G. V. Veselova, and G. Klingelhöfer, *Lunar and Planet. Sci.* (1993)459.
- [Fri 89] S. M. Fries, J. Crummenauer, U. Gonser, P. Schaff, and C. L. Chien, *Hyp. Inter.* 45(1989)301.
- [Gal 89] J. Galazkha-Friedman and J. Juchniewicz, *Martian Mössbauer Spectrometer MarMös, project proposal*, Space Research Center (Polish Academy of Sciences, Warsaw, 1989).
- [Gel 04] R. Gellert, R. Rieder, R. C. Anderson, J. Brückner, B. C. Clark, G. Dreibus, T. Economou, G. Klingelhöfer, G. W. Lugmair, D. W. Ming, S. W. Squyres, C. d'Uston, H. Wänke, A. Yen, and J. Zipfel, *Science* 305(2004)829.
- [Gol 89] D. E. Goldberg, *Genetic algorithms in search, optimization, and machine learning*, (Addison-Wesley, Reading, 1989).
- [Gol 63] V. I. Goldanskii, E. F. Makarov, and V. V. Kharapov, *Phys. Lett.* 3(1963)344.
- [Gol 04] D. C. Golden, D. W. Ming, R. V. Morris, A. J. Brearley, H. V. Lauer Jr., A. H. Treiman, M. E. Zolensky, C. S. Schwandt, G. E. Lofgren, and G. A. McKay, *Evidence for exclusively inorganic formation of magnetite in Martian meteorite ALH84001*, *Am. Mineral.* (2004) in press.
- [Gol 03] M. P. Golombek, J. A. Grant, T. J. Parker, D. M. Kass, J. A. Crisp, S. W. Squyres, A. F. C. Haldemann, M. Adler, W. J. Lee, N. T. Bridges, R. E. Arvidson, M. H. Carr, R. L. Kirk, P. C. Knocke, P. B. Roncoli, C. M. Weitz, J. T. Schofield, R. M. Zurek, P. R. Christensen, R. L. Fergason, F. S. Anderson, and J. W. Rice Jr., *J. Geophys. Res.* 108, E12(2003)1029.
- [Goo 78] J. L. Gooding, *Icarus* 33(1978)483.
- [Goo 78b] J. L. Gooding, S. J. Wentworth, and M. E. Zolensky, *Geochim. Cosmochim. Acta.* 52(1978)909.
- [Gon 86] U. Gonser. *Mössbauer spectroscopy*. U. Gonser ed. In: *Microscopic methods in metals*, Chap. 13 (Springer Verlag, Berlin-Heidelberg-New York, 1986).

- [Gor 03] S. Gorevan, T. Myrick, K. Davis, J. J. Chau, P. Bartlett, S. Mukherjee, R. Anderson, S. W. Squyres, R. E. Arvidson, M. B. Madsen, P. Bertelsen, W. Goetz, C. S. Binau, and L. Richter, *J. Geophys. Res.* 108, E12(2003)8068.
- [Gra 66] R. W. Grant. In *Mössbauer effect methodology*, I. J. Gruvermann ed., Vol. 2 (Plenum Press, New York, 1966).
- [Gra 82] E. D. Grave, L. H. Bowen and S. B. Weed, *J. Mag. Mater.* 27(1982)98.
- [Gui 87] E. A. Guinness, R. E. Arvidson, M. A. Dale-Bannister, R. B. Singer, and E. A. Bruckenthal, *J. Geophys. Res.* E92(1987)E575.
- [Gum 88] A. W. Gummer, *Nucl. Instrum. Meth. Phys. Res.* B34(1988)224.
- [Güt 78] P. Gütlich, R. Link, and A. X. Trautwein, *Mössbauer spectroscopy and transition metal chemistry*, (Springer-Verlag, Heidelberg, 1978).
- [Har 79] R. B. Hargraves, D. W. Collinson, R. E. Arvidson, and P. M. Gates, *J. Geophys. Res.* 84(1979)8379.
- [Haz 68] Y. Hazony, R. C. Axtman, and J. W. Hurley, Jr., *Chem. Phys. Lett.* 2(1968)440.
- [Hel 93] P. Held, R. Teucher, G. Klingelhöfer, J. Foh, H. Jäger, and E. Kankeleit, *Lunar Planet. Sci.*, XXIV (1993)633.
- [Hel 97] P. Held, *MIMOS II: Ein miniaturisiertes Mößsbauerspektrometer in Rückstreugeometrie zur mineralogischen Analyse der Marsoberfläche*. Diss., Institut für Kernphysik, TH Darmstadt (1997).
- [Hec 87] R. Hecht-Nielsen, *Appl. Opt.* 26(1987)4979.
- [Höl 89] A. R. Hölzel, *Systematics of minerals: data, literature, crystallography, element register, petrography* (Privately Printed, Mainz, 1989).
- [Hug 82] R. L. Huguenin, *J. Geophys. Res.* 87(1982)10069.
- [Hol 97] T. J. B. Holland and S. A. T. Redfern, *Mineral. Mag.* 61(1997)65.
- [Hub 79] J. S. Hubbard, *J. Mol. Evol.* 14(1979)211.

- [Jor 69] C. K. Jorgensen, *Oxidation number and oxidation States*, (Springer, New York, 1969).
- [Kan 64] E. Kankeleit, *Rev. Sci. Instrum.* 35(1964)194.
- [Kan 75] E. Kankeleit, *Proc. Int. Conf. on Mössbauer Spectroscopy*, Univ. of Krakow, Krakow, Poland, 1975.
- [Kar 63] S. V. Karyagin, *Dokl. Akad. Nauk. SSSR* 148(1963)1102.
- [Kau 00] W. Kautek and C. Maywald-Pitellos, *J. Cul. Herit.* 1(2000)1.
- [Kli 92] G. Klingelhöfer, U. Imkeller, E. Kankeleit, and B. Stahl, *Hyp. Interact.* 71(1992)1445.
- [Kli 95] G. Klingelhöfer, P. Held, R. Teucher, F. Schlichting, J. Foh, and E. Kankeleit, *Hyp. Interact.* 95(1995)305.
- [Kli 02] G. Klingelhöfer, R. V. Morris, B. Bernhardt, J. Foh, U. Bonnes, D. Rodionov, P. A. de Souza Jr., C. Schröder, R. Gellert, S. Kane, P. Gütlich, and E. Kankeleit, *Hyp. Interact.* 144(2002)371.
- [Kli 02b] G. Klingelhöfer, G. M. da Costa, G. M. Porus, and B. Bernhardt, *Hyp. Interact.* C5(2002)423.
- [Kli 03] G. Klingelhöfer, R. V. Morris, B. Bernhardt, D. Radionov, P. A. de Souza Jr., S. W. Squyres, J. Foh, E. Kankeleit, U. Bonnes, R. Gellert, Ch. Schröder, S. Linkin, E. Evlanov, B. Zubkov, and O. Prilutski, *J. Geophys. Res.* 108, E12(2003)1029.
- [Kli 04] G. Klingelhöfer, R. V. Morris, B. Bernhardt, C. Schröder, D. S. Rodionov, P. A. de Souza Jr., A. Yen, R. Gellert, E. N. Evlanov, B. Zubkov, J. Foh, U. Bonnes, E. Kankeleit, P. Gütlich, D. W. Ming, F. Renz, T. Wdowiak, S. W. Squyres, and R. E. Arvidson, *Jarosite and Hematite at Meridiani Planum from Opportunity's Mössbauer Spectrometer*, Dec. 3 (2004) *Science*, in Press.
- [Kei 80] K. Keil, *Brazilian stone meteorites*, (Univ. New Mexico Press, 1980).
- [Koh 88] T. Kohonen, *Self-organization and Associative Memory*, 3rd. ed. (Springer-Verlag, Berlin, 1988).

- [Knu 92] J. M. Knudsen, M. B. Madsen, M. Olsen, L. Vistisen, C. B. Koch, S. Mørup, E. Kankleit, G. Klingelhöfer, E. N. Evlanov, V. N. Khromov, L. M. Mukhin, O. F. Prilutskii, B. Zubkov, G. V. Smirnov, and J. Juchniewicz, *Hyp. Interact.* 68(1992)83.
- [Kün 69] W. Kündig and R. S. Hargrove, *Sol. Stat. Comm.* 7(1969)223.
- [Kuz 03] E. Kuzmann, S. Nagy, and A. Vèrtes, *Pure Appl. Chem.* 75, 6(2003)801.
- [Lew 79] D. G. Lewis and U. Schwertmann, *Clay Min.* 14(1979)195.
- [Lod 98] K. Lodders and B. Fegley Jr., *The planetary scientist's companion*, (Oxford Press Univ., 1998).
- [Mar 94] R. J. Mark II and R. J. Mark, eds., *Fuzzy logic technology and applications*, IEEE Technology Update Series, (IEEE Press, N. Y., 1994).
- [Mar 92] *Mars* H. H. Kiefer, B. M. Jakosky, C. W. Snyder, and M. S. Matthews, eds., Space Science Series, (The University of Arizona Press, Tucson, 1992).
- [Mat 89] Y. Matsumoto, N. Fujino, and S. Nasu, *ISIJ Int.* 29, 11(1989)973.
- [Mck 96] D. S. McKay, E. K. Gibson Jr., K. L. Thomas-Keprta, H. Vali, C. S. Romanek, S. J. Clemett, X. D. F. Chillier, C. R. Maechling, and R. N. Zare, *Science* 273(1996)924.
- [Mcm 00] P. H. McMurry, *Atmos. Environ.* 34(2000)1959.
- [Mcs 80] H. Y. McSween Jr. and E. M. Stolper, *Sci. Amer.* 242(1980)54.
- [Mcs 94] H. Y. McSween Jr., *Meteoritics* 29(1994)757.
- [Mcs 00] H. Y. McSween Jr., In *Meteorites and their parent planets*, 2nd. ed. (Cambridge University Press, Cambridge, 2000).
- [Mcs 04] H. Y. McSween Jr., R. E. Arvidson, J. F. Bell III, D. Blaney, N. A. Cabrol, P. R. Christensen, B. C. Clark, J. Crisp, L. S. Crumpler, D. J. Des Marais, J. D. Farmer, R. Gellert, A. Ghosh, S. Gorevan, T. Graff, J. Grant, L. A. Haskin, K. E. Herkenhoff, J. R. Johnson, B. L. Joliff, G. Klingelhofer, A. T. Knudson, S. McLennan, K. A. Milam, J. E. Moersch, R. V. Morris, R. Rieder, S. W. Ruff, P. A. de Souza Jr., S. W. Squyres, H. Wänke, A. Wang, M. B. Wyatt, A. Yen, and J. Zipfel, *Science* 305(2004)842.

- [Mit 92] S. Mitra, In *Applied Mössbauer spectroscopy: theory and Practice for geochemists and archeologists*, (Pergamon Press, Oxford, 1992).
- [Mør 83] S. Mørup and H. Tøpsoe, *Magnetic and electronic properties of microcrystals of Fe_2O_3* , J. Mag. Mag. Mat. 31(1983)953.
- [Mor 85] R. V. Morris, H. V. Lauer, Jr., C. A. Lawson, E. K. Gibson Jr., G. A. Nace, and C. Stewart, J. Geophys. Res. 90(1985)3126.
- [Mor 88] R. V. Morris, D. G. Agresti, T. D. Shelfer, and T. J. Wdowiak, *Mössbauer spectroscopy for mineralogical analysis on planetary surfaces*, 1988. Proc. SAAP Instrument Technology Workshop, Sample Acquisition and Anal. Program, Houston, Texas, 1988.
- [Mor 00] R. V. Morris, D. C. Golden, J. F. Bell III, T. D. Shelfer, A. C. Scheinost, N. W. Hinman, G. Furniss, S. A. Mertzman, J. L. Bishop, D. W. Ming, C. C. Allen, and D. T. Britt, J. Geophys. Res. 105(2000)1817.
- [Mor 01] R. V. Morris, T. G. Graff, T. D. Shelfer, and J. F. Bell III, Abs. # 1912, Lunar Planet. Sci. [CD-ROM], XXXII, 2001.
- [Mor 04] R. V. Morris, G. Klingelhöfer, B. Bernhardt, C. Schröder, D. S. Rodionov, P. A. de Souza Jr., A. Yen, R. Gellert, E. N. Evlanov, J. Foh, E. Kankleit, P. Gütlich, D. W. Ming, F. Renz, T. Wdowiak, S. W. Squyres, and R. E. Arvidson, Science 305(2004)833.
- [Mös 58a] R. L. Mössbauer, Z. Physik 151(1958)124.
- [Mös 58b] R. L. Mössbauer, Naturwissenschaften 45(1958)538.
- [Mös 62] R. L. Mössbauer, Science 137(1962)731.
- [Mös 00] R. L. Mössbauer, Hyp. Interact. 126(2000)1.
- [Myn 00] S. C. B. Myneni, *X-ray and vibrational spectroscopy of sulfate in geologic materials*. In: Rev. Mineral. Sulfate Minerals: Crystallography, Geochemistry, and Environmental Significance, ed. C. N. Alpers, J. L. Jambor, and D. K. Nordstrom, Vol. 40(2000)113-172.
- [Pau 00] H. Paulsen, R. Linder, F. Wagner, H. Winkler, S. J. Pöppel, and A. X. Trautwein, Hyp. Interact. 126(2000)421.

- [Pri 90] O. Prilutskii, Internal report from Minsk, (Space Research Institute (IKI), Moscow, 1990).
- [Ras 74] S. D. Rasberry and K. F. J. Heinrich, *Anal. Chem.* 46(1974)81.
- [Rie 97] R. Rieder, T. Economou, H. Wänke, A. Turkevich, J. Crisp, J. Brückner, G. Dreibus, and H. Y. McSween Jr., *Science* 278(1997)1771.
- [Rie 69] R. Riesenman, J. Steger, and E. Kostiner, *Nucl. Instrum. Meth.* 72(1969)109.
- [Rgz 03] Römisches-Germanisches Zentral Muzeum, Chinese excavation report (- Mainz, 2003).
- [Sal 94] E. O. T. Salles, P. A. de Souza Jr., and V. K. Garg, *Nucl. Instrum. Meth. Phys. Res. B*94(1994)499.
- [Sal 95] E. O. T. Salles, P. A. de Souza Jr., and V. K. Garg, *J. Radioanal. Nucl. Chem.* 190(1995)439.
- [San 92] E. Sánchez-Sinencio and C. G. Y. Lau, Eds. *Artificial neural network hardware - Paradigms, applications and implementation*, (IEEE Press, New York, 1992).
- [Sch 80] H. P. Schramm and B. Hering, *Historische Materialien und Möglichkeiten ihrer Identifizierung* (-, Dresden, 1980).
- [Sch 01] C. Schröder, *Optimierung der Nachweis eigenschaften des miniaturisierten Mössbauer-Spektrometers MIMOS-II und Messungen an Mars-Analog-Proben*, diploma-arbeite, Johannes Gutenberg Universität, Mainz, 2001.
- [Sch 91] U. Schwertmann and R. M. Cornell, In *The iron oxides in the laboratory: preparation and characterization*, (VCH, New York, 1991).
- [Sch 92] G. Schatz and A. Weidinger, *Nucleare Festkörperphysik*, (Teubner Studienbücher, Stuttgart, 1992).
- [Shi 66] T. Shiraiwa and N. Fujino, *Jap. J. Appl. Phys.* 5(1966)886.
- [Sil 04] M. M. da Silva, *Fatores influenciadores na determinação de ferro total em minério de ferro por espectroscopia de fluorescência de raios-X*, M.Sc. Diss., Universidade Federal de Ouro Preto, Brazil (2004).

- [Sim 96] P. K. Simpson ed., *Neural networks: theory, technology and applications*, (IEEE Press, New York, 1996).
- [Sim 02] M. R. Sims, D. Pullan, G. W. Fraser, S. Whitehead, J. Sykes, J. Holt, G. I. Butcher, N. Nelms, J. Dowson, D. Ross, C. Bicknell, M. Crocker, B. Favill, A. A. Wells, L. Richter, H. Kochan, H. Hamacher, L. Ratke, A. D. Griffiths, A. J. Coates, P. N. Phillips, A. Senior, J. C. Zarnecki, M. C. Towner, M. Leese, M. Patel, C. Wilson, N. Thomas, S. Hviid, J.-C. Josset, G. Klingelhofer, B. Bernhardt, P. van Duijn, G. Sims, and K. L. Yung, Proc. SPIE Int. Soc. Opt. Eng. 4859(2002)32.
- [Sin 85] R. B. Singer, Adv. Space Res. 5(1985)59.
- [Sod 78] L. A. Soderblom and D. B. Wenner, Icarus 34(1978)622.
- [Sou 93] M. N. Souza, M. A. Figueira, and M. S. da Costa, Nuc. Instrum. Meth. Phys. Res. B 73(1993)95.
- [Ste 86] J. G. Stevens and W. Zhu, Hyp. Interact. 29(1986)1149.
- [Squ 03] S. W. Squyres, R. E. Arvidson, E. T. Baumgartner, J. F. Bell III, P. R. Christensen, S. Gorevan, K. E. Herkenhoff, G. Klingelhöfer, M. Bo Madsen, R. V. Morris, R. Rieder, and R. A. Romero, J. Geophys. Res. 108, E12(2003)8062.
- [Ste 82] J. G. Stevens, H. Pollak, L. Zhe, V. E. Stevens, R. M. White, and J. L. Gibson, eds. *Mineral data* (MEDC, Univ. North Carolina, Asheville, 1982).
- [Teu 94] R. Teucher, *Miniaturisierter Mössbauer antrieb*, diploma-arbeite, Inst. Nucl. Phys., TH Darmstadt, 1994.
- [Tho 02] K. L. Thomas-Keprta, S. J. Clemett, D. A. Bazylinski, J. L. Kirschvink, D. S. McKay, S. J. Wentworth, H. Vali, E. K. Gibson, and C. S. Romanek, Appl. Environ. Microb. 68(2002)3663.
- [Too 77] O. B. Toon, J. B. Pollack, and C. Sagan, Icarus 30(1977)663.
- [Ulr 73] K. Ulrich, Archäologisches Korrespondenzblatt 3(1973)313.
- [Van 01] R. E. Vandenberghe, E. van San, E. de Grave, and G. M. da Costa, Cz. J. Phys. 51, 7(2001)663.
- [Ver 41] E. J. W. Verwey and P. W. Haaymann, Physica 8(1941)979.

- [Vie 86] V. W. A. Vieira, T. V. V. Costa, H. G. Jensen, J. M. Knudsen, M. Olsen, and L. Vistisen, *Physica Scripta* 33(1986)180.
- [Wat 01] J. G. Watson and J. C. Chow, *Ambient air sampling, in aerosol measurement: principles, techniques, and applications*, 2nd ed., P. Baron and K. Willeke, eds. (John Wiley & Sons, New York, 2001).
- [Way 86] G. A. Wayshunas, *Am. Mineral.* 71(1986)1261.
- [Wea 67] Ch. E. Weaver, J. M. Wampler, and T. E. Pecuil, *Science* 156(1967)504.
- [Wad 99] M. L. Wade, D. G. Agresti, T. J. Wdowiak, L. P. Armendarez, and J. D. Farmer, *J. Geophys. Res.* 104(1999)8489.
- [War 87] P. H. Warren, *Icarus* 70(1987)153.
- [Wei 92] C. Weinheimer, M. Schrader, J. Bonn, T. Loeken, and H. Backe, *Nucl. Instrum. Meth.* A311(1992)273.
- [Wer 64] G. K. Wertheim, *Mössbauer effect: principles and applications*, (Academic Press, London, 1964).
- [Wen 88] S. J. Wentworth and J. L. Gooding, *Meteoritics* 23(1988)310.
- [Wdo 67] T. J. Wdowiak and D. G. Agresti, *Nature* 311(1967)140.
- [Web 00] S. Weber, P. Hoffmann, J. Ensling, A. N. Dedik, S. Weinbruch, G. Miehe, P. Gütlich, and H. M. Ortner, *J. Aerosol Sci.* 31(2000)987.
- [Wiv 81] C. Wivel, S. Mørup, *J. Phys. E. Sci. Instrum.* 14(1981)605.
- [Zol 87] M. E. Zolensky, W. L. Bourcier, and J. L. Gooding, *Mars sample return science workshop* (Lunar and Planetary Institute, Houston) (1987)157.

Appendix A

Possible Mars analogue Fe-minerals

Iron is one of the key elements in our solar system and can be found associated to different other elements. On Earth surface and interior, up to the present date, it was detected nearly 500 different iron minerals associated with almost all natural elements of the periodic table, but more commonly found with oxygen, sulfur, chlorine, carbon, and other transition metals [Ste 82]. Probably, no more than 10 iron-bearing minerals will be identified on Mars by each rover at the landing site. The list is more extensive than the minerals detected on Mars by MIMOS II because the landing sites are unlikely to be representative of the whole Martian surface. Those iron-bearing minerals where formed under specific condition (pressure, temperature, gases, water, and their soluble salts).

Table A.1 depicts some quantitative analysis performed by different Mars landers [Cla 82, Rie 97, Gel 04].

The next sections present the possible minerals already studied by Mössbauer spectroscopy that were expected to be found on Mars surface prior the MER landing. Those substances where organized in four groups:

- Iron oxide, hydroxide and oxide-hydroxide;
- Sulphate, sulphide and sulphite;
- Silicates;
- Other Minerals.

As shown in figure 3.10 the temperature on Mars surface is always below $298K$ and above $77K$. Therefore, changes is the Mössbauer parameters in

Table A.1: Average chemical composition of soils and rocks in oxide weight percents.

Elemental Analysis	Viking 1	Viking 2	Pathfinder	Mars Exploration Rover-A [†]			
	Chryse	Utopia	Soil	Rock	Soil	Adirondack Dusty	Adirondack Brushed
Fe_2O_3	17.5	17.3	14.9	17.8	17.6	19.4	19.2
Na_2O	—	—	2.7	2.3	3.3	2.7	3.1
MgO	6	6*	4.3	7.7	9.3	10.3	10.4
Al_2O_3	7.3	7.3*	10.1	8.5	10.0	11.1	11.4
Si_2O	44	43	56.6	49.5	45.8	45.8	45.5
SO_3	6.7	7.9	2.4	5.5	5.82	3.46	2.06
Cl	0.8	0.4	0.5	0.6	0.53	0.32	0.23
K_2O	< 0.5	< 0.5	0.6	0.3	0.41	0.15	0.11
CaO	5.7	5.7	6.6	6.5	6.10	7.24	7.51
TiO_2	0.62	0.54	0.9	1.2	0.81	0.52	0.46
Br ppm	~ 80	present	—	—	40	—	10

* Mg and Al for Utopia are taken as equal to Chryse data. [†] Results obtained from 11 soils and from Adirondack rock [Gel 04]. Major elements in the chemical composition of the atmosphere of Mars [Lod 98]: $CO_2=95.32\%$, $O_2=0.13\%$, $N_2=2.7\%$, $Ar=1.6\%$. *Opportunity* data were not public by the conclusion date of this thesis.

this temperature range will include their change on Mars. This temperature range was observed on Mars and was used to select the Mössbauer parameters to train the artificial neural network for phase identification.

A.1 Oxide, hydroxide and oxide-hydroxide

Table A.2: Iron oxide, hydroxide and oxide-hydroxide complexes studied by Mössbauer spectroscopy which are possible Mars substances.

Name	Formula	Remarks
	$Fe(OH)_2$	
bernalite	$Fe(OH)_3$	
goethite	$\alpha - FeOOH$	
akaganéite	$\beta - FeOOH$	
lepidocrocite	$\gamma - FeOOH$	
magnetite	Fe_3O_4	
maghemite	$\gamma - Fe_2O_3$	
hematite	$\alpha - Fe_2O_3$	
ferrihydrite	$FeHO_3 \cdot 4H_2O$	
	$\beta - Fe_2O_3$	
	$\epsilon - Fe_2O_3$	
ilmenite	$FeTiO_3$	$Mn, Fe^{2+} \rightarrow Fe$

A.2 Carbonates and Rich-Mn minerals

Table A.3: Carbonate and Mn-rich minerals studied by Mössbauer spectroscopy.

Name	Formula	Remarks
ankerite	$Ca(Fe, Mg)(CO_3)_2$	up to 0.1 of Mn reported
calcite	$CaCO_3$	$Fe \rightarrow Ca$
dolomite	$CaMg(CO_3)_2$	$Fe, Mn \rightarrow Mg$
humboldtine	$Fe(CO_3)_2 \cdot 2H_2O$	
siderite	$FeCO_3$	$Ca, Mg, Mn \rightarrow Fe$
rodochrosite	$MnCO_3$	$Fe \rightarrow Mn$
bixbyite	$(Fe, Mn)_2O_3$	
carpholite	$(Mn, Fe)Al_2(Si_2O_6)(OH)_4$	

A.3 Sulphate, sulphide and sulphite

Table A.4: Fe-S minerals studied by Mössbauer spectroscopy which are possible Mars substances.

Name	Formula	Remarks
blutlerite	$Fe^{2+}(SO_4)(OH)/2H_2O$	
coquimbite	$Fe_2(SO_4)_3/9H_2O$	
delvauxite	$CaFe^{3+}(PO_4, SO_4)_2(OH)_8/nH_2O$	
greigite	Fe_3S_4	
halotrichite	$Fe^{2+}Al_2(SO_4)_4/22(H_2O)$	
jarosite	$KFe^{3+}(SO_4)_2(OH)_6$	
kornelite	$Fe_2(SO_4)_3/H_2O$	
marcasite	FeS_2	see pyrite
melanterite	$FeSO_4/7H_2O$	
metavoltine	$K_2Na_6Fe^{2+}Fe_6^{3+}(SO_4)_{12}O_2/18(H_2O)$	
millosevichite	$(Al, Fe^{3+})_2(SO_4)_3$	
niningerite	$(Fe, Mg)_{0.5}S$	Fe is minor
pyrite	FeS_2	see marcasite
pyrrhotite	$Fe_{1-x}S$	
rasvumite	$K_1Fe_2S_3$	
rozenite	$FeSO_4/4H_2O$	
schwertmannite	$Fe_8O_8(OH)_6SO_4$	
smaltite	Fe_3S_4	see smythite
smythite	Fe_3S_4	see smaltite, $Ni \rightarrow Fe$
szolmolnokite	$FeSO_4/H_2O$	
troilite	FeS_{1-x}	
villamaninite	$(Fe, Co)S_2$	

A.4 Phosphates

Table A.5: Phosphate minerals studied by Mössbauer spectroscopy.

Name	Formula	Remarks
anapaite	$Ca_2Fe(PO_4)_2/4H_2O$	
barbosalite	$Fe_3(PO_4)_2(OH)_2$	Fe^{3+} was found
delvauxite	$CaFe^{3+}(PO_4, SO_4)_2(OH)_8/nH_2O$	
ferristrunzite	$Fe_3^{3+}(PO_4)_2(OH)_2[(H_2O)_{5.5}(OH)]$	
graftonite	$(Mg_{0.8}Fe_{0.2})_3(PO_4)_2$	$Mn, Ca \rightarrow Fe$
kershenite	$Fe^{2+}Fe_2^{3+}(PO_4)_2(OH)_2/6H_2O$	also known as kirshenite
kryzhanovskite	$MnFe_2(PO_4)_2(OH)_2/H_2O$	
lazulite	$(Mg, Fe^{2+})Al_2(PO_4)_2(OH)_2$	
lipscombite	$Fe^{3+}(PO_4)_2(OH)_2$	traces : Fe^{2+} and Mn
ludlamite	$(Fe, Mg, Mn)_3(PO_4)_2(H_2O)_4$	
metavivianite	$Fe_{1+x}^{2+}Fe_{2-x}^{3+}(PO_4)_2(OH)_{2-x}/(H_2O)_6$	
mitridatite	$CaFe_4^{3+}(PO_4)_4$	
phosphoferrite	$Fe_3(PO_4)_2/3H_2O$	
picita	$Fe_5^{3+}(PO_4)_3(OH)_6/10H_2O$	
purpurite	$(Fe_{0.3}^{3+}Mn_{0.7})(PO_4)(OH)_{0.4}$	$Na, K, Ca, Mg \rightarrow Fe, Mn : Cr, Ti, Si \rightarrow P$
vivianite	$Fe_3(PO_4)_2/8H_2O$	Fe^{3+} was also detected
wolfeite	$(Fe, Mn)_2PO_4OH$	
zwieselite	Fe, Mn_2PO_4F	

A.5 Silicates

The silicates were organized according to the standard mineralogical classification [Cor 68, Höl 89] in six groups (table A.6):

Nesosilicate Nesosilicates are silicates with isolated $[SiO_4]$ in the structure. This group includes olivine table A.7 and garnets table A.8.

Sorosilicates Sorosilicates have two silicate tetrahedrons that are linked by one oxygen ion and thus the basic chemical unit is the anion group (Si_2O_7) with a negative six charge (-6);

Inosilicate Inosilicate contains two distinct groups: the single chain and double chain silicates. In the single chain group the tetrahedrons share two oxygens with two other tetrahedrons and form a seemingly endless chain. The ratio of silicon to oxygen is thus 1:3;

Cyclosilicate These silicates form chains such as in the inosilicates except that the chains link back around to form rings. The silicon to oxygen ratio is generally the same as the inosilicates, (1:3);

Chain Silicates Silicates forming pyroxenes (single-chain structure). Pyroxene can be found as clinopyroxene (clinic crystalline structure) or as orthopyroxene (orthorhombic crystalline structure). The other structure type found in chain-silicates are the amphiboles which is characterized by a double-chain structure.

Phyllosilicates Includes the di-octahedral muscovites, tri-octahedral biotites and chlorites;

Tectosilicate Includes the feldspates, plagioclase, sodalites, and zeolites.

Table A.6: Silicate classification.

Class	Arrangement of SiO_4 Tetrahedral	Ratio Si:O
Nesosilicates	Isolated	1:4 (0.25)
Sorosilicates	Double	2:7 (0.29)
Cyclosilicates	Rings	1:3 (0.33)
Inosilicates	Single Chain	1:3 (0.33)
	Double Chain	4:11 (0.36)
Phyllosilicates	Sheets	2:5 (0.1)
Tectosilicates	Frameworks	1:2 (0.5)

A.5.1 Nesosilicates

Table A.7: Olivine nesosilicate group and minerals studied by Mössbauer spectroscopy.

Mineral	Formula	Remarks
forsterite	$Mg_2[SiO_4]$	
olivine	$(Mg, Fe)_2[SiO_4]$	
fayalite	$Fe_2[SiO_4]$	
hortonolite	$2(Fe, Mg, Mn)[SiO_4]$	
kirschsteinite	$CaFe[SiO_4]$	
knebelite	$(Mn, Fe)_2[SiO_4]$	
laihunite	$FeFe_2[SiO_4]_2$	black

Table A.8: Garnet (nesosilicate group) and minerals studied by Mössbauer spectroscopy.

Mineral	Formula	Remarks
pyrope	$Mg_3Al_2[SiO_4]_3$	
almandine	$Fe_3^{2+}Al_2[SiO_4]_3$	
spessartine	$Mn_3Al_2[SiO_4]_3$	
grossular	$Ca_3Al_2[SiO_4]_3$	
andradite	$Ca_3, Fe_2^{3+}Al_2[SiO_4]_3$	
melanite	$Fe_3^{2+}Al_2[SiO_4]_3$	
schorlomite	$Ca_6(Fe, Ti)_2[Si_5TiO_{24}]$	

Table A.9: Sillimanite-Euclase (nesosilicate group) and minerals studied by Mössbauer spectroscopy.

Mineral	Formula	Remarks
sillimanite	$Al^{[6]}Al^{[4]}[O][SiO_4]$	
andalusite	$Al^{[6]}Al^{[5]}[O][SiO_4]$	$Fe, Mn, Fe^{3+} \rightarrow Al$
mulite	$Al^{[6]}Al^{[4]}[O_3O_{0.5}OH][Si_3AlO_{16}]$	$Fe \rightarrow Al$ $Fe^{3+} \rightarrow Al$
yoderite	$(Al, Mg, Fe)_2[(O, OH) SiO_4]$	
staurolite	$Fe_2Al_9[O_6(O, OH)_2](SiO_4)_4]$	$Mg, Co, Zn, Ti, Mn \rightarrow Fe$ $Al \rightarrow Si$

Table A.10: Norbergite-Alleghanyite-leucophoenicites (nesosilicate group) and minerals studied by Mössbauer spectroscopy.

Mineral	Formula	Remaks
chondrite	$(Mg, Fe)_5[OH, F SiO_4]_2$	
clinohumite	$(Mg, Fe)_9[(OH, F)_2 (SiO_4)_4]$	
titanclinohumite	$(Mg, Fe)_{17}Ti[(OH)_2 O_2 (SiO_4)_8]$	
braunite	$Mn_4^{2+}, Mn_3^{4+}[O_8 SiO_4]$	$Ca, Mg \rightarrow Mn^{2+}$ $Al, Fe \rightarrow Mn^{4+}$
macaulayite	$(Fe, Al)_{24}Si_4O_{43}(OH)_2$	

Table A.11: Titanites (nesosilicate group) and minerals studied by Mössbauer spectroscopy.

Mineral	Formula	Remaks
chloritoid	$FeAl_2[(OH)_2 O SiO_4]$	
magnesiochloritoid	$(Mg, Fe)Al_2[(OH)_2 O SiO_4]$	

A.5.2 Sorosilicates

Table A.12: Sorosilicate minerals studied by Mössbauer spectroscopy.

Mineral	Formula	Remaks
ilvaite	$CaFe_2^{2+}Fe^{3+}[OH O Si_2O_7]$	$Na \rightarrow Ca; Al \rightarrow Fe$
clinozoisite	$Ca_2Al_3[O OH SiO_4 Si_2O_7]$	
epidote	$Ca_2(Al, Fe^{3+})Al_2[O OH SiO_4 Si_2O_7]$	
vesuvianite	$Ca_{10}(Mg, Fe)_2Al_4[(OH)_4 (SiO_4)_5 (Si_2O_7)_2]$	

A.5.3 Cyclosilicate

Table A.13: Cyclosilikate minerals studied by Mössbauer spectroscopy.

Mineral	Formula	Remaks
axinite	$Ca_2(Mn, Fe)Al_2[OH BO_3 Si_4O_{12}]$	
cordierite	$Mg_2Al_3[AlSi_5O_{18}]$	$K, Na, Ca, Mn, Fe \rightarrow Mg, Fe, Al \rightarrow Si$

A.5.4 Inosilicates

Table A.14: Inosilicate minerals studied by Mössbauer spectroscopy.

Structure Type	Mineral	Formula	Remarks
Clinopyroxene	pigeonite	$(Mg, Fe, Ca)_2[Si_2O_6]$	$Na, K, Mn \rightarrow Mg, Fe, Ca$
	diopside	$CaMg[Si_2O_6]$	$Fe, Mn \rightarrow Ca, Mg$
	hedenbergite	$CaFe[Si_2O_6]$	$Mg, Mn \rightarrow Ca, Fe$
	augite	$(Ca_{0.81}, Mg_{0.75}Fe_{0.12}^{2+})(Al, Fe^{3+}, Ti)_{0.25}$ $[Si_{1.81-1.51}Al_{0.19-0.49}O_6]$	
	aegirine	$NaFe^{3+}[Si_2O_6]$	acmite if brown-transp.
Orthopyroxene	enstatite	$Mg_2[Si_2O_6]$	$Fe \rightarrow Mg$ clinoenstatite can be found
	bronzite	$(Fe_x, Mg_{1-x})_2[Si_2O_6]$	$5 \leq \%Fe \leq 13$
	hypersthene	$(Fe, Mg)[Si_2O_6]$	$K, Na, Ca, Mn; Al \rightarrow Si$ 30-50 mol.-% Fe-Sil.
Ca-amphibole	tremolite	$Ca_2Mg_5[(OH, F)_2Si_8O_{22}]$	$Fe \rightarrow Mg$
	hornblende	$(Na, K)_{0.25-1}Ca_{1.5-2}Mg_{1.5-4}Fe_{1-2}^{2+}$ $(Al, Fe^{3+})[(OH)_2Si_{7-6}Al_{1-2}O_{22}]$	Mn and Ti can be found related to Augite
Alkali-amph.	glaucophane	$Na_2Mg_{1.5-3}Fe_{1-1.5}^{2+}Fe_{0-0.25}^{3+}Al_{0-0.25}$ $[(OH)_2Si_{7.75-8}Al_{0-0.25}O_{22}]$	
	riebeckite	$(Na, K)_{2-3}Ca_{0-0.5}Mg_{0-1}Fe_{1.5-4}^{2+}Fe_{0-3}^{3+}$ $[(OH, O)_2Si_{7.5-8}Al_{0.5-0}O_{22}]$	$Mn \rightarrow Fe^{2+}$
	arfvedsonite	$Na_{2.5}Ca_{0.5}(Fe^{2+}, Mg, Fe^{3+}, Al)_5$ $[(OH, F)_2Si_{7.5}Al_{0.5}O_{22}]$	$K \rightarrow Na, Ti \rightarrow Fe^{3+}$ $Ti, Li, Mn \rightarrow Fe^{2+}$
	anthophyllite	$(Mg, Fe)_7[(OH)_2Si_8O_{22}]$	
	rhodonite	$Ca, Mn_4[Si_5O_{15}]$	$Fe \rightarrow Mn$

A.5.5 Phyllosilicates

Table A.15: Phyllosilicate minerals studied by Mössbauer spectroscopy.

Structure Type	Mineral	Formula	Remarks
	vermiculite	$Mg_{2.36}Fe_{0.48}^{3+}Al_{0.16}[(OH)_2Al_{1.28}Si_{2.72}O_{10}]_{0.64} - ? Mg_{90.32}(H_2O)_4$	
Muscovite-series	muscovite	$KAl_2[(OH, F)_2 AlSi_3O_{10}]$	$Mg, Fe^{2+}, Fe^{3+}, Ti \rightarrow Al; Na, Ca \rightarrow K$
di-octahedral	glauconite	$[(K, Ca, Na)_{<1}(Al, Fe^{2+}, Fe^{3+}, Mg)_2(OH)_2Si_3.65Al_{0.35}O_{10}]$	Ti as trace $Fe^{2+} \rightarrow Mg$
	phlogopite	$KMg_3[(OH, F)_2 AlSi_3O_{10}]$	$Fe^{2+} \rightarrow Mg$
	biotite	$K(Mg, Fe, Mn)_3[(OH, F)_2AlSi_3O_{10}]$	Ti as trace
Biotite-series	annite	$KFe_3[(OH, F)_2 AlSi_3O_{10}]$	found with quartz, sanidine and fayalite
tri-octahedral	lepidolite	$[Fe_{1.5-1}OH_{0.5-1}Si_{3-3.5}Al_{1-0.5}O_{10}]K(Li_{1-1.5}Fe_{1-0.5}^{2+}, Al)$	
	zinnwaldite	$K(Li_{1-1.5}Fe_{1-0.5}^{2+}, Al)[(Fe_{1.5-1}OH_{0.5-1}Si_{3-3.5}Al_{1-0.5}O_{10})]$	
	stilpnomelane	$(Na, K, Ca)_{0-0.7}(Fe^{3+}, Fe^{2+}, Mg, Al, Mn)_{2.95-4.1}[(OH)_2Si_4O_{10}(O.OH, H_2O)_{1.8-4.25}]$	
	pyrophyllite	$Al_2[(OH)_2 Si_4O_{10}]$	$Na, K, Mn \rightarrow Mg, Fe, Ca$
Smectite	montmorillonite	$Al_{1.67}Mg_{0.33}[(OH)_2Si_4O_{10}]_{0.33} - ? Na_{0.33}(H_2O)_4$	Ca, Fe can be found
di-octahedral	beidelite	$Al_{2.17}[(OH)_2Al_{0.83}Si_{3.17}O_{10}]_{0.32} - ? Na_{0.32}(H_2O)_4$	K, Fe^{2+}, Fe^{3+}, Mn can be found
	nontronite	$Fe^{3+}[(OH)_2Al_{0.33}Si_{3.67}O_{10}]_{0.33} - ? Na_{0.33}(H_2O)_4$	Ti, Fe^{2+}, Fe^{3+}, Mn can be found
	talc	$Mg_3[(OH)_2 Si_4O_{10}]$	$Fe, Mn \rightarrow Ca, Mg$
Smectite	saponite	$Mg_3[(OH)_2Al_{0.33}Si_{3.67}O_{10}]_{0.33} - ? Na_{0.33}(H_2O)_4$	
tri-octahedral	hectorite	$Mg_{2.67}Li_{0.66}[(OH)_2Al_{0.33}Si_{3.67}O_{10}]_{0.33} - ? Na_{0.33}(H_2O)_4$	
	sauconite		
	clinochlore	$(Mn, Al)_3[(OH)_2AlSi_3O_{10}Mg_3(OH)_6]$	grochaulte if Fe-rich
	chaamosite	$(Fe^{2+}, Fe^{3+})[(OH)_2AlSi_3O_{10}](Fe_3^{2+}, Mg_9(O, OH)_6)$	
	kaolinite	$Al_4[(OH)_8 Si_4O_{10}]$	$Fe^{3+}, Mg \rightarrow Al$
	antigorite	$Mg_6[(OH)_8 Si_4O_{10}]$	jenkinsite if with Fe
	chrysotile	$Mg_6[(OH)_8 Si_4O_{10}]$	$Al, Ca, Ni, Fe^{3+} \rightarrow Mg$
Chlorite	amesite	$Mg_{3.2}Al_{2.0}Fe_{0.8}^{2+}[(OH)_8 Al_2Si_2O_{10}]$	$Fe^{3+} \rightarrow Al$
	cronstedtite	$Fe_2^{3+}Fe_4^{2+}[(OH)_8 Si_2Fe_3^{2+}O_{10}]$	$Na, Mg \rightarrow Fe^{2+}$
	halloysite	$Al_4[(OH)_8Si_4O_{10}](H_2O)_4$	$Fe^{3+} \rightarrow Al(Si)$
	palygorskite	$(Mg, Al)_2[(OH)_8 Si_4O_{10}] \cdot 2H_2O + H_2O$	$Fe^{3+} \rightarrow Al(Si)$

A.5.6 Tectosilicates

Table A.16: Tectosilicate minerals studied by Mössbauer spectroscopy.

Structure Type	Mineral	Formula	Remarks
	leucite	$K[AlSi_2O_6]$	$Fe \rightarrow Al; T < 605^\circ C$
Alkali-feldspar	sanidine	$(Na, K)[AlSiO_4]$	$Na : K \sim 3 : 1$
	microcline	$K[AlSi_3O_8]$	$Fe \rightarrow Na, K \rightarrow Al$
Plagioclase	albite	$Na[AlSi_3O_8]$	0-10 mol% An ¹
Sodalite	sodalite	$Na_8[Cl_2 (AlSiO_4)_6]$	$Fe \rightarrow Na, K$
Zeolite	heulandite	$Ca[Al_2Si_7O_{18}] \cdot 6H_2O$	
	zeolite	$Na[AlSi_5O_{12}] \cdot 3H_2O$	

A.6 Other minerals

This includes a list of minerals that was not found at [Cor 68], but reported by other authors.

Table A.17: Unclassified minerals studied by Mössbauer spectroscopy.

Mineral	Formula	Remarks
actinolite	$Ca_2(Mg, Fe^{2+})_5Si_8O_{22}(OH)_2$	
allophane	$Al_2O_3 * SiO_2 * nH_2O$	Na, P, Fe^{3+}, Ti tracers; Basaltic glass
alurgite	<i>complex</i>	Not found in the ref. books
amosite	$(Mg, Fe)_7Si_8O_{22}(OH)_2$	Not found in the ref. books
axinite	$Ca_2(Fe, Mn, Mg)Al_2B[OH O (Si_2O_7)_2]$	Sorosilicate; Axinite-Grp
babingtonite	$Ca_2(Fe, Mn)Fe[OH Si_5O_{14}]$	Inosilicate; Rhodonite-Grp
berthierine	$(Fe, Mg)_9(Fe, Al)_3[(OH)_{16} Al_3Si_5O_{20}]$	Phyllosilicate; Serpentine-Grp exists berth-1M and orthoberth.

¹An = Anorthite, $Ca[Al_2Si_2O_8]$

Acknowledgements

I sincerely thank my wife, Anelisa, and my daughter, Júlia, for their patience, love, and for being by my side during all this period.

I also thank Prof. Dr. José Weber Freire Macedo, the Chancellor of Federal University of Espírito Santo (UFES) for his constant encouragement. I thank my friends Professor Vijayendra Kumar Garg and Tsutomu Morimoto for their valuable support to my carrier.

I received valuable support from many Institutions and friends for my stay and work in Germany. I thankfully acknowledge financial support from Companhia Siderúrgica de Tubarão (CST), Companhia Vale do Rio Doce (CVRD), and Coordenação de Aperfeiçoamento de Pessoal de Nível Superior (CAPES) that made possible my stay and work.

At Mainz University, I have had very productive and rewarding time thanks to the nice experimental facilities and a friendly working atmosphere I ever had in my life. I thank Bodo Bernhardt, Daniel Rodionov, and Christian Schröder for their valuable assistance to my work in Mainz. I wish to thank Dr. rer. nat. Göstar Klingelhöfer for letting me share the challenging work of constructing payload instruments of interplanetary missions: All the way to Mars!

I thank the valuable support from Professor Dr. Markus Egg, Dr. Susanne Greiff, and Mr. Uwe Hertz from the Römisch-Germanisches Zentral Museum in Mainz. The RGZM staff provided me with an interesting insight to the discipline of archaeology, both on historical context of the studied artifacts and motivation toward the better understanding on manufacturing, conservation and on restoration. I thank Dr. Claus Maywald-Pitellos and Dr. Hanebutt-Benz from the Gutenberg Museum in Mainz for providing me with some unique paintings such as a nice miniature for an interesting Mössbauer surface characterization. I am thankful to Professor Dr. Dr. h.c. Udo Schwertmann for providing me with six Al-goethite reference samples for characterization and to Dr. Enver Murad for the fruitful discussions, and to Dr. Vadim Kasentonov from the Institute of Inorganic and Analytical Chemistry of the Mainz University for his assistance on SQUID measurements. I also thank Dr. Maria Elizabeth Zucolloto, the curator of the National Brazilian

Museum for providing me a large number of meteorites from their collection for my study. I also thank Dr. Richard V. Morris from NASA Johnson Space Center for the nice and fruitful discussion we had on Mars mineralogy.

I am honored for the opportunity of working during real-time surface operations for Mars Exploration Rover mission at the Jet Propulsion Laboratory, Caltech, Pasadena. For this opportunity I wish to thank Professor Dr. Steven W. Squyres, from Cornell University, Principal Investigator for MER. In the name of Dr. John Callas, Manager of MER, I would like to thank JPL-Caltech and their scientists, engineers and employees for the unwavering support during the training sessions for real-time surface operations and for the fantastic rover they built and controlled some million kilometers from our yard. I thank The Athena Science Team for the very interesting scientific discussion during the preparation for MER mission either in Pasadena or in Kennedy Space Center, Florida, as well as during the surface operations of the rovers *Spirit* and *Opportunity* on Mars.

Without guidance and interest of Professor Philipp Gütlich this work could never come to this stage. I am very much honored being a student of Professor Gütlich. In particular, for being his last 'son'.

Lebenslauf (Vitae)

Paulo Antônio de Souza Júnior
Av.: Est. José Júlio de Souza, 980/401
Ed. Gardênia - Praia de Itaparica
29102-010 Vila Velha, ES, Brazil
eMail: paulosouza2@hotmail.com

Personal data:

Date and place of birth: 20.03.1971, Campo Grande, MS, Brazil.

Married to Dr. med. Anelisa Dazzi Chequer de Souza, one child (Júlia Chequer de Souza)

Education:

1977-1984 Colégio Maria Mattos, Anchieta, ES, Brazil
1985-1987 Colégio dos Jesuítas, Juiz de Fora, MG, Brazil
1991-1999 Bachelor in Physics, UFES, Vitória, ES, Brazil
1999-2000 M.Sc., Mech. Eng. Dep., UFES, Vitória, ES, Brazil on

'Atmospheric Corrosion and Their Products Analysis in Area under Direct
Influence from Aracruz Celulose Co.'

since February 2000: graduate studies at the Johannes Gutenberg - Uni-
versität, Mainz on

'Extraterrestrial and Outdoor Terrestrial Applications of Mössbauer
Spectroscopy'

July 20th, 2000: Viva Voce